3-2022

Application of Machine Learning Models with Numerical Simulations of an Experimental Microwave Induced Plasma Gasification Reactor

Owen D. Sedej

APPLICATION OF MACHINE LEARNING MODELS WITH NUMERICAL SIMULATIONS OF AN EXPERIMENTAL MICROWAVE INDUCED PLASMA GASIFICATION REACTOR

THESIS

Owen D. Sedej, 2Lt, USAF

AFIT-ENV-MS-22-M-261

DEPARTMENT OF THE AIR FORCE
AIR UNIVERSITY

AIR FORCE INSTITUTE OF TECHNOLOGY

Wright-Patterson Air Force Base, Ohio

AFIT-ENV-MS-22-M-261

APPLICATION OF MACHINE LEARNING MODELS WITH NUMERICAL SIMULATIONS OF AN EXPERIMENTAL MICROWAVE INDUCED PLASMA GASIFICATION REACTOR

THESIS

Presented to the Faculty

Department of Engineering Management

Graduate School of Engineering and Management

Air Force Institute of Technology

Air University

Air Education and Training Command

In Partial Fulfillment of the Requirements for the

Degree of Master of Science in Environmental Engineering

Owen D. Sedej

2Lt, USAF

March 2022

AFIT-ENV-MS-22-M-261

APPLICATION OF MACHINE LEARNING MODELS WITH NUMERICAL SIMULATIONS OF AN EXPERIMENTAL MICROWAVE INDUCED PLASMA GASIFICATION REACTOR

Owen D. Sedej

2 Lt, USAF

Committee Membership:

Dr. Eric G. Mbonimpa, Ph.D., P.E.
Chair

Dr. Jeremy M. Slagley, Ph.D.
Member

Major Trevor W. Sleight, Ph.D.
Member

Abstract

Climate change continues to rage as an international and multi-faceted issue that requires immediate attention. While the stakeholders in this issue range the global population, the USDoD is one such stakeholder that has publicly raised the alarm to climate change as a threat to its current and future operations. Waste-to-energy technologies are one type of emerging solution that will help to mitigate several factors that contribute to climate change. These technologies can utilize municipal solid waste streams as a form of renewable energy while simultaneously reducing greenhouse gas emissions. One type of waste-to-energy technology that is currently emerging as an efficient and viable option is microwave-induced plasma gasification. This thesis aims to contribute to the future development of this technology by providing an in-depth literature review of how this technology physically operates and can be numerically modeled. Additionally, this thesis reviews literature of machine learning models that have been applied to gasification to make accurate predictions regarding the system. Finally, this thesis provides a framework of how to numerically model an experimental plasma gasification reactor in order to inform a variety of machine learning models. The machine learning models were able to achieve a high degree of accuracy (MAE = 0.011) for predicting the proportion of the reactor that is greater than 2000K given the input variables of reactor geometry and plasma flame temperature. This novel approach applying both computational fluid dynamics software and machine learning models with experimental microwave-induced plasma gasification systems serves to aid in the advancement of this and future waste-to-energy technologies.

Acknowledgments

To all my educators, this is only a small dividend of your enduring wisdom.

Owen D. Sedej

Table of Contents

Page

Abstract v
Table of Contents vii
List of Figures x
List of Tables xi
I. Introduction 1
Background 1
Problem Statement 2
Research Objectives 3
Scope and Approach 4
II. Scholarly Article 1: CFD Modeling of a Lab-Scale Microwave Plasma Reactor for Waste-to-Energy Applications: A Review 6
Abstract 6
Short Summary 7
Introduction 7
Materials and Methods 12
EMIPG System Physical Description 13
EMIPG Reactor Physical Description 16
Reaction Kinetics within an EMIPG Reactor 19
Governing Equations within an EMIPG Reactor 25
Modeling Tools/Software for an EMIPG Reactor 27
Forward Look 29
Conclusion 30

II. Scholarly Article 2. Artificial Neural Networks and Gradient Boosted Machines Used for Regression to Evaluate Gasification Processes: A Review 32
Abstract.....32
Short Summary.....33
Introduction 33
Materials and Methods 35
The Gasification Process 36
Important Gasification Process Terminology.....38
Machine Learning and Gasification Literature.....39
ANN models with Gasification 41
GBM models with gasification.....48
Performance Evaluation of ANN and GBM ML Models 52
Conclusion.....53
IV. Scholarly Article 3: Application of Machine Learning to Predict the Performance of an EMIPG Reactor Using Data from Numerical Simulations.....54
Abstract.....54
Short Summary.....55
Introduction 55
Data Selection.....60
Modeling an EMIPG reactor in ANSYS FLUENT.....61
Modeling Assumptions, Boundary Conditions, and Limitations 54
Modeling Geometry and Meshing.....55
Mathematical Modeling Equations.....58
Machine Learning Algorithms 60

Linear Regression ML model 61
Gradient Boosting ML Models 61
Deep Neural Network ML Model 62
Performance of the ML Algorithms 65
CFD Model Description and Resultant Data Set 66
Model Validation 69
Linear Regression ML Models 70
Gradient Boosting ML Models 72
DNN ML Models 74
Comparison of all ML Models 78
Conclusion 78
V. Conclusions and Recommendations 81
Conclusions of Research 81
Contribution of Research 82
Significance of Research 83
Future Research recommendations 83
Appendices 85
Appendix A: Numerically Modelling an EMIPG reactor using ANSYS Fluent 85
Appendix B: Code for the LR and DNN ML Models 95
Appendix C: Code for GBM ML Models 103
Bibliography ..... **Error! Bookmark not defined.**

List of Figures

Page

Figure 1. Classification of plasma gasification systems 10

Figure 2. Schematic representation of a basic EMIPG system 13

Figure 3. Close-up schematic representation of an EMIPG reactor 20

Figure 4. Schematic representation of a multi-stage gasification process 37

Figure 5. CitespaceV visualization network of matching key terms between Scopus documents 41

Figure 6. Schematic diagram of a MIMO ANN model (A) one hidden layer (B) two hidden layers 42

Figure 7. Gross representation of a GBM ML model 48

Figure 8. Numerical model geometry and meshing structure for 5.5cmx100cm EMIPG reactor 57

Figure 9. DNN model structure to predict the proportion of reactor >2000K in an EMIPG reactor 64

Figure 10. CFD solution for EMIPG reactor with contour diagram and scaled residuals 66

Figure 11. Pair plot of dataset from CFD model 69

Figure 12. Correlation matrix of the dataset provided by CFD simulations 70

Figure 13. Input parameter vs. proportion with linear regression prediction and dataset 71

Figure 14. Linear regression model with all input parameters, 100 epochs 72

Figure 15. n_estimators vs GBM models: LightGBM (LGBM), XGBoost, GBR respectively from left to right 73

Figure 16. DNN model for diameter, temperature, and length predictions vs. dataset 75

Figure 17. DNN model for diameter, temperature, and length error for 100 epochs 75

Figure 18. DNN model of all inputs over 100 epochs 76

Figure 19. (A) True value vs. DNN prediction, (B) Histogram of DNN prediction error 77

List of Tables

Page

Table 1. Advantages of MW plasma gasification systems 11

Table 2. Major components of experimental MIPG systems 15

Table 3. Reactor description within EMIPG systems 18

Table 4. Reactor kinetic relationships and effects from Yoon et al.'s research 22

Table 5. Key chemical reactions within an EMIPG system reactor[51]–[54] 24

Table 6. Numerical modeling strategies of chemical kinetics within a plasma gasification system reactor 24

Table 7. Governing equations within a plasma gasification reactor [56] 26

Table 8. Definitions for variables in Table 7 27

Table 9. Comparison of CFD modeling software packages 28

Table 10. Important terminology describing the gasification process 38

Table 11. ANN ML models used with gasification 46

Table 12. GBM ML models for regression used with gasification 50

Table 13. Reactor descriptions for reviewed EMIPG systems 61

Table 14. Geometry and temperature iterations modeled 57

Table 15. DNN model characteristics 64

Table 16. Resultant proportion for one iteration of a CFD model 67

Table 17. Demonstration of dataset used to inform the ML models 68

Table 18. Table of statistics describing the dataset used to inform the ML models..... 68

Table 19. Comparison of GBM model results with 10^5 n_estimators..... 74

Table 20. Comparison of DNN model results 77

Table 21. Comparison of all ML models with all input parameters 78

APPLICATION OF MACHINE LEARNING MODELS WITH NUMERICAL SIMULATIONS OF AN EXPERIMENTAL MICROWAVE INDUCED PLASMA GASIFICATION REACTOR

I. Introduction

"And this is not a joke: You know what the Joint Chiefs told us the greatest threat facing America was? Global warming." -President Joe Biden, Royal Air Force Mildenhall Address, 2021

Background

The existential threat of climate change directly impacts current and future United States Department of Defense (USDoD) operations beyond the historical existence of kinetic threats like terrorism and near-peer adversaries. A technology that the USDoD can leverage in order to combat climate change is an emerging waste-to-energy (WtE) solution called plasma gasification[1]. While climate change exists due to a variety of forcing factors, plasma gasification offers the opportunity to create synthetic fuels from municipal solid waste streams, reduces greenhouse gas emissions, creates a source of renewable energy, and supports the capture and reuse of certain precious elements. Plasma gasification is a technology that has experienced limited industrial scale application; however, it promises a broad range of benefits to the USDoD and greater humanity. Modeling and simulation of emerging technologies such as plasma gasification support the reduction of cost and time to market by reducing the iterative process of physical design and scale-up testing.

Problem Statement

Plasma gasification offers a solution to the broad threat of climate change in conjunction with the desire for the USDoD to be able to create synthetic fuels at contingency bases. Within the literature, a method of plasma gasification known as microwave-induced plasma gasification seems to offer the best fit technology to these USDoD desires. Microwave induced plasma gasification is a maturing technology and therefore is largely studied in the literature at an experimental scale. The lack of industrial scale application of this technology shows that there is still limited process understanding of these systems, and they can benefit from further design optimization.

Currently, there are three traditional approaches used to simulate a gasification process in order to aid in design optimization of these systems. The first approach is to create a mathematical model and simplify the process by solving the representative governing equations and ignoring any system complexities. The second approach is to discretize the domain in time and space and solve a mathematical model with more complexity. The third and final approach is to build a physical model of the system and perform experiments at a small scale. Both the first and third approaches have limitations that prevent them from creating realistic solutions of a scaled gasification system. A simple system does not capture the multitude of physical and chemical phenomena that are taking place, nor is a small-scale experiment necessarily representative of a scaled system due to the high temperature and pressure conditions that take place within it.

The best method for modeling complex gasification systems is to take advantage of modern computational power to numerically simulate the process. The genre of

programs that can be used to properly model gasification systems, including plasma gasification systems, are known as computational fluid dynamics software. One disadvantage when creating a proper computational fluid dynamics software model of a plasma gasification system is that it is extremely time consuming. Additionally, adding further modeling complexity through additional physical/chemical reactions or raising the solver resolution by creating a larger geometry or finer elemental mesh both can exponentially increase the run time of the solver. One way to help mitigate time consumption when optimizing gasification systems using computational fluid dynamics software is to synthesize the solutions of these models into a machine learning model. Once a proper machine learning model has been created and verified, it can be used to predict gasification system behavior with much more computational efficiency than computational fluid dynamics software.

Research Objectives

This thesis is focused on numerically modeling an experimental plasma gasification reactor to inform a dataset that can be used by a machine learning model to properly estimate the proportion of the reactor that is >2000K. To accomplish this, research has been focused on addressing the following objectives:

1. Understand experimental plasma gasification systems and reactors and determine how they can be evaluated numerically.
2. Understand machine learning models and determine the appropriate machine learning models that can be used with gasification systems.

3. Apply the knowledge of experimental plasma gasification systems, numerical solutions, and machine learning models to synthesize these concepts and estimate the proportion of the reactor that is >2000K.

Scope and Approach

To accomplish the research objectives, this thesis follows a scholarly format in which Chapters 2, 3, and 4 are stand alone, academic publications respectively addressing research objectives 1, 2, and 3. Chapter 2, "CFD Modeling of a Lab-Scale Microwave Plasma Reactor for Waste-to-Energy Applications: A Review" addresses the first research objective. In this article, experimental microwave-induced plasma gasification systems are described both physically and by their respective governing equations. Additionally, computational fluid dynamics software that has been widely applied to these systems are compared. Chapter 3, "Artificial Neural Networks and Gradient Boosted Machines Used for Regression to Evaluate Gasification Processes: A Review" focuses on the second research objective. This article reviews machine learning models that have been applied to predict for a continuous solution, like reactor temperature, in gasification systems. The review evaluates the accuracy of these predictive models as well as their respective structure and architecture. Chapter 4, "Application of Machine Learning to Predict the Performance of an EMIPG Reactor Using Data from Numerical Simulations" addresses the final research objective. This article applies what has been learned by the previous research objectives and synthesizes it by creating a numerical solution for an experimental microwave-induced plasma gasification reactor. Once the

numerical solution is created, it is then iterated many times to inform a dataset that is utilized by several types of machine learning models. The article then compares which model can most accurately predict the proportion of reactor that is >2000K. Finally, Chapter 5 discusses the research conclusions, contributions, significance, and future recommendations associated with this thesis.

II. Scholarly Article 1: CFD Modeling of a Lab-Scale Microwave Plasma Reactor for Waste-to-Energy Applications: A Review

Abstract

Rapidly increasing solid waste generation and energy demand are two critical issues of the current century. Plasma gasification, a type of waste-to-energy (WtE) technology, has the potential to produce clean energy from waste and safely destroy hazardous waste. Among plasma gasification technologies, microwave (MW)-driven plasma offers numerous potential advantages to be scaled as a leading WtE technology if its processes are well understood and optimized. This paper reviews studies on modeling experimental microwave-induced plasma gasification systems. The system characterization requires developing mathematical models to describe the multiphysics phenomena within the reactor. The injection of plasma-forming gases and carrier gases, the rate of the waste stream, and the operational power heavily influence the initiation of various chemical reactions that produce syngas. The type and kinetics of the chemical reactions taking place are primarily influenced by either the turbulence or temperature. Navier–Stokes equations are used to describe the mass, momentum, and energy transfer, and the k-epsilon model is often used to describe the turbulence within the reactor. Computational fluid dynamics software offers the ability to solve these multiphysics mathematical models efficiently and accurately.

Short Summary

This article reviews literature that has either modeled or experimented with experimental microwave-induced plasma gasification systems. By reviewing the literature, the physical process of these systems and their reactors can be compared and understood. Additionally, governing solutions that can be used in order to numerically solve for these systems are identified. Finally, modeling software that allows for the numerical solutions to be solved by computational power are compared and their respective advantages and disadvantages are listed.

Introduction

In 1950, the global population was estimated at approximately 2.5 billion individuals; meanwhile, current predictions foresee a 2050 population of about 10.6 billion individuals[2]. Larger waste streams and consumption of energy accompany a rapidly increasing population and will continue to do so at the same rapid rate[3]–[5]. Furthermore, the current global waste stream is experiencing increases in its composition of complex and hazardous wastes, including electronics, plastics, and medical waste[6], [7]. This problem is felt not only at the global level, but also within small system environments. Small systems such as remote deployed environments, long-duration space missions, and disaster camps face a lack of access to waste disposal facilities and reliable sources of energy[8], [9].

One solution to this current problem is using waste-to-energy (WtE) technology. WtE technologies can simultaneously reduce a municipal solid waste stream and produce

energy. One type of WtE technology is plasma gasification. Plasma gasification is a process that introduces waste material into a reactor to be combusted by a plasma flame. This process takes place at extremely high heat, with temperatures within the reactor exceeding 6000 K [10]. Through this reaction at very hot temperatures, carbonaceous material is decomposed predominantly into carbon monoxide (CO) and hydrogen (H_2), which can be used as synthetic gas, or syngas, for energy production [11]. Solid waste that is produced from the combustion process, known as slag, has demonstrated material properties that would allow it to be used as supplemental cementitious materials in construction applications, thus removing it from landfilled waste stream [12].

Plasma gasification also offers several benefits over other WtE technologies. One benefit is the high efficiency of the system. The conversion efficiency of the waste material within plasma gasification systems can reach as high as 100% [13]. While the initial plasma flame is energy-intensive to create, it is estimated that only 2% to 5% of energy from the waste is needed to continue the combustion process, allowing the remaining energy to be captured for other uses [14]. Due to the hazardous composition of current waste streams, WtE technologies that use traditional combustion methods can cause pollution problems from the release of undesirable by-products and toxins, such as dioxin, furans, and greenhouse gases [15]. Plasma gasification is an emerging WtE technology that has demonstrated the ability to safely combust hazardous materials without producing toxic residue and air emissions, significantly reducing greenhouse gas emissions. With temperature in excess of 5000 $^{\circ}$C, a leach-free glass-like (vitrified) slag residue is formed [14]. Plasma gasification systems are described by three distinct

categories based on the plasma generator type, reactor design, and the working gas that is used within the reactor [10]. Plasma generator types consist of direct current (DC), alternating current (AC), radio frequency (RF) induction, microwave (MW) discharge, and hybrid systems. DC and AC plasma generators utilize an electric current that passes between two electrodes. When in the presence of a sufficiently high gas flow, the plasma extends beyond the two electrodes and forms a plasma flame. RF induction and MW discharge plasma generators utilize electromagnetic energy from a source that allows a plasma flame to form when in the presence of a plasma-forming gas. DC and AC plasma generators have been scaled up to 6 MW. These large-scale systems have operational and maintenance disadvantages such as reactor contamination from the electrodes, which need to be replaced once degraded [10]. MW discharge plasma systems generate a denser and larger plasma flame than RF induction systems [10]. Some systems utilize multiple techniques to either further refine the syngas that was produced or to initiate a plasma flame with a DC or AC electrode configuration which is then removed and sustained by RF induction or MW discharge. These are known as hybrid systems. Different reactor designs include a plasma fixed/moving bed reactor system, a plasma entrained-flow system, and a spout reactor fluid system. Plasma fixed/moving bed reactor systems are the simplest reactors and consist of a bed of solid waste, a waste feeding unit, an ash removal unit, and a syngas exit [10]. These reactors offer the advantage of a simple setup and have been proven in large-scale demonstration projects. Plasma entrained-flow bed reactors push the waste feedstock through a plasma flame, which enables them to be described as a plug flow system [10]. The degree to which these types of reactors have

been scaled is limited to laboratory testing, and the reactors suffer from low energy efficiency [10]. Spout reactor systems are a combination of a fluidized bed and a plasma spouted bed in which the plasma flame is combined with a fluid gas flow [10]. These reactors are able to obtain higher operating temperatures and a higher rate of mixing than the previous reactors. These reactors are also the most difficult to construct and operate [10]. The type of plasma working gas that is chosen for a system depends on a variety of factors. Gases can be selected in order to help carry the feedstock into the reactor or to provide turbulence and mixing within it. Additionally, gases can be selected in order to supplement the chemical reactions taking place within the reactor. Most gases are chosen depending on their availability (e.g. Argon and Nitrogen). RF and MW plasma systems typically can use steam or oxygen within the system as they operate without electrodes and, therefore, do not need to consider corrosion [10]. Figure 1 shows several variations of plasma gasification systems [14].

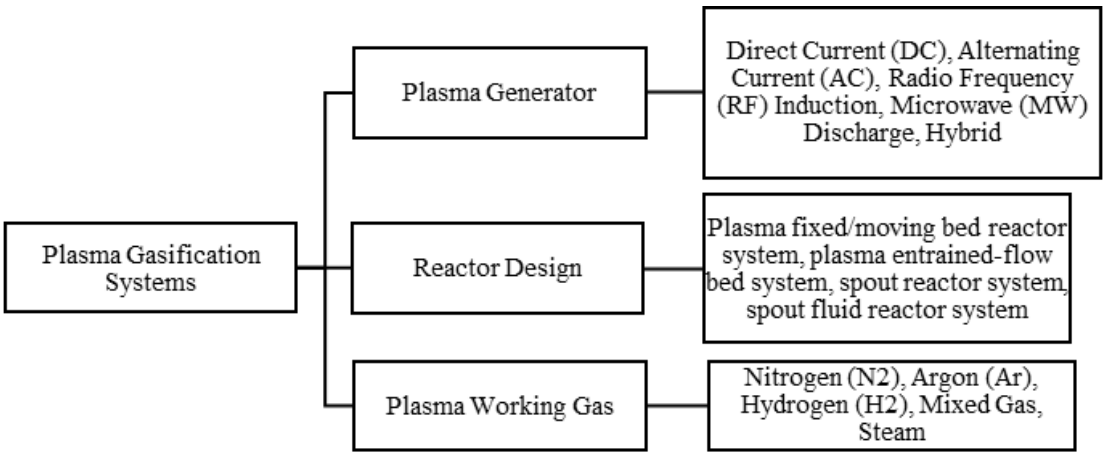

Figure 1. Classification of plasma gasification systems

MW discharge plasma gasification is one type of plasma gasification system that offers distinct advantages over other plasma gasification systems. Table 1 summarizes these advantages. Unfortunately, one drawback of MW discharge plasma gasification is that these systems have not been subject to much application beyond the laboratory scale. One large-scale example of an MW discharge plasma gasification system that could become commercially viable is found in research by Uhm et al. [16]. Two microwave systems directed towards the top and bottom of the reactor had to be used to provide an evenly distributed temperature profile within the scaled-up volume. This limitation is of important note as an increase in microwave systems will demand more power and could perhaps limit the efficiency of large systems. This type of limitation is also experienced with DC and AC plasma gasification systems, as their electrode size and power input need to be increased to be utilized as larger, commercial systems.

Table 1. Advantages of MW plasma gasification systems

Source	**Advantage**
[17]	Lower voltage requirement than other plasma generator methods.
[18]	Lower setup cost due to its ability to operate under atmospheric conditions, also allowing the system to be much more compact in size.
[17], [19]	Works without an electrode arrangement so that it avoids operational problems specific to electrode utilization.
[20]	Microwave energy has already shown its ability to safely combust a variety of hazardous wastes through previous remedial applications.

A review on plasma gasification labeled one plasma gasification challenge as "limited process understanding" [21]. Therefore, this review seeks to help close the gap on the limited process understanding of MW plasma gasification in order to support the numerical modeling of experimental microwave-induced plasma gasification (EMIPG) system reactors.

Materials and Methods

This review focuses on small, laboratory-scale experimental systems configured for plasma gasification. The majority of the material referenced is specifically related to EMIPG systems. Additional material is focused on numerical modeling and governing equations for plasma-driven systems and reactors, as well as computational fluid dynamic (CFD) software that is available to solve numerical models in regard to these systems. It is of important note that all mentioned plasma within this review is thermal plasma, and not nonequilibrium (cold) plasma. Cold plasma is typically used in combination with other pyrolysis processes as a method for the conversion, and thus reduction, of tar and other non-desirable outputs that could degrade or damage the system[22], [23]. This review contains a total of 65 peer-reviewed journal articles. Additionally, 5 CFD modeling software manufacturer websites were cited in order to provide information about the specifications their products have to offer. Searches for reviewed journal articles were conducted on databases such as ScienceDirect, Google Scholar, IEEE Explore, and MDPI Open Access Journals. Search terms that were used to find reviewed journal articles consisted of the following keywords: "plasma gasification", "microwave

driven plasma gasification", "numerical modeling of plasma reactor", "pyrolysis", "waste-to-energy technologies".

EMIPG System Physical Description

The setup for an EMIPG system can be divided into five distinct sections: power supply and microwave source, wave propagation section, plasma reactor, carrier gas/feedstock inputs, and data collection equipment. A schematic representation of these basic elements assembled into a system is shown in Figure 2.

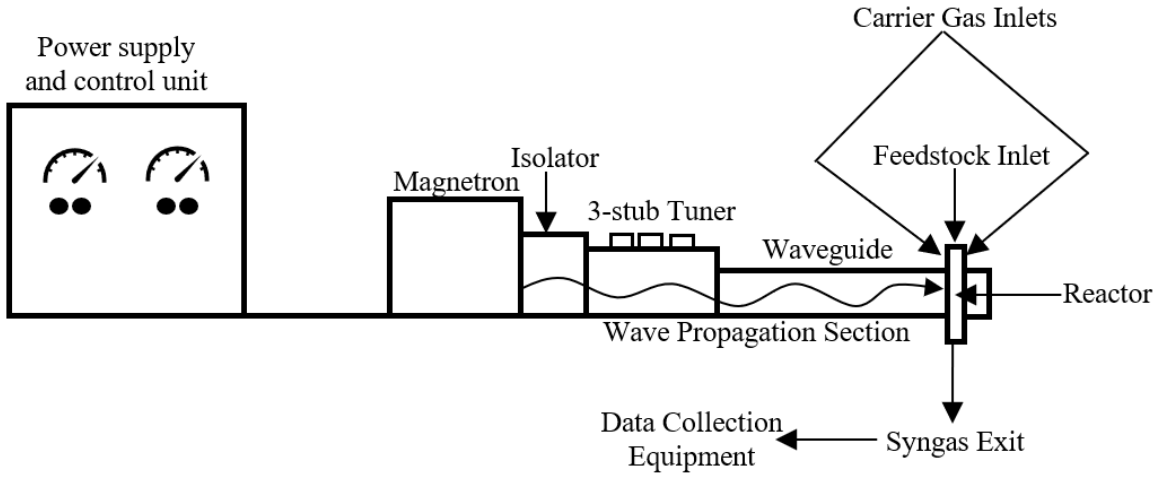

Figure 2. Schematic representation of a basic EMIPG system

Microwaves are generated by a magnetron that operates at a specific frequency and power setting. The typical power setting found within the reviewed literature for an EMIPG system ranges from 0.8 kW to 6 kW. The typical frequency that the magnetron within an EMIPG system operates at is 2.45 GHz. This frequency of 2.45 GHz is normally used at the experimental scale, as it is also the operating frequency of most domestic microwave ovens [24]. A commonly used waveguide for an EMIPG system is

the WR-340. The WR-340 is a hollow, rectangular metal waveguide that transports the electromagnetic energy created by the magnetron to the reactor in a single dimension [25]. Some EMIPG setups include an isolator and/or three-stub tuner along the wave propagation section of the system. A three-stub tuner can significantly improve efficiency as it is able to maximize the electric field from the point of generation to the distance of the reactor, substantially reducing reflected power within the system [26]. An isolator assists in protecting the magnetron from damage that can be caused by reflected microwaves[27], [28]. The reactor, various carrier gases, and other inputs that are fed into said reactor will be discussed further in the next section. Mass flow controllers (MFC) are used to govern the flow of carrier gases, plasma-forming gases, and aerosolized feedstocks into the reactor of an EMIPG system.

Additionally, data collection equipment can be combined within an EMIPG system in order to follow the syngas as it exits to identify its composition. Some examples of data collection equipment within the EMIPG system are thermocouples, both R-type and K-type, and CCD cameras. Examples of data collection equipment that may be used to analyze the chemical composition of the syngas matrix are gas chromatographs (GC), emission spectroscopy systems (ES), and Fourier-transform

infrared spectroscopy (FTIR) systems. Further details pertaining to EMIPG systems within their respective literature are located in Table 2.

Table 2. Major components of experimental MIPG systems

Source	Power Setting	Magnetron	Waveguide	MFC	Three-Stub Tuner	Data Collection Equipment	Other Equipment
[29]	1–6 kW	2.45 GHz (Sairem GMP G4 60 K T400)	WR-340	Alicat Scientific, Tucson AZ, USA	Yes	3 thermocouples, HR 2000+ES spectrometer (Ocean Optics Inc., Largo, FL, USA)	E-3000 precision steam generators
[30]	2–5 kW	2.45 GHz (Sairem GMP G4 60 K T400)	WR-340	Alicat Scientific, Tucson AZ, USA	Yes	4 type K thermocouples, HR2000+ ES spectrometer (Ocean Optics Inc., Largo, FL, USA)	E-3000 precision steam generators
[19]	Up to 6 kW	2.45 GHz (N.S.)	WR-340	Bronkhorst F-210 AV-50 K	N.S.	Offline micro-gas chromatograph (micro-GC, Varian CP-4900), sampling bags (Tedlar, 15 L)	Impedance tuner, solid feeder
[31], [32]	1–1.8 kW	2.45 GHz (SM 745, Richardson Electronics)	N.S.	Brooks 5850	Yes	2 R-type and 5 K-type thermocouples, GC HP 6890, TCD Carbosphere 80/100 packed column, Alltech	Glycerol preheater and feeder, steam supplier, gear pump (Cole Parmer, 74014-750), syringe pump, band heater
[26]	4 kW	2.45 GHz (N.S.)	WR-340	N.S.	Yes	Gas analyzer (N.S.)	Quartz plate installed in the end of tapered waveguide
[33]	5 kW	2.45 GHz (N.S.)	Twisted Waveguide	N.S.	Yes	Gas analyzer (N.S.)	Quartz plate installed in the end of tapered waveguide
[34]	1.2–1.6 kW	2.45 GHz (N.S.)	WR-248	N.S.	Yes	Optical emission spectroscopy system, transmission stage, optical fiber bundle, spectrometer, CCD camera, data acquisition unit	Forward and backward power meter controller

[35]	0.8, 0.9, and 1 kW	Not specified	N.S.	N.S.	Yes	GC/TCD, RGA, ESEM, EA (N.S.)	Voltage regulator, cooling water
[36]	0.8–1.8 kW	2.45 GHz (National Electronics YJ-1600)	WR-340	N.S.	Yes	GC, FTIR	Cavity resonator
[37]	0.8–1.4 kW	2.45 GHz (National Electronics YJ-1600)	ASTEX WR-340	N.S.	Yes	GC/TCD, FTIR, MS	Cavity resonator
[38]	Up to 6 kW	2.45 GHz (N.S.)	WR-340	Bronkhorst F-201 AV-50 K	Yes	GC, collection bags (N.S.)	Variable reflector, Sairem SAS for all microwave circuits, impedance transformer
[39]	Up to 6 kW	915 MHz, 2.45 GHz	WR-975, WR-430	N.S.		GC (Shimadzu GC-2014 and SRI 8610 C), FTIR (Thermo Nicolet 380), optical emission spectroscopy (CVI DK-480), CCD camera	Water cooling, ferrite circulator with water load, directional coupler, moveable plunger

N.S.: not specified

EMIPG Reactor Physical Description

The typical reactor within an EMIPG system consists of a hollow quartz tube with a specific length and diameter. A breakdown of reactors within EMIPG system reactors and their distinctive physical parameters from the literature review can be found in Table 3. Quartz is commonly used as the material of choice in an EMIPG system reactor for its ability to withstand a wide range of pressure and temperature conditions, as well as its ability to minimally contaminate the product syngas [40]. The reviewed literature shows that the temperature of the plasma flame and the reacting species within the quartz reactor can reach as high as 6100 K. The pressure within all reviewed EMIPG reactor systems remained at an atmospheric level. Most of the feedstocks used within EMIPG systems

were simple organic compounds such as methanol, ethanol, and coal. The EMIPG systems that did not use any solid feedstocks or organic compounds were focused on optimizing the plasma flame or observing how different gases can be processed into a useful syngas. Therefore, the only inputs into the reactor of these EMIPG systems are from carrier gases and plasma-forming fluids in order to create and sustain a plasma flame. AC and DC plasma gasification systems have been used at a large industrial scale to safely process MSW, biomass, tires, plastics, hazardous wastes, and refuse-derived fuel (RDF) [41].

Other inputs into an EMIPG system reactor are carrier gases and plasma-forming gases. Carrier gases accompany the feedstock into the reactor and are typically related to the feedstock input by a ratio. Carrier gases typically consist of air, oxygen (O_2), and steam (H_2O). The carrier gases can be tangentially injected into the reactor, allowing them to act as a physical insulator of the quartz reactor by stabilizing and centering the plasma flame within it [36]. Carrier gasses can have additional benefits by affecting the chemical kinetics within the reactor.

Plasma-forming gases typically consist of nitrogen (N_2) or argon (Ar), as they are able to populate the reactor chamber with high-energy electrons that support a more efficient and higher temperature plasma flame [42]. The majority of the EMIPG systems use a tungsten rod that is inserted into the reactor to initiate the plasma flame and then quickly withdrawn from it. This process has been conducted both mechanically and manually within the reviewed literature. The tungsten rod acts as a temporary electrode, and its properties, particularly its high-temperature resistance, make it well suited for the

environment within the EMIPG reactor [43]. Other EMIPG systems start the plasma flame within the reactor by introducing a partially ionized plasma-forming gas that is able to support the plasma arc, free from physical electrodes [44]. The downside of this process is that the EMIPG setup will require external equipment that provides excitation energy to the plasma-forming gas by partially ionizing it before it enters the reactor. The equipment used as a source of ionization to the plasma-forming gas is also used in laboratory environments that have inductively coupled plasma (ICP) spectroscopy systems [45].

Table 3. Reactor description within EMIPG systems

Source	Feedstock	Rate of Feedstock Input	Reactor Geometry	Operating Pressure	Carrier Gases/Plasma-Forming Gases	Rate of Carrier Gas/Plasma-Forming Gases Input	Ignition Source	Reactor Temperature
[29]	None	None	Quartz tube (L: 450 mm, OD: 25.6 mm, ID: 30 mm)	Atmospheric	H_2O, CO_2	20–50 g/min, 20–80 SLPM	Inserted tungsten rod	Up to 6300 ℃
[30]	None	None	Quartz tube (L: 35 cm, OD: 25.6 mm, ID: 30 mm)	Atmospheric	H_2O, CO_2, Air	10–50 g/min (up to 200 ℃), 0–100 SLPM, 0–100 SLPM	Inserted tungsten rod	Up to 6300 ℃
[19]	$CH_{1.5}O_{.49}$	09–13 g/s	Quartz Tube (L: 50 mm, OD: 34 mm, ID: 30 mm)	Atmospheric	Air, N_2	8.5–10 NL/min, 17.9–25 NL/min	Used plasma-forming gas (N_2)	973–2173 K
[31][32]	Coal	1 g/min	Quartz Tube (L:100 cm, ID: 5.8cm)	Atmospheric	N_2, O_2, steam	15 L/min, 0–1.0 L/min, 0–1.5 mL/min	Used plasma-forming gas (N_2)	Above 3000 ℃
[32]	Glycerol	3 g/min	Quartz Tube (L:100cm, ID: 5.8cm)	Atmospheric	N_2, O_2, steam	15 L/min, 0–2.6 L/min, 0–7.2 mL/min	Used plasma-forming gas (N_2)	N.S.
[26]	Coal	0–3.75 kg/hr	Quartz tube (L: N.S., OD: 30 mm, thickness: 1.5 mm)	Atmospheric	O_2, air	20 L/min, 15 L/min	Inserted tungsten rod	2000–6500 K
[33]	Coal	160 mol coal powder/hr	Quartz tube (L: N.S., OD: 30 mm, thickness: 1.5 mm)	Atmospheric	O_2	14 mol/hr	N.S.	5000 ℃

[34]	None	None	Quartz tube (2.54 cm in diameter and 22.5 cm in length)	Atmospheric	Air, N_2, Ar	30 L/min-60 L/min	Inserted tungsten rod	5446–6100 K
[35]	Spirulina algae	1 g of dry Spirulina algae	Quartz tube (L: 35 cm, OD: 3.3 cm, ID: 2.9 cm)	Atmospheric	N_2	12 L/min	N.S.	1063–1121 K
[36]	CH_4	12–18 SLPM	Quartz tube (OD: 3.3 cm)	Atmospheric	N_2	12–18 SLPM	N.S.	N.S.
[37]	Methanol	12.4 SLPM	Quartz tube (ID: 2.9 cm)	Atmospheric	N_2	N.S.	N.S.	1500 K
[38]	Cellulose	0.5 g/s	Quartz tube (ID: 31 mm, wall thickness: 2 mm)	Atmospheric	Air	15–20 NL/min	Inserted ignition electrode system	4000–5000 K
[39]	Ethanol	Introduced into system via bubbler @ 20 °C and 3% *v*/*v*	Quartz tube (N.S.)	Atmospheric	CO_2, N_2, Ar	1500–3900 NL/h	N.S.	Up to 6000 K

*N.S.: not specified, L: length, OD: outside diameter, ID: inside diameter, SLPM: standard liter per minute.

Reaction Kinetics within an EMIPG Reactor

A close-up schematic of an EMIPG system reactor and how all of its different components interact is shown in Figure 3. The basic components that make up an EMIPG system reactor include the microwave, which is transferred within a waveguide, the reactor, the input gas, and the feedstock (waste stream). When the feedstock meets the plasma flame, it is converted into a syngas and rises out of the syngas exit to be collected. Feedstock that is not fully combusted falls out of the reactor and is collected as char or ash. Systems that utilize an input gas generally place it above the feedstock entrance so that the entire residence time of the feedstock in the reactor is influenced by it.

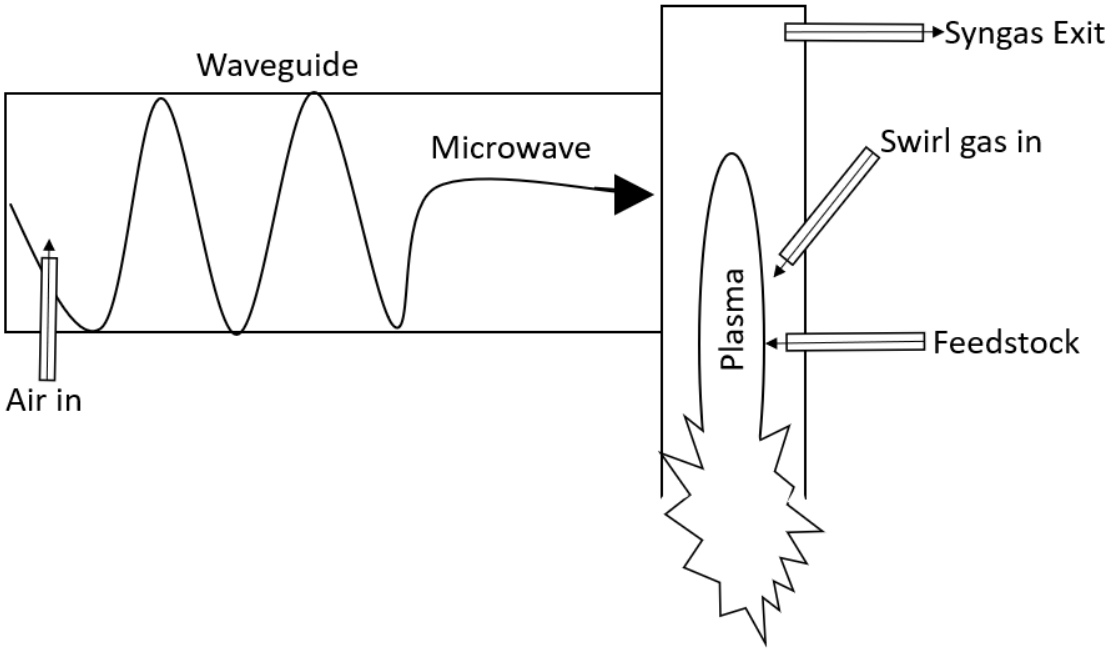

Figure 3. Close-up schematic representation of an EMIPG reactor

The high heating of feedstock and the heat transfer rates within an EMIPG system reactor are described by a process known as fast pyrolysis [46]. The temperature within an EMIPG reactor can exceed 6000 K. Besides the heat transfer within an EMIPG system reactor, a variety of other fluctuating factors determine the overall kinetic reaction that takes place within it to yield a syngas output. These factors include turbulence discrepancies and the rates and respective concentrations of the feedstock, carrier gas, and plasma-forming gas inputs. System variances such as geometry, power source, part and build quality, use of water cooling, and other implemented efficiencies can also affect the reaction kinetics within an EMIPG system reactor. In their research, Yoon et al. used an EMIPG system to compare how different rates and concentrations of input gases, as well as feedstock, can affect the plasma flame and resulting output syngas

composition. The research conducted by Yoon et al. explored the effects of O_2-to-feedstock ratio, steam-to-fuel ratio, microwave power, rate of feedstock input, and ways to promote gasification efficiency of the EMIPG system. The H_2 portion of the syngas linearly decreased as the rate of O_2 was increased relative to the rate of the feedstock into the reactor [31], [32], [47]. CO and CO_2 remained relatively constant in the output syngas until the O_2-to-feedstock ratio reached 0.6 [31], [32], [47]. Following a 0.6 O_2 to feedstock ratio, CO decreased in the syngas mixture, and CO_2 rapidly increased [31], [32], [47]. Overall, greater O_2 presence within the reactor increased the reaction temperature within it [31], [32], [47]. The increased temperature promoted a greater flow velocity within the reactor, which yielded less efficiency as the feedstock retention time (FRT) within the reactor was reduced [31], [32], [47]. A 2017 study concluded that FRT within the reactor of an MW discharge plasma gasification system is a key parameter affecting the gasification performance and overall efficiency of the system [18]. Yoon et al. also observed the impact of the steam-to-feedstock ratio within an EMIPG system reactor. The research concluded that both H_2 and CO_2 content of the resulting syngas increased as the ratio of steam to feedstock increased [31], [32], [47]. Alternatively, CO content decreased as the steam-to-feedstock ratio increased [31], [32], [47]. Ultimately, the decrease in the CO content and the resulting heating value of the syngas was found to control the syngas efficiency [31], [32], [47]. Furthermore, the research found that gasification efficiency was supported by the temperature, length of the plasma flame, and the FRT within the reactor [31], [32], [47]. The microwave power setting helped to improve combustible gas content, syngas heating value, gas yield, conversion rate, and

overall efficiency [31], [32], [47]. Additionally, an excessive rate of feedstock input would lower the reactor temperature, causing a poor syngas yield [31], [32], [47]. It is important to note that the feedstock used within the Yoon et al. research was limited to coal and glycerol; regardless, their research still serves as a great foundation for informing numerical modeling with this feedstock. All the factors previously discussed that Yoon et al. observed are summarized in Table 4.

Table 4. Reactor kinetic relationships and effects from Yoon et al.'s research

Relationship	Effect
O_2-to-feedstock ratio	• H_2 content in syngas linearly decreased with O_2 additions. • CO remained constant until O_2-to-feedstock ratio reached 0.6 and then decreased. • CO_2 remained constant until O_2-to-feedstock ratio reached 0.6 and then rapidly increased. • Increasing the O_2-to-feedstock ratio increased the reactor temperature and the CH_4 content in the syngas due to the decomposition. • Increase in O_2 supply increases the reaction temperature, which increases the flow velocity. Therefore, the syngas is less efficient because the FRT is reduced.
Steam-to-feedstock ratio	• H_2 and CO_2 content in the syngas increased with the increase in the steam-to-fuel ratio. • CO content decreased with the increase in the steam to fuel ratio. • Decrease in CO content and the heating value of the syngas leads to the decrease in carbon conversion and cold gas efficiency.
Gasification efficiency	• Dominated by the temperature, length of the plasma flames, and the FRT.

Microwave power	• Increase in microwave power improves the combustible gas content, syngas heating value, gas yield, conversion rate, and efficiency.
Rate of feedstock input	• With glycerol feed rate it was found that an excessive supply would lower the reactor temperature and thus decrease the heating value and production yield of syngas.

Many different chemical reactions take place within an EMIPG reactor. Furthermore, due to the high-temperature nature of a plasma gasification reactor, there are a variety of matter phases across which these reactions take place. Thus, chemical reactions are described as *heterogeneous* if different matter phases are involved and *homogeneous* if they happen within a single matter phase. Typical chemical reactions that take place within an EMIPG system reactor are devolatilization, oxidation, water gas, water gas shift, Boudouard, methanation, steam methane reforming, nitrogenous species formation, and sulfur species formation reactions. The stoichiometric reaction chemistry of these reactions is displayed in Table 5. Chemical reaction rates within an EMIPG reactor can be controlled by either the turbulence or the temperature phenomena that are occurring within it [48]. In order to accurately model the reaction kinetics within an EMIPG reactor given the previous scenario, a common method used is the finite rate chemistry/eddy dissipation (FRC/EDM) Model. The FRC/EDM model considers both the Arrhenius and eddy dissipation reaction rates taking place within the reactor and chooses the minimum value of the two contributions in order to establish the reaction rate [49]. The FRC/EDM model as previously described is commonly referred to as the Kobayashi model [50]. Additionally, it is important to consider the devolatilization of organic

feedstocks within an EMIPG reactor. Devolatilization drives moisture and volatile matter from the organic feedstock through the heat within the reactor, and it must be considered in order to build an accurate model of the reactor chemistry [49]. Reviewed literature typically used the FRC/EDM model while simultaneously considering devolatilization in modeling the chemical kinetics within a plasma gasification system reactor. These respective articles that modeled the chemistry within plasma reactors are found in Table 6.

Table 5. Key chemical reactions within an EMIPG system reactor[51]–[54]

Reaction Name	Stoichiometric Description
Devolatilization	$CH_xO_yN_zS_w \rightarrow Char + Volatiles$
Oxidation	$C + 0.5O_2 \rightarrow CO, \Delta H^0 = -268 \text{ kJ mol}^{-1}$ $C + O_2 \rightarrow CO_2, \Delta H^0 = -406 \text{ kJ mol}^{-1}$
Water gas reaction	$C + H_2O \rightarrow CO + H_2, \Delta H^0 = 131.4 \text{ kJ mol}^{-1}$
Water gas shift	$CO + H_2O \leftrightarrow CO_2 + H_2, \Delta H^0 = -42 \text{ kJ mol}^{-1}$
Boudouard	$C + CO_2 \rightarrow 2CO, \Delta H^0 = 172.6 \text{ kJ mol}^{-1}$
Methanation	$C + 2H_2 \leftrightarrow CH_4, \Delta H^0 = -75 \text{ kJ mol}^{-1}$
Steam methane reforming	$CH_4 + H_2O \leftrightarrow CO + 3H_2, \Delta H^0 = 206 \text{ kJ mol}^{-1}$
Nitrogenous species	$Char - N \overset{H}{\rightarrow} HCN$ $HCN + H_2O \rightarrow NH_3 + CO$
Sulfur species	$H_2S + CO_2 \rightarrow COS + H_2O$ $H_2S + CO \rightarrow COS + H_2$

Table 6. Numerical modeling strategies of chemical kinetics within a plasma gasification system reactor

Source	Reactor Type	Modeling Software	Model Used	Devolatilization Considered	Equations/Models Implemented
[48]	Downdraft Plasma Coal and Biomass Gasifier Reactor	ANSYS Fluent	FRC/EDM	Yes	FRC/EDM Devolatilization: single rate model
[55]	Downdraft plasma coal gasifier reactor	ANSYS Fluent	FRC/EDM	Yes	FRC/EDM Devolatilization: single rate model

[56]	Pilot-scale plasma bubbling fluidized bed reactor	ANSYS Fluent	FRC/EDM	Yes	FRC/EDM Devolatilization: user-defined function (UDF) using single rate model developed by Badzioch and Hawsley [57].
[7]	Updraft plasma gasifier reactor	ANSYS Fluent	FRC/EDM	Yes	FRC/EDM Devolatilization: UDF
[58]	Downdraft plasma gasifier reactor	Aspen Plus	N.S.	Yes	HCOALGEN model: used to estimate the heat of combustion, heat of formation, and heat capacity of feedstock. DCOALIGT model: used to calculate the density of the feedstock.
[59]	Plasma spouted bed gasifier	OpenFOAM	N.S.	Yes	Multiphase particle-in-cell approach (MPPICFoam) CoalChemistryFoam

Governing Equations within an EMIPG Reactor

The reaction kinetics discussed previously are mostly governed by both the temperature and turbulence parameters inside the reactor. Turbulence and temperature directly influence the variable velocity fields (gasifier flow phenomena) at high Reynolds numbers and thus affect momentum, energy, species concentration and transport, heat transfer, drag, vorticity distribution, and swirl flows [49]. In order to properly understand which of the two parameters is controlling the reaction kinetics at a given place and time in the reactor, a complex mathematical model must be created. Typical models within the reviewed articles employ the principles of Navier–Stokes equations for mass, momentum, and energy balance, as well as a Reynolds-averaged Navier–Stokes simulation (RANS) model equation for the turbulence in the reactor. In order to simplify the fluid motion within the reactor, the Eulerian–Eulerian approach is commonly used where both the gas and solid phases are combined into a single continuum [56]. This approach is common for plasma gasification systems because the high heat and turbulence within the reactor,

as well as the small solid feedstock size and carrier fluid, cause the gas and solid phase flows to behave similarly to each other. The method that is commonly employed to solve the combination of these complex mathematical models is the finite volume method. The finite volume method discretizes the geometry of the reactor by creating a three-dimensional mesh of a specific number of volumes within it. These volumes allow for the mathematical models to be solved within each discrete volume of the mesh and can be pieced together to describe the entirety of the fluid within the reactor. The RANS approach typically employs the standard k-epsilon model for turbulence. This model is widely accepted for plasma reactor modeling due to its low computational cost and accuracy [56]. All models for mass, momentum, energy conservation, and turbulence are defined in Table 7 and Table 8 and were solved using the finite volume method.

Table 7. Governing equations within a plasma gasification reactor [56]

Mass Balance Model	Momentum Model	Energy Conservation Model	Turbulence Model
Solid phase: $\frac{\partial}{\partial t}(\alpha_s\rho_s) + \nabla\cdot(\alpha_s\rho_s\,\vec{v}_s) = S_{sg}$ **Gas phase:** $\frac{\partial}{\partial t}(\alpha_g\rho_g) + \nabla\cdot(\alpha_g\rho_g\,\vec{v}_g) = S_{gs}$ **Supporting equations:** $S_{sg} = -S_{gs} = M_c\sum\gamma_c R_c$ $\frac{1}{\rho_g} = \frac{RT}{p}\sum_{i=1}^{n}\frac{Y_i}{M_i}$	**Solid phase:** $\frac{\partial}{\partial t}(\alpha_s\rho_s\,\vec{v}_s) + \nabla\cdot(\alpha_s\rho_s\,\vec{v}_s\vec{v}_s) = -\alpha_s\cdot\nabla p_s + \nabla\cdot\alpha_s\bar{\tau}_s + \alpha_s p_s\vec{g} + \beta(\vec{v}_g - \vec{v}_s) + S_{sg}U_s$ **Gas phase:** $\frac{\partial}{\partial t}(\alpha_g\rho_g\,\vec{v}_g) + \nabla\cdot(\alpha_g\rho_g\,\vec{v}_g\vec{v}_g) = -\alpha_g\cdot\nabla p_g + \nabla\cdot\alpha_g\bar{\tau}_g + \alpha_g p_g\vec{g} + \beta(\vec{v}_g - \vec{v}_s) + S_{gs}U_s$	**Gas and solid phases:** $\frac{\partial}{\partial t}(\alpha_q\rho_q h_q) + \nabla\cdot(\alpha_q\rho_q\,\vec{v}_q\,h_q) = \alpha_q\frac{\partial}{\partial t}(\rho_q) + \bar{\tau}_q:\nabla\cdot\vec{v}_q - :\nabla\cdot\vec{q}_q + S_q + \sum_{p=1}^{n}(\vec{Q}_{pq} + \dot{m}_{pq}h_{pq} - \dot{m}_{pq}h_{pq})$ **Supporting equations:** $\vec{Q}_{pq} = h_{pq}(T_p - T_q)$ $h_{pq} = \frac{6k_p\alpha_q\alpha_p N_{u_q}}{d_p^2}$ $N_{u_s} = \frac{h_{gs}d_s}{k_g} = (7 - 10\alpha_g + 5\alpha_g^2)(1 + 0.7Re_s^{0.2}Pr_g^{0.33}) + (1.33 - 2.4\alpha_g + 1.2\alpha_g^2)Re_s^{0.7}Pr_g^{0.33}$	**$k-\varepsilon$ model:** $\frac{\partial}{\partial t}(\rho k) + \frac{\partial}{\partial x_i}(\rho k_{u_i}) = \frac{\partial}{\partial x_j}\left[(\mu + \frac{\mu_i}{\sigma_k})\right] + G_k + G_b - \rho\varepsilon - Y_m + S_k$ $\frac{\partial}{\partial t}(\rho\varepsilon) + \frac{\partial}{\partial x_i}(\rho\varepsilon_{v_i}) = \frac{\partial}{\partial x_j}\left[(\mu + \frac{\mu_i}{\sigma_\varepsilon})\frac{\partial\varepsilon}{\partial x_j}\right] + C_{1\varepsilon}\frac{\varepsilon}{k}(G_k + C_{3\varepsilon}G_b) - C_{2\varepsilon}\rho\frac{\varepsilon^2}{k} + S_\varepsilon$

Table 8. Definitions for variables in Table 7

Variable	Term	Variable	Term
ρ	Density	$\bar{\tau}_g$	Gas-phase stress tensor
v	Instantaneous velocity of gas/solid phase	β	Gas–solid interphase drag coefficient
s	Solid-phase subscript	U_s	Mean velocity of solid
g	Gas-phase subscript	G_k	Generation of turbulence kinetic energy due to the mean velocity gradients
S	Mass source term	G_b	Generation of turbulence kinetic energy due to buoyancy
R_c	Reaction rate	Y_m	Contribution of fluctuating dilatation in compressible turbulence to the overall dissipation rate
γ_c	Stoichiometric coefficient	S_ε	User-defined source term
M_c	Molecular weight	S_k	User-defined source term
R	Universal gas constant	$\vec{Q}_{pq}$	Heat transfer intensity between fluid phase p and solid phase q
T	Temperature of gas mixture	$\vec{q}_q$	Heat flux
p	Gas pressure	S_q	Source term due to chemical reactions
Y_i	Mass fraction	h_{pq}	Enthalpy of the interface
M_i	Molecular weight of each species	k_p	Thermal conductivity for phase p
Re_s	Reynolds number based on diameter of solid phase and relative velocity	Pr_g	Prandtl number of the gas phase

Modeling Tools/Software for an EMIPG Reactor

In the past, researchers of WtE technologies have typically relied on experimental setup to gain an understanding of the multiple physical–chemical phenomena that take place within the system [60]. Fortunately, with the advent of technology, computational power has evolved in parallel with numerical model solver efficiency [61]. Due to the rapid advancement in both computation and calculation capacity, CFD is a tool that can be used to design, optimize, and predict processes within WtE systems [49]. CFD modeling software uses mathematical models to solve complicated partial differential equations of conservation laws for mass, momentum, and energy, as well as their theoretical and empirical correlations [49]. By synthesizing these models, CFD software has the ability to design reactor simulations incorporating structural, thermal, and chemical analysis [62]. Computational software such as Aspen Plus, Aspen HYSYS, and chemCAD have been used within the literature as plasma gasification modeling tools; however, they are limited in their application. The applications of Aspen Plus, Aspen

HYSYS, and chemCAD are focused on process simulation and chemical process simulation only [41]. ANSYS Fluent, OpenFoam, and COMSOL Multiphysics software typically allow for a wide application of multiphysics problems. Barracuda is a simulation software that is tailored for fluidized reactor bed simulation and design. ANSYS CFX uses a vertex-centered solver approach within its software which tailors its application more towards CFD problems that apply to turbomachinery. The specifications for each software package are shown in Table 9. CFD modeling provides multiple benefits to simulate an EMIPG system reactor. It allows for the testing of multiple configurations of reactor geometry; the identification of critical variables that affect the process; and the demonstration of velocity vector profiles, average pressure drop curves slopes, and temperature and species profiles. Modeling also prevents expensive and tedious experimentation [48].

Table 9. Comparison of CFD modeling software packages

Sources	CFD Software	Developer	Quick Specifications
[56], [62], [63]	Fluent	ANSYS	• FRC/EDM model which directly applies to a plasma reactor system • Allows for user-defined functions to be created but has built-in modules for dealing with reactor phenomena • Built-in modules for chemical species descriptions and functions • Can be used for a wide array of multiphysics problems • Tested and verified readily available models • Cell-centered approach allows for low computational energy in mass, momentum, and energy conservation models • Has been used to model MW plasma and other plasma reactors
[56], [64], [65]	OpenFoam	Open CFD Ltd.	• Free, open-source solver platform allows for synthesis of different solver methods • Can be used for a wide array of multiphysics problems • Independently tested, released every six months

			• Has been used to model plasma gasification reactors but requires user-defined functions.
[56], [66], [67]	CFX	ANSYS	• Industry-leading CFD software for turbomachinery applications • Can be used for a wide array of multiphysics problems • Vertex-centered approach • Not suitable for plasma reactor modeling
[56], [68], [69]	COMSOL Multiphysics	COMSOL Inc.	• Can be used for a wide array of multiphysics problems • Software designed for simulations in all fields of scientific study. • Allows for solutions that deal with electrical, structural, acoustics, fluid, heat, and chemical disciplines • Has been used extensively in modeling MW plasma and other plasma reactors
[56], [70], [71]	Barracuda	CPFD Software LLC.	• Good for industrial-scale simulations • Designed for applications like fluidized bed operation and design • Deals exclusively with gas-particle fluidized reactors • Not suitable for modeling an EMIPG system

Forward Look

MW plasma gasification is limited in nature by the frequency of electromagnetic energy. The magnetron, which is the driving force of electromagnetic energy in the system, is constrained in size, creating difficulty when scaling the system. To overcome this system constraint and still drive an even plasma flame within a large-scale reactor, multiple magnetrons can be used to distribute electromagnetic energy into the reactor. A demonstration of this configuration in a scaled-up unit can be found in research conducted by Uhm et. al. Uhm et al. used two microwave steam-plasma units to provide an even temperature plasma to a large, cylindrical reactor with a diameter of 90 cm and a height of 180 cm. This research utilized low-grade coals for a feedstock and found a cold gas efficiency of hydrogen-rich syngas of 84% [16]. The high efficiency of this system

demonstrates the potential of microwave plasma to be scaled in order to convert waste into energy.

Conclusion

Plasma gasification offers the ability to produce clean energy and destroy hazardous waste. This technology has not matured for commercial WtE applications. This review focused on experimental microwave-induced plasma gasification (EMIPG) system reactors. An EMIPG system is constituted by various components: power supply and microwave source, wave propagation section, plasma reactor, plasma-forming gases, carrier gas, feedstock inputs, and data collection equipment. Various chemical reactions convert feedstock into syngas. The rates of carrier gas and plasma-forming gas inputs, the operational power of the system, and the rate of the feedstock injection affect the chemical reaction kinetics. The temperature and turbulence play a significant role in determining the rate and distribution of these chemical conversions within an EMIPG reactor. The Navier–Stokes equations for mass, momentum, and energy and the k-epsilon model for turbulence are used to describe the fluid motion and temperature within the reactor. Most studies used the Eulerian–Eulerian approach to model the gas and solid phases. Since the complexity of these mathematical models is significant, CFD software is used to solve the models of multiphysics phenomena happening within the reactor. The CFD software solves the mathematical models describing the reactor by using numerical methods such as the finite volume method. A CFD model can allow optimization of the

system, as well as a better understanding of how the system converts various feedstocks, such as plastics, electronic wastes, and COVID-19 biomedical waste.

II. Scholarly Article 2. Artificial Neural Networks and Gradient Boosted Machines Used for Regression to Evaluate Gasification Processes: A Review

Abstract

Waste-to-Energy technologies have the potential to dramatically improve both the natural and human environment. One type of waste-to-energy technology that has been successful is gasification. There are numerous types of gasification processes and in order to drive understanding and the optimization of these systems, traditional approaches like computational fluid dynamics software have been utilized to model these systems. The modern advent of machine learning models has allowed for accurate and computationally efficient predictions for gasification systems that are informed by numerous experimental and numerical solutions. Two types of machine learning models that have been widely used to solve for quantitative variables that are of predictive interest in gasification systems are gradient boosted machines and artificial neural networks. In this article, the reviewed literature used either gradient boosted machines or artificial neural networks to successfully model gasification systems. The review of such literature allows for a comparison in machine learning model architecture and resultant accuracy as well as an insight into what parameters are being used to inform the models and to make predictions.

Short Summary

This article compares a variety of machine learning models that have been used to successfully model gasification systems. Through the comparison of the literature, the accuracy of these machine learning models can offer insight into successful machine learning model architecture for gasification systems.

Introduction

Waste-to-Energy (WtE) technologies are of growing interest since they offer a multivariate solution to the sustainability dilemma: minimizing waste streams and returning both energy and materials. WtE technologies are typically categorized into thermal, biochemical, or mechanical processes. Previously, thermal technologies posed a number of adverse effects to the environment and human health, as poor-quality combustion can lead to the emission of undesirable pollutants such as NOx, SOx, dioxins, and furans. Fortunately, current advancements in combustion and air pollution control technologies have allowed thermal WtE technologies to achieve efficient energy and material recovery while minimizing adverse effects on the environment and human health[72].

Gasification is one of the most common alternatives to combustion as a means of proper thermal treatment of municipal solid waste (MSW) [13], [73]–[75]. Gasification uses a thermal process coupled with a reduced oxygen environment of a reactor to convert the large molecules within MSW into small molecules[76]–[78]. Gasification is typically aided by the initial treatment of a high temperature combustion process of the

MSW called pyrolysis. Through pyrolysis, a combustible gas known as a syngas is partially formed and primarily consists of H_2, CH_4, CO_2, and CO. Once finally treated in the gasification stage, the syngas can be used to generate energy. The different types of pyrolysis used with gasification are flash, fast, and slow[79]. Additionally, the reactors themselves have different configurations: fixed-bed, fluidized-bed, rotary kiln, ablative, and screw[79]. Modern gasification systems have the ability to reduce the original MSW stream volume by 80-95% and achieve an exergy efficiency of up to 46.7%[80], [81]. Due to the complex nature of gasification systems, many different approaches have been taken to model these systems. Recently, traditional approaches like computational fluid dynamics (CFD) modeling and small-scale experiments have allowed for machine learning (ML) models to utilize data obtained by the previous research methods. This data then can build an accurate and easy-to-use model of gasification systems. ML models can make sense of the non-linear data attributed to the gasification process due to the wide range of varying system parameters such as temperature, MSW stream, pressure, heating rates, and reactor residence. By combining the available datasets of the parameters surrounding different gasification systems, ML models allow researchers to gain an accurate understanding of the nuanced system. ML models are becoming more popular within research surrounding gasification and WtE technologies, as they are much more cost-effective than experimental iterations. They also can achieve a higher accuracy than traditional CFD models.

ML models are used to solve for classification or regression prediction problems. Classification ML models create a mapping function by using input variables and discrete

output variables. The output variables of classification ML models belong to a label or category, and thus, the mapping function is used to predict whether the outcome will be a label or category. Regression ML models create a mapping function by using input variables and continuous output variables. The output variables of regression ML models are normally a real-value quantity; therefore, the mapping function is used to predict what the real-value quantity of the outcome is. ML regression models are useful for application with gasification systems because they are able to predict real-value system performance quantities such as syngas composition, remaining mass, lower heating value (LHV), and total syngas yield[81]–[85]. Two ML regression models that are commonly used with gasification systems are artificial neural networks (ANNs) and gradient boosted machines (GBMs).

The purpose of this paper is to conduct a discussion of ANN and GBM ML models that are used with gasification systems. This discussion will first provide insight as to what gasification is and the key parameters that are used to describe the system, the literature that links ML models to gasification, and how the ANN and GBM models work. It will then analyze what statistical methods are used to evaluate the models and successful synthesis of gasification with ANN and GBM models that have been found in the literature.

Materials and Methods

This discussion focuses on gasification systems that are used for WtE processes and ML models, specifically ANNs and GBMs for regression, that are applied to these

systems. This review contains 74 peer-reviewed journal articles. Searches for reviewed journal articles were conducted on databases such as ScienceDirect, IEEE Explore, Google Scholar, and SCOPUS. Search terms that were used to find reviewed journal articles consisted of the following key words: “Machine Learning”, “Gasification”, “Regression Analysis”, “Neural Networks”, “Gradient Boosted Machines”.

The Gasification Process

Gasification is a thermal process in which a waste feedstock is decomposed into a syngas that can be used as a source of energy. The reaction that describes the conversion process of waste feedstock into the valuable syngas and other constituents is shown in Equation 1. The product syngas contains non-condensable gases such as H, CO, CO_2, H_2O, N_2, and some lighter hydrocarbons[86].

$$waste\ feedstock + heat \rightarrow syngas + tar + char \quad (1)$$

An elevated temperature must be applied in order to assist in the conversion from the input waste feedstock to a syngas. The typical temperature range in which gasification takes place is between 900-1500℃[87]. Some of the notable byproducts from the gasification process found in Equation 1 are tar and char. Tar consists of larger hydrocarbons that are a product of the gasification process and develop into a viscous substance[88]. Char consists of solids that are entrained within the product syngas and are composed of solid carbon and inorganic ash[89]. Char and tar byproducts should be minimized as they can lead to erosion, corrosion, and plugging of the gasification systems that can necessitate maintenance and decrease process efficiency[90]. Multiple

process stages are employed to the gasification process in order to minimize the overall impact that char and tar have on the operational condition of the system. By using multiple stages, the waste feedstock can first be treated at a lower temperature (pyrolysis) allowing for initial char removal by the first reactor and cyclone before it enters the gasification reactor[91]. An example of a multi-stage gasification process and the separation of pyrolysis from gasification is illustrated in Figure 4. It is important to note that the tar is broken down to non-condensable gases in the final gasification step with the aid of oxygen[86]. Tar will be reduced to lighter hydrocarbons, hydrogen, and carbon monoxide in the final step process so that the heating value of tar will be retained within the product syngas[86].

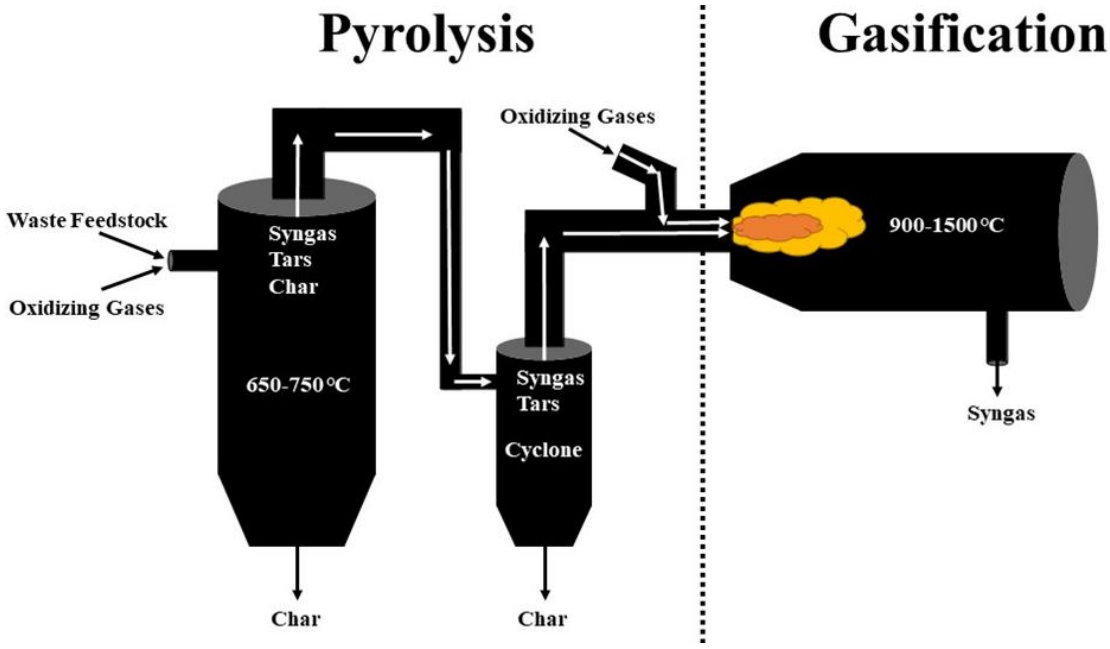

Figure 4. Schematic representation of a multi-stage gasification process

The gasifier component of the multi-stage system can be classified by the parameters that describe the reactor. Fixed bed and fluidized bed reactors are two types of

classifications for gasification reactors. A fixed bed reactor holds the waste feedstock in relative place during the combustion process within the surrounding walls of the reactor[92]. A fluidized bed reactor allows the waste feedstock to move freely during the combustion process within the surrounding walls of the reactor[92]. Gasification reactors can be classified further based on the direction of flow within the reactor. In downdraft gasifiers, both the waste feedstock and any oxidating agent moves downward. However, in updraft gasifiers, the waste feedstock moves downward while the oxidating agents move upward[93].

Important Gasification Process Terminology

It is important to know the terminology used to describe different parameters within the gasification process in order to understand how ML predictive models can be applied to these processes. This important terminology describes the inputs and outputs of the gasification system. Predicting the outputs of a gasification system from the inputs allows for the development of better and more efficient systems. Table 10 defines the important terminology relevant to gasification systems.

Table 10. Important terminology describing the gasification process

Term	**Abbreviation**	**Description**
Moisture Content	MC	The moisture content of the input waste feedstock (fuel)[94].
Lower Heating Value	LHV	The net heat of combustion[95]. Specifically relating to the created syngas.
Lower Heating Value of Products	LHV_p	The sum of the LHV of the syngas and the calorific value of entrained char and tar[81].

Reduction Zone Temperature	RZT	Portion of the gasifier directly above the combustion zone. This zone occurs once all the oxygen and gasifying media from the reaction is gone[96], [97]. In this zone the CO_2 and water vapor entrained by the gas flow have been reduced to CO and H_2[96]–[98].
Equivalence Ratio	ER	The ratio of actual air fuel to the stoichiometric air fuel[99].
Injected Steam Ratio	ISR	The ratio of steam to dry feedstock[100].
Steam Flow Rate	SFR	Rate of steam flow input in (kg/h)[84].
Space Velocity	SV	The ratio of entering volumetric flow rate and the reactor volume[85].
Particle Size	None	Size of the entering waste feedstock[85].
Syngas Yield	GY	Yield of the syngas output[81].
Atmosphere Type	ATM	Level of CO_2 and N_2 within the reactor adjusted by experimental control[101].
Heating Rate	HR	The heating conditions within the reactor adjusted by experimental control[102].
Ash Content	A	Proximate analysis and resultant ash content of waste feedstock[103].
Gasifier Bottom Temperature	GBT	Temperature at the bottom of the gasification reactor[84].
Volatile Compounds	VC	Proximate analysis and resultant volatile compound content of waste feedstock[103].
Fixed Carbon	FC	Proximate analysis and resultant fixed carbon content of waste feedstock[103].

Machine Learning and Gasification Literature

Elsevier's abstract and citation database, Scopus, was used to scrub for articles using the Boolean search phrase: "Machine Learning" AND "Gasification". This Boolean search phrase returned 40 documents that contained both of the search terms within either their title, abstract, and keywords [104], [105], [114]–[123], [106], [124]–[133], [107], [134]–[143], [108]–[113]. CitespaceV software used the data collected from the title, abstract, keywords, and references for each document. The software was able to visually model the interconnectedness of matching key terms between the documents from the

Scopus research database that used the Boolean search phrase. This visualization is shown in Figure 5. The visualization in Figure 5 utilized six different clusters to connect key terms that matched from the title, abstract, and keywords between the documents. The strength between the matching key terms is visualized by the thickness of each line that connects the individual document nodes. Matching key terms that appeared more frequently are visualized by a larger text font. Figure 5 exhibits that some of the stronger key terms were: “machine learning”, “underground coal gasification”, “artificial intelligence”, “neural network”, “regression analysis”, and “artificial neural network”. Furthermore, the color of the line between each node document indicates the year in which the document was published. The recency of the connection between ML models and gasification is demonstrated by the oldest document connecting these search terms

being published in 2013. In fact, all the documents found in Scopus only have a nine-year timespan between the document with the earliest publication date and the latest.

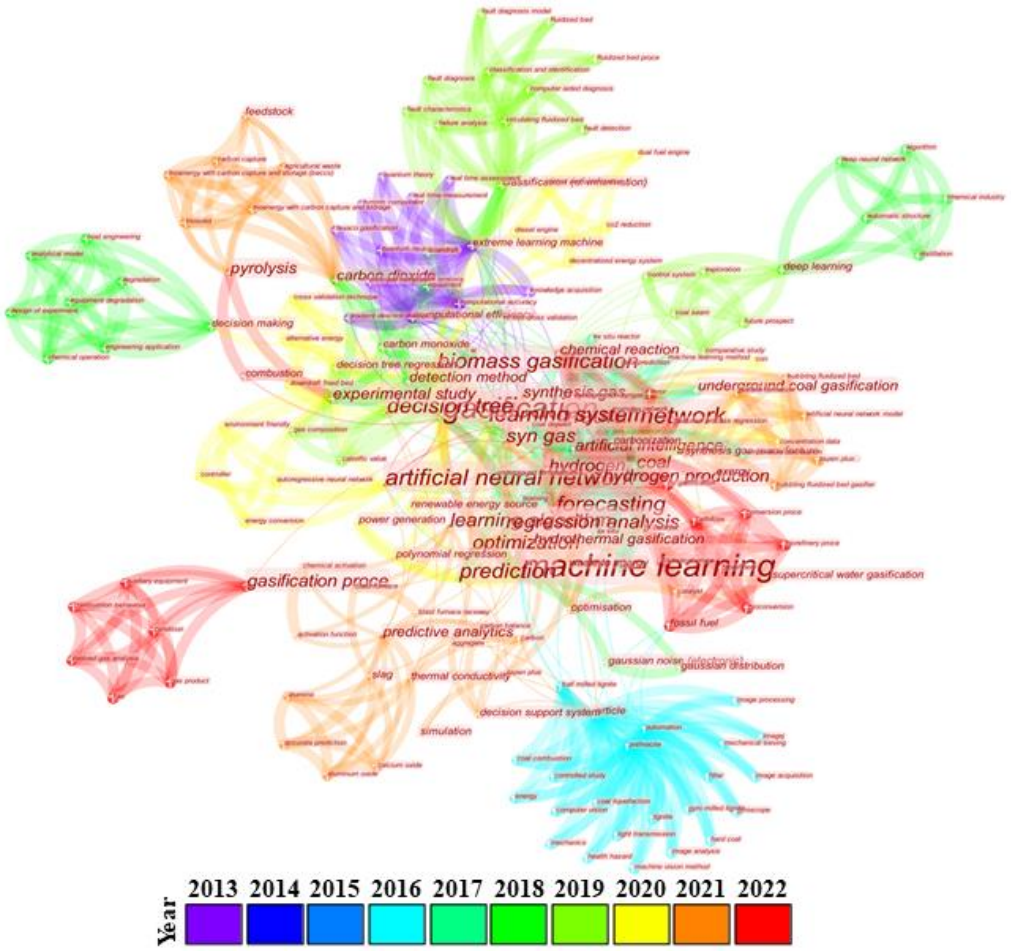

Figure 5. CitespaceV visualization network of matching key terms between Scopus documents

ANN models with Gasification

ANN models utilize available data in order to learn a process similar to the human brain. The advantage of ANN models over other types of theoretical and empirical models is that ANN models are universal approximators and therefore allow for close prediction accuracy in a variety of situations[81]. ANN models have been applied across

a wide variety of fields including: weather prediction, signal processing, pattern recognition, function approximation, and process simulation[81]. Like many predictive models, the dataset that an ANN model utilizes to create its prediction is typically a limiting factor of how accurate the ANN model predictions can get. Since the ANN model creates a unique predictive model based off the dataset it is fed, the more data that an ANN model can receive on the situation, then the more likely it will be representative of the non-linearities and "randomness" that exist within the dataset.

Two types of ANN architectures used for gasification modeling are a multilayer feed-forward neural network with multiple input and multiple output (MIMO) variables and multiple input and single output (MISO) model. Figure 6 shows a MIMO model with both dual and single layers. Both models shown in Figure 6 contain an input layer, a hidden layer or layers, and an output layer. The inputs and outputs of each layer are shown using typical parameters found in the literature used when modeling gasification. A range of all inputs used with gasification ANN models are shown in the "Input Parameters" column of Table 11 along with a range of all output parameters shown by

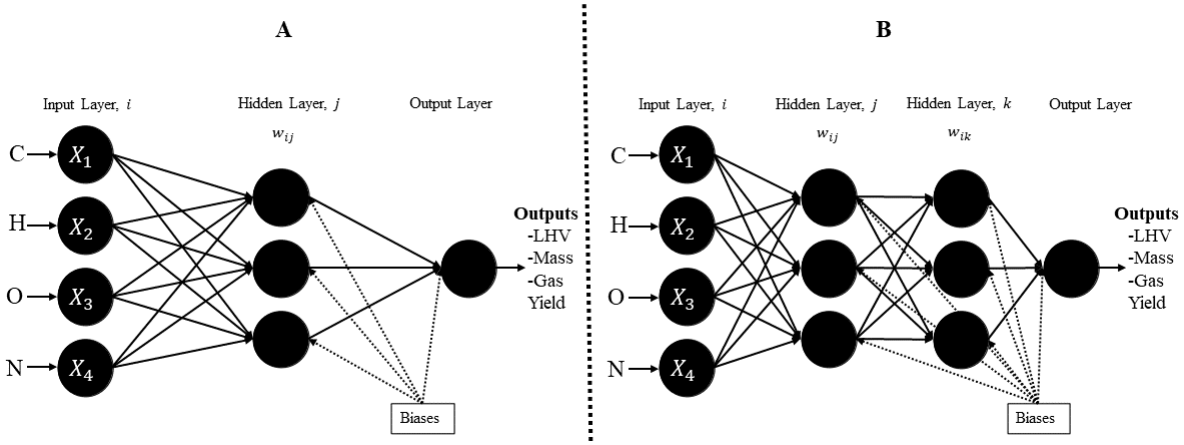

Figure 6. Schematic diagram of a MIMO ANN model (A) one hidden layer (B) two hidden layers

the “Predictive Parameters” column. Table 11 also indicates the type of ANN model used in the “ANN model” column, the type of gasification process being modeled in the “System Description” column, and the number of layers in the ANN model in the “Number of Layers” column.

In the ANN model, each neuron that is not in the input layer uses a non-linear transfer function when moving towards the output layer[81]. The transfer functions that have been utilized with gasification and ANN models found in the literature are shown in the “Transfer Function” column of Table 11. When the ANN models exceed a single hidden layer, they are able to utilize the same or different transfer function between each respective layer. Therefore, an ANN model that has two layers is able to use two of the same or different transfer functions. When the ANN model transitions from the final hidden layer to the output layer, all of the ANN models in the literature review used a pure linear transfer function. Table 11 shows that three different types of transfer functions have been used with ANN models predicting gasification. These three different types of transfer functions are a hyperbolic tangent sigmoid function (tansig), a logarithmic sigmoid function (logsig), and a rectified linear activation function (ReLU). The activation functions are shown in Equations 2, 3, and 4, respectively. Different transfer functions, and combinations thereof, can create different prediction accuracies for the same dataset. Therefore, it is important to iterate combinations of transfer functions when setting up an ANN model in order to find the best fit function for the gasification system.

$$\text{tansig: } f(x) = \frac{e^{x} - e^{-x}}{e^{x} + e^{-x}} \quad (2)$$

$$\text{logsig: } f(x) = \frac{1}{1 + e^{-x}} \quad (3)$$

$$\text{ReLU: } f(x) = \max(0, x) \quad (4)$$

The output of the MIMO ANN Model with a single hidden layer in Figure 6 is shown as y_j in Equation 5. In Equation 5, neurons, x_i, distribute the input signals to the hidden layer, j [81]. The neurons in hidden layers sum up the input signal x_i, after multiplying by the weight w_{ij}. f represents the activation function, d is the dimension of the network, l is the number of layers, and w_{ij}^{l} is the weight which belongs to the network with l layers and has i input and j hidden layers[81]. The MIMO ANN model with a single hidden layer in Figure 6 weights are described mathematically in Equation 6.

$$y_j = f\left(\sum_{i=0}^{d^{(l-1)}} (w_{ij}^{l} x_i^{l-1})\right) \quad (5)$$

$$w_{ij}^{l} \in \begin{cases} 1 \le l \le L \ layers \\ 0 \le i \le d^{l-1} \ input \\ 1 \le j \le d^{l} \ output \end{cases} \quad (6)$$

Table 11 shows the number of neurons in the “Neurons” column and the different number of layers in the “Number of Layers” column for different ANN models. Once the ANN model has reached an output value y_{ij}, it then utilizes a training function to train the neural network to recognize an input and map to an output. All the research found in the literature review used the Levenberg-Marquardt back propagation algorithm (LMBPA) in order to train the neural network. This is shown in the “Training Function”

column of Table 11. The LMBPA gives accurate results for moderate sized neural networks[81]. In tandem with a training function, the ANN model also uses a learning function in order to manipulate the individual weights and thresholds of the network. All the research found in the literature review showed that a gradient descent (GD) function was employed by the ANN model. This is shown in the "Learning Function" column in Table 11. Equation 7 shows the LMBPA where the Jacobian, J, is calculated using backpropagation, followed by the Hessian $H = J^T J$ and the gradient calculation ($g = J^t e$) where e is the network error[81]. In this function, μ is a scalar, and after each successful step, the value of μ is increased or decreased as determined by the cost function. The LMBPA minimizes the mean squared error (MSE) between the target output and the calculated output.

$$x_{k+1} = x_k - [J^T J + \mu I]^{-1} J^t e \quad (7)$$

In order to check the accuracy of the ANN model, the dataset is randomly divided into proportions for training, validation, and testing purposes. The proportions used for respective training, validation, and testing purposes by ANN models used to predict gasification systems are shown by the "Data Division" column in Table 11. Additionally, some ML models employed cross-validation within the network, allowing for the training, validation, and testing data to be re-split multiple times. This process finds the best representative model. Whether an ANN model that is predicting gasification systems used cross validation or not is shown in by the "Cross Validation" column in Table 11.

Table 11. ANN ML models used with gasification

ANN Model	System Description	Number of Layers	Input Parameters	Predictive Parameters	Transfer Function	Training Function	Learning Function	Cross Validation	Dataset	Data Division	Epochs Run	Neurons	Test Accuracy	Source
MISO	MSW in fluidized bed reactor	1	C, H, N, S, O, MC, A, ER, T	LHV	tansig	LMBPA	GD	Yes	N/A	70%TR/15%V/15%T	up to 12	9	MSE=0.0086	[81]
MISO	MSW in fluidized bed reactor	1	C, H, N, S, O, MC, A, ER, T	LHV	logsig	LMBPA	GD	Yes	N/A	70%TR/15%V/15%T	up to 12	30	MSE=0.0077	[81]
MISO	MSW in fluidized bed reactor	1	C, H, N, S, O, MC, A, ER, T	LHVp	tansig	LMBPA	GD	Yes	N/A	70%TR/15%V/15%T	up to 12	12	MSE=0.0024	[81]
MISO	MSW in fluidized bed reactor	1	C, H, N, S, O, MC, A, ER, T	LHVp	logsig	LMBPA	GD	Yes	N/A	70%TR/15%V/15%T	up to 12	30	MSE=0.0021	[81]
MISO	MSW in fluidized bed reactor	1	C, H, N, S, O, MC, A, ER, T	GY	tansig	LMBPA	GD	Yes	N/A	70%TR/15%V/15%T	up to 12	6	MSE=0.0004	[81]
MISO	MSW in fluidized bed reactor	1	C, H, N, S, O, MC, A, ER, T	GY	logsig	LMBPA	GD	Yes	N/A	70%TR/15%V/15%T	up to 12	8	MSE=0.0003	[81]
MIMO	MSW in fluidized bed reactor	1	C, H, N, S, O, MC, A, ER, T	LHV, LHVp, GY	tansig	LMBPA	GD	Yes	N/A	70%TR/15%V/15%T	up to 12	11	MSE=0.0035	[81]
MIMO	MSW in fluidized bed reactor	1	C, H, N, S, O, MC, A, ER, T	LHV, LHVp, GY	logsig	LMBPA	GD	Yes	N/A	70%TR/15%V/15%T	up to 12	28	MSE=0.0031	[81]
MISO	MSW in fluidized bed reactor	2	C, H, N, S, O, MC, A, ER, T	LHV	tansig/tansig	LMBPA	GD	Yes	N/A	70%TR/15%V/15%T	up to 12	4/12	MSE=0.00852	[81]
MISO	MSW in fluidized bed reactor	2	C, H, N, S, O, MC, A, ER, T	LHV	tansig/logsig	LMBPA	GD	Yes	N/A	70%TR/15%V/15%T	up to 12	10/15	MSE=0.00837	[81]
MISO	MSW in fluidized bed reactor	2	C, H, N, S, O, MC, A, ER, T	LHV	logsig/logsig	LMBPA	GD	Yes	N/A	70%TR/15%V/15%T	up to 12	9/15	MSE=0.00810	[81]
MISO	MSW in fluidized bed reactor	2	C, H, N, S, O, MC, A, ER, T	LHV	logsig/tansig	LMBPA	GD	Yes	N/A	70%TR/15%V/15%T	up to 12	4/12	MSE=0.00840	[81]
MISO	MSW in fluidized bed reactor	2	C, H, N, S, O, MC, A, ER, T	LHVp	tansig/tansig	LMBPA	GD	Yes	N/A	70%TR/15%V/15%T	up to 13	4/13	MSE=0.00251	[81]
MISO	MSW in fluidized bed reactor	2	C, H, N, S, O, MC, A, ER, T	LHVp	tansig/logsig	LMBPA	GD	Yes	N/A	70%TR/15%V/15%T	upt to 12	4/14	MSE=0.00247	[81]
MISO	MSW in fluidized bed reactor	2	C, H, N, S, O, MC, A, ER, T	LHVp	logsig/logsig	LMBPA	GD	Yes	N/A	70%TR/15%V/15%T	up to 12	4/13	MSE=0.00229	[81]
MISO	MSW in fluidized bed reactor	2	C, H, N, S, O, MC, A, ER, T	LHVp	logsig/tansig	LMBPA	GD	Yes	N/A	70%TR/15%V/15%T	up to 12	4/10	MSE=0.00234	[81]
MISO	MSW in fluidized bed reactor	2	C, H, N, S, O, MC, A, ER, T	GY	tansig/tansig	LMBPA	GD	Yes	N/A	70%TR/15%V/15%T	up to 12	6/6	MSE=0.00057	[81]
MISO	MSW in fluidized bed reactor	2	C, H, N, S, O, MC, A, ER, T	GY	tansig/logsig	LMBPA	GD	Yes	N/A	70%TR/15%V/15%T	up to 12	6/10	MSE=0.00055	[81]
MISO	MSW in fluidized bed reactor	2	C, H, N, S, O, MC, A, ER, T	GY	logsig/logsig	LMBPA	GD	Yes	N/A	70%TR/15%V/15%T	up to 12	6/5	MSE=0.00051	[81]
MISO	MSW in fluidized bed reactor	2	C, H, N, S, O, MC, A, ER, T	GY	logsig/tansig	LMBPA	GD	Yes	N/A	70%TR/15%V/15%T	up to 12	5/6	MSE=0.00056	[81]
MIMO	MSW in fluidized bed reactor	2	C, H, N, S, O, MC, A, ER, T	LHV, LHVp, GY	tansig/tansig	LMBPA	GD	Yes	N/A	70%TR/15%V/15%T	up to 12	6/12	MSE=0.00353	[81]
MIMO	MSW in fluidized bed reactor	2	C, H, N, S, O, MC, A, ER, T	LHV, LHVp, GY	tansig/logsig	LMBPA	GD	Yes	N/A	70%TR/15%V/15%T	up to 12	8/15	MSE=0.00346	[81]
MIMO	MSW in fluidized bed reactor	2	C, H, N, S, O, MC, A, ER, T	LHV, LHVp, GY	logsig/logsig	LMBPA	GD	Yes	N/A	70%TR/15%V/15%T	up to 12	7/15	MSE=0.00347	[81]
MIMO	MSW in fluidized bed reactor	2	C, H, N, S, O, MC, A, ER, T	LHV, LHVp, GY	logsig/tansig	LMBPA	GD	Yes	N/A	70%TR/15%V/15%T	up to 12	7/15	MSE=0.00357	[81]
MISO	Biomass in fixed bed downdraft gasifiers	1	C,H,O, A , MC, and RZT	CH4	tansig	LMBPA	GD	Yes	63	70% TR/30%T	1000	5	R^2=0.9928, RMSE= 0.0523	[82]

MISO	Biomass in fixed bed downdraft gasifiers	1	C,H,O, A , MC, and RZT	CO	tansig	LMBPA	GD	Yes	63	70% TR/30%T	1000	5	R^2=0.09916, RMSE=0.0688	[82]
MISO	Biomass in fixed bed downdraft gasifiers	1	C,H,O, A , MC, and RZT	CO2	tansig	LMBPA	GD	Yes	63	70% TR/30%T	1000	4	R^2=0.9887, RMSE=0.0873	[82]
MISO	Biomass in fixed bed downdraft gasifiers	1	C,H,O, A , MC, and RZT	H2	tansig	LMBPA	GD	Yes	63	70% TR/30%T	1000	3	R^2=0.09855, RMSE=0.0915	[82]
MISO	Biomass in circulating fluidized bed gasifiers	1	A, M.C., C,H,O, ER, T	CO	tansig	LMBPA	GD	Yes	90	80%TR/20%T	N/A	2	R^2=0.9995, RMSE=0.144	[83]
MISO	Biomass in circulating fluidized bed gasifiers	1	A, M.C., C,H,O, ER, T	CO2	tansig	LMBPA	GD	Yes	90	80%TR/20%T	N/A	2	R^2=0.998, RMSE=0.093	[83]
MISO	Biomass in circulating fluidized bed gasifiers	1	A, M.C., C,H,O, ER, T	CH4	tansig	LMBPA	GD	Yes	90	80%TR/20%T	N/A	2	R^2=0.9985, RMSE=0.049	[83]
MISO	Biomass in circulating fluidized bed gasifiers	1	A, M.C., C,H,O, ER, T	H2	tansig	LMBPA	GD	Yes	90	80%TR/20%T	N/A	2	R^2=0.9771, RMSE=0.332	[83]
MISO	Biomass in circulating fluidized bed gasifiers	1	A, M.C., C,H,O, ER, T	GY	tansig	LMBPA	GD	Yes	90	80%TR/20%T	N/A	2	R^2=0.9967, RMSE=0.036	[83]
MISO	Biomass in circulating fluidized bed gasifiers	1	A, MC, C, H, O, ER, T, ISR	CO	tansig	LMBPA	GD	Yes	180	80%TR/20%T	N/A	2	R^2=0.9934, RMSE=0.790	[83]
MISO	Biomass in circulating fluidized bed gasifiers	1	A, MC, C, H, O, ER, T, ISR	CO2	tansig	LMBPA	GD	Yes	180	80%TR/20%T	N/A	2	R^2=0.984, RMSE=0.417	[83]
MISO	Biomass in circulating fluidized bed gasifiers	1	A, MC, C, H, O, ER, T, ISR	CH4	tansig	LMBPA	GD	Yes	180	80%TR/20%T	N/A	2	R^2=0.9911, RMSE=0.155	[83]
MISO	Biomass in circulating fluidized bed gasifiers	1	A, MC, C, H, O, ER, T, ISR	H2	tansig	LMBPA	GD	Yes	180	80%TR/20%T	N/A	2	R^2=0.9958, RMSE=0.624	[83]
MISO	Biomass in circulating fluidized bed gasifiers	1	A, MC, C, H, O, ER, T, ISR	GY	tansig	LMBPA	GD	Yes	180	80%TR/20%T	N/A	2	R^2=0.9919, RMSE=0.075	[83]
N/A	Rice husks in fixed bed updraft gasifier	N/A	ER, GBT, and SFR	H2	N/A	N/A	N/A	N/A	74	70%TR/30%T	N/A	N/A	R^2=0.81	[84]
N/A	Rice husks in fixed bed updraft gasifier	N/A	ER, GBT, and SFR	CH4	N/A	N/A	N/A	N/A	74	70%TR/30%T	N/A	N/A	R^2=0.73	[84]
N/A	Rice husks in fixed bed updraft gasifier	N/A	ER, GBT, and SFR	CO	N/A	N/A	N/A	N/A	74	70%TR/30%T	N/A	N/A	R^2=0.63	[84]
N/A	Rice husks in fixed bed updraft gasifier	N/A	ER, GBT, and SFR	CO2	N/A	N/A	N/A	N/A	74	70%TR/30%T	N/A	N/A	R^2=0.78	[84]
N/A	Rice husks in fixed bed updraft gasifier	N/A	ER, GBT, and SFR	N2	N/A	N/A	N/A	N/A	74	70%TR/30%T	N/A	N/A	R^2=0.70	[84]
MIMO	Pyrolysis of pine sawdust	1	SV, T, Particle Size	H2, CO, CH4, CO2	logsig	LMBPA	N/A	Yes	N/A	85%TR/15%T	N/A	7	MSE=0.01	[85]
MISO	Pyrolysis of cattle manure	2	T, HR, and ATM	Remaining Mass	ReLU	LMBPA	N.A	Yes	85416	80%TR/ 20%T	N/A	N/A	RMSE=9.666, R^2=0.8583	[101]

Where: A: Ash Content, MC: Moisture Content, S: Sulfur, ER: Equivalence Ratio, T: Temperature, RZT: Reduction Zone Temperature, LHV: , LHV_p: ISR: Injected Steam Ratio, GBT: Gasifier Bottom Temperature, SFR: Steam Flow Rate, ATM: Atmosphere Type, SV: Space Velocity, LMBPA: Levenberg-Marquardt Back-Propagation Algorithm, HR: Heating Rate, GD: Gradient Descent with Weight and Bias, TR: Train, T: Test, V: Validation, For Neurons Column: Layer 1/Layer 2

GBM models with gasification

GBM ML models utilize available data as an efficient solving tool for regression problems that can make predictions for datasets with complex non-linearities[144]. The GBM ML model uses an ensemble of weak predictive learners, known as decision trees, to create an accurate predictive model. Each weak predictive learner corrects on the predecessor's error through a gradient descent function that is used to minimize the error and thus fit the model[145], [146]. An illustration of a gross representation of the GBM process that shows how the model leverages an ensemble of weak predictive learners for a strong prediction tool is in Figure 7.

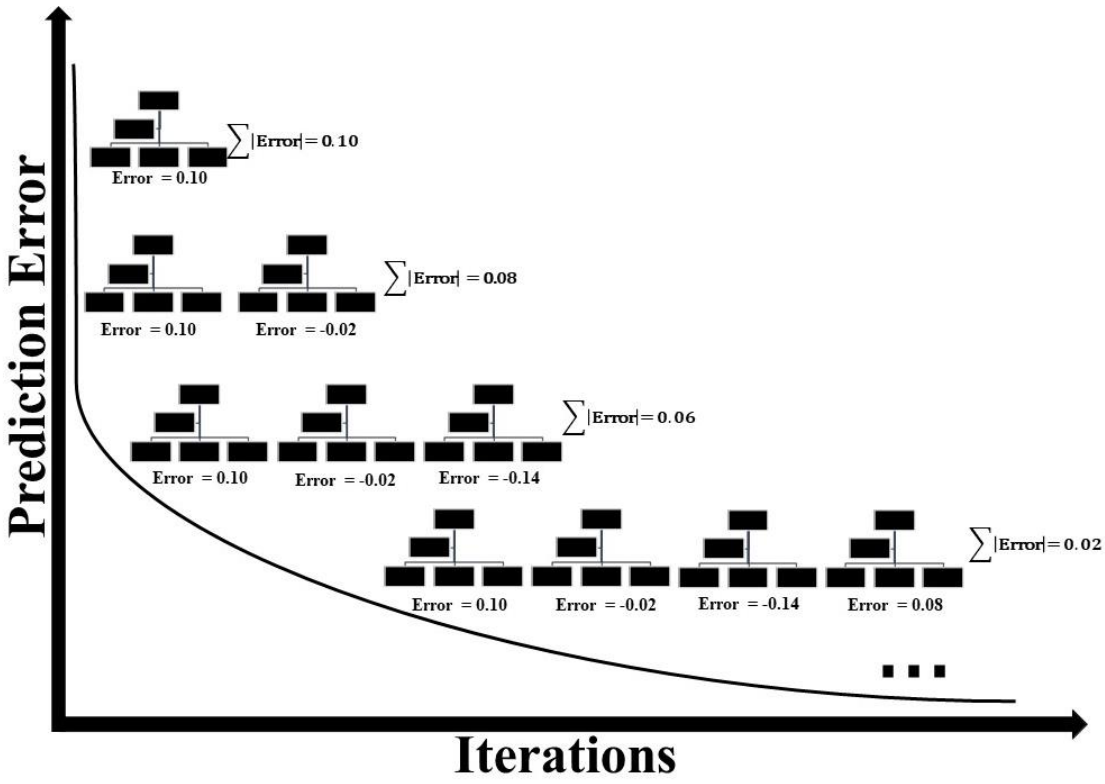

Figure 7. Gross representation of a GBM ML model

As shown in Figure 7, the GBM ML model minimizes the expected loss function through the use of decision trees[147]. The parameters of the GBM ML model include depth of trees, the learning rate, and the number of iterations[147]. The GBM algorithm is mathematically expressed as a summation of decision trees in Equation 8.

Generalized GBM model: $f_m(x) = \sum_{m=1}^{M} T(x, \theta_m),\ T(x, \theta_m)$ (8)

θ_m is the parameter of the decision tree and M is the number of decision trees. A gradient descent loss function is then used by the GBM ML model in order to optimize the next parameter, shown in Equation 9[145], [146].

GBM Loss Function: $\theta_{m+1} = \text{argmin} \sum_{t=1}^{N} L\big(y_t, F_m(x) + h(x, \theta_{m+1})\big)$ (9)

Table 12 provides an overview of different GBM models for regression found in the literature that were used for prediction of gasification systems. Similar to ANN ML models, GBM models also split the dataset into proportions to be used for testing, training, and validation of the model. Additionally, all GBM models used with gasification systems employed cross-validation within the algorithm in order to randomize the data multiple times and find the best-fit *m*.

Table 12. GBM ML models for regression used with gasification

GBM Model	System Description	Cross Validation	Input Parameters	Predictive Parameter	Dataset	Data Division	Test Accuracy	Source
GBR	Wet organic wastes	Yes	FC, OC	H2	295	90%TR/ 10%T	R^2=0.92, RMSE=2.07	[148]
GBR	Wet organic wastes	Yes	FC, OC	CH4	295	90%TR/ 10%T	R^2=0.90, RMSE=0.56	[148]
GBR	Wet organic wastes	Yes	FC, OC	CO2	295	90%TR/ 10%T	R^2=0.95, RMSE=1.3	[148]
GBR	Wet organic wastes	Yes	FC, OC	CO	295	90%TR/ 10%T	R^2=0.92, RMSE=0.39	[148]
GBR	Rice husks in fixed bed updraft gasifier	N/A	ER, GBT, SFR	H2	74	70%TR/ 30%T	R^2=0.82	[84]
GBR	Rice husks in fixed bed updraft gasifier	N/A	ER, GBT, SFR	CH4	74	70%TR/ 30%T	R^2=0.59	[84]
GBR	Rice husks in fixed bed updraft gasifier	N/A	ER, GBT, SFR	CO	74	70%TR/ 30%T	R^2=0.66	[84]
GBR	Rice husks in fixed bed updraft gasifier	N/A	ER, GBT, SFR	CO2	74	70%TR/ 30%T	R^2=0.77	[84]
GBR	Rice husks in fixed bed updraft gasifier	N/A	ER, GBT, SFR	N2	74	70%TR/ 30%T	R^2=0.78	[84]
XGB	Pyrolysis of algae	Yes	C, H, O, N	BY+C	85	75%TR/ 25%T	R^2= 0.2143	[103]
XGB	Pyrolysis of algae	Yes	H/C, O/C, N/C, T	BY+C	85	75%TR/ 25%T	R^2=0.6895	[103]
XGB	Pyrolysis of algae	Yes	FC, VC, T, A	BY+C	85	75%TR/ 25%T	R^2=0.8145	[103]
XGB	Pyrolysis of algae	Yes	C, H, O, N, T	BY+C	85	75%TR/ 25%T	R^2=0.6516	[103]
XGB	Pyrolysis of algae	Yes	H/C, O/C, N/C, T, PT, HR	BY+C	85, 64 for PT+HR	75%TR/ 25%T	R^2=0.7405	[103]

XGB	Pyrolysis of algae	Yes	H/C, O/C, N/C, A, FC, VC, T	BY+C	85	75%TR/ 25%T	R^2=0.7139	[103]
XGB	Pyrolysis of algae	Yes	C,H,O,N, PT, HR, T	BY+C	85, 64 for PT+HR	75%TR/ 25%T	R^2=0.7314	[103]
XGB	Pyrolysis of algae	Yes	C, H, O, N, H/C, O/C, N/C, T	BY+C	85	75%TR/ 25%T	R^2=0.7263	[103]
XGB	Pyrolysis of algae	Yes	C, H, O, N, A, FC, VC, T	BY+C	85	75%TR/ 25%T	R^2=0.7696	[103]
XGB	Pyrolysis of algae	Yes	C, H, O, N, H/C, O/C, N/C, PT, HR, T	BY+C	85, 64 for PT+HR	75%TR/ 25%T	R^2=0.7208	[103]
XGB	Pyrolysis of algae	Yes	C, H, O, N, A, FC, VC, PT, HR, T	BY+C	85, 64 for PT+HR	75%TR/ 25%T	R^2=0.7464	[103]
XGB	Pyrolysis of algae	Yes	C, H, O, N, H/C, O/C, N/C, A, FC, VC, T	BY+C	85	75%TR/ 25%T	R^2=0.7301	[103]
XGB	Pyrolysis of algae	Yes	C, H, O, N, H/C, O/C, N/C, A, FC, VC, PT, HR, T	BY+C	85, 64 for PT+HR	75%TR/ 25%T	R^2=0.7381	[103]
XGB	Pyrolysis of algae	Yes	H/C, N/C, A, PT, T	BY+C	85, 64 for PT+HR	75%TR/ 25%T	R^2=0.8440	[103]
GBR	Pyrolysis of cattle manure	Yes	T, HR, ATM	Remaining mass	85416	80%TR/ 20%T	R^2=0.9989, RMSE=0.820	[101]
GBR	Pyrolysis of textile dyeing sludge and incense sticks	Yes	BR, HR, ATM, T	Remaining mass	154000	80%TR/ 20%T	R^2=0.9937, RMSE=1.716	[102]
GBR	Pyrolysis of textile dyeing sludge and incense sticks	Yes	BR, HR, ATM, T	Derivative thermogravimetry	154000	80%TR/ 20%T	R^2=0.5978, RMSE=1.695	[102]
GBR	Pyrolysis of textile dyeing sludge and incense sticks	Yes	BR, HR, ATM, T	Differential scanning calorimetry	154000	80%TR/ 20%T	R^2=0.9077, RMSE=1.762	[102]

Where: GBR: Gradient Boosted Regression, XGB: eXtreme Gradient Boosted Regression, FC: Feedstock Composition, OC: Operational Conditions, FC: Fixed Carbon, VC: Volatile Compounds, PT: Pyrolysis Time, HR: Heating Rate, ATM: Atmosphere Type, BR: Blend Ratio, BY+C: Biochar Yield, TR: Train, T: Test

Performance Evaluation of ANN and GBM ML Models

The error for the ANN and GBM ML models used for regression predictions of gasification systems can be found in the "Test Accuracy" columns in Tables 11 and 12. The regression model accuracy for all the ML models in Tables 11 and 12 utilize one or multiple of four evaluation metrics. These four types of evaluation metrics utilized by the ML models are the mean absolute error (MAE), the mean standard error (MSE), the root mean squared error (RMSE), and the coefficient of determination (R^2). They are described respectively by Equations 10, 11, 12, and 13. These evaluation metrics are calculated by comparing the output created by the ML model and comparing it to the expected real value output found in the dataset. In the following equations $Y_{predicted}$ is the value generated by the ML model, Y_{actual} is the expected value on the test dataset, and n is the number of iterations of the ML model.

$$MAE = \frac{1}{n}\sum_{i=1}^{n}\left|Y_{predicted} - Y_{actual}\right| \quad (10)$$

$$MSE = \frac{1}{n}\sum_{i=1}^{n}\left(Y_{predicted} - Y_{actual}\right)^2 \quad (11)$$

$$RMSE = \sqrt{MSE} = \sqrt{\frac{1}{n}\sum_{i=1}^{n}\left(Y_{predicted} - Y_{actual}\right)^2} \quad (12)$$

$$R^2 = 1 - \frac{\sum_{i=1}^{n}\left(Y_{actual} - Y_{predicted}\right)^2}{\sum_{i=1}^{n}\left(Y_{actual} - Y_{mean\ value}\right)^2} \quad (13)$$

Tables 11 and 12 demonstrate how effective ML models can be to predict key performance parameters in gasification systems. These models achieved an R^2 value as high as 0.995, an RMSE value as low as 0.049, and an MSE as low as 0.0004.

Conclusion

ANN and GBM ML models for regression have been employed in numerous recent studies in order to make accurate predictions for gasification systems. The development of these ML models allows for better understanding and optimization of the gasification process. ML models allow for an alternative form of gasification system investigation than the traditional means of computational fluid dynamics modeling (CFD) or experimental iterations. There are many drawbacks to the traditional means of CFD modeling and experimental iterations to describe gasification systems. The former, CFD modeling, requires a high level of expertise, proper computing power, and can take a long time to create multiple modeling scenarios. The latter, experimental iterations, also requires a high level of expertise and can take a long time, but they additionally can have a high cost since there must be a large investment into proper materials and data analysis equipment. ML models mitigate the issues surrounding CFD modeling and experimental iterations of gasification systems by combining existing iterations of these methods and synthesizing them into an accurate and specific algorithm. The advancement of integration of ML models into gasification and other WtE technologies will serve to speed up the progress within these fields and assist in creating a more sustainable humanity.

IV. Scholarly Article 3: Application of Machine Learning to Predict the Performance of an EMIPG Reactor Using Data from Numerical Simulations

Abstract

Rising energy demand and waste generation are two forcing factors that encourage the development of waste-to-energy technologies. Plasma gasification is a type of waste-to-energy technology that has the potential to produce clean energy from municipal solid waste via a combustion process. Unlike traditional thermal waste treatment processes, plasma gasification provides an extreme condition within the reactor as temperatures can reach 30000K. Temperature conditions greater than 2000K allow for the complete combustion of municipal solid waste streams with minimal undesirable byproducts that can cause detriment to humans or the environment. One plasma gasification system that is emerging as a system with numerous benefits is microwave driven plasma gasification. Computational fluid dynamics software is renowned as one of the best ways to solve for the conditions within a plasma gasification reactor. When used in tandem with computational fluid dynamics software, machine learning models can accelerate high-fidelity fluid simulation, improve turbulence modeling, and enhance reduced-order-models. In this paper, a two-dimensional microwave driven plasma gasification reactor was developed in ANSYS® Fluent as a tool to create a total of 644 datasets for the training of six machine learning models that predict the proportion of area in the reactor that is greater than 2000K. The machine learning model with the best architecture to predict this proportion was a feed forward neural network that achieved a

mean absolute error of .011. This novel machine learning model will allow for the future optimization of experimental microwave plasma gasification systems as they allow the user to easily understand how much area within the reactor is available to contact the input waste at proper temperature conditions.

Short Summary

In this article a CFD solver is used for a numerical solution for the proportion of an experimental microwave-induced plasma gasification system reactor that is greater than 2000K. Following this, the numerical solution is iterated 644 times using different inputs and the results are recorded to inform a dataset. Finally, this dataset is used to inform a variety of machine learning models that can efficiently and accurately predict the experimental microwave-induced plasma gasification system reactor.

Introduction

The global human population is expected to increase from 7.8 billion to 10.9 billion people throughout the course of the 21st century[149]. The growth of the global populace yields greater consumption of resources and consequently drives an increasing municipal solid waste (MSW) stream[150]. Furthermore, rapid urbanization and economic development accompany this global population rise and concentrate MSW into confined, metropolitan areas[150]–[152]. Increased production and concentration of MSW in tandem with a rising composition complexity poses a glaring challenge for proper waste management[153]. Of the globally estimated 2.01 billion tonnes of MSW currently generated annually, approximately 33% is not managed properly[154].

Proper management of MSW is essential for preserving the welfare of society. MSW has the ability to affect air, water, and soil vectors that directly impact human health[155], [156]. The two predominant global means of managing MSW today are landfilling and incineration[154]. Unfortunately, both means of management and disposal can lead to inadvertent negative effects even when conducting proper management procedures. Landfills are some of the most significant contributors to greenhouse gas emissions within the waste industry and, in developing countries, landfill methane is rising in conjunction with population, consumption, and landfill expansion[150], [156], [157]. Waste incineration can cause a detriment to public health and the environment by creating sulfur oxides, nitrogen oxides, and particulate matter from the combustion process[158], [159]. Additionally, the increasing complexity of the composition of MSW causes incineration to yield a wide range of toxic and carcinogenic contaminants such as polyvinyl chloride, heavy metals, organic chemicals, and polychlorinated dibenzodioxins (dioxins) and polychlorinated dibenzofurans (furans) [41], [150], [160]–[163].

While known to be a global issue, smaller systems and environments also experience this waste management dilemma. The United States Department of Defense (USDOD) has recognized the need for process improvement within all of its operating centers [164]–[167]. Some factors driving the USDOD to pursue process improvement within waste management include: concerns about burn pit exposure causing adverse human health effects, limited energy resources and land availability in contingency operation environments, desire for point-of-source waste-to-energy (WtE) technologies, security concerns, and an overall transition towards more sustainable operations[8],

[168]–[171]. The National Aeronautic and Space Administration (NASA) as well as other private and government space agencies are concentrated on improving waste management processes. NASA along with other space agencies desire this process improvement to ensure efficient use of resources on interplanetary space travel, and future colonization of terrestrial bodies, planets, and space stations[9]. Facilities such as hospitals and airports also must focus efforts on improving their waste management practices. During the peak period, the COVID-19 pandemic created an estimated 5-fold increase in the demand for daily medical waste disposal which threatened the resilience of medical emergency systems in urban areas[172]. Many airports generate waste volumes at the same rate as a small city, and regional and national governments in their jurisdiction emphasize waste diversion from landfills [173]. This focus on waste diversion for numerous airports leads to their pursuit of sustainable waste management practices[173].

One emerging technology that may help to solve the multivariate waste management problem is microwave induced plasma gasification (MIPG). MIPG is a WtE technology that utilizes plasma gasification as a thermal waste treatment process. Plasma gasification is a process which subjects the MSW to a plasma flame within a reactor where temperatures can exceed 10000K[174]. Once exposed to the extreme temperatures within the reactor, the MSW is converted into two products: a syngas primarily composed of carbon monoxide and hydrogen, and an inert slag[17]. Both products can be utilized as resources, promoting a sustainable waste management model. The syngas output can be utilized for energy production, and the inert slag can be used as construction material[11],

[12]. The high temperature combustion is an enormous benefit for plasma gasification over other thermal waste treatment processes; this extreme temperature allows for hazardous and complex materials to be safely combusted without toxic emissions, dioxins, furans, or greenhouse gases[15], [24]. Most MIPG systems initialize the plasma flame by inserting a tungsten rod that acts as a temporary electrode arrangement[1], [43]. Once the plasma flame is initiated, the tungsten rod is removed and the plasma flame is maintained by a microwave and plasma forming gases, not an electrode arrangement. This increases system resilience as electrode utilization and corrosion can cause multiple operational problems and efficiency losses in traditional plasma gasification systems[17], [19]. Additionally, MIPG systems maintain lower voltage requirements than other plasma generator methods and have a lower setup cost as the reactor can operate under atmospheric conditions[17], [18]. One disadvantage of MIPG systems is that they are harder to scale than electrode based systems[16]. While MIPG systems can control the diameter and temperature of the plasma flame by increasing power to the system, the length of the reactor can only be controlled by adjusting the reactor size[26]. The diameter of the plasma flame is also constrained to the physical boundary of the reactor[175].

ANSYS® Fluent is a software that can be used to numerically model an MIPG system. Fluent is one of the most widely used computational fluid dynamics (CFD) modeling software packages in the world[176]. CFD is a tool originally used for aerospace applications; however, it has been adopted heavily in both the environmental and chemical engineering fields for its rich reactor modeling and solver ability[176]–

[179]. CFD modeling software uses a chosen solver method to solve partial differential equations for mass, momentum, and energy, as well as their theoretical and empirical correlations[49]. When these models are synthesized, the physical-chemical phenomena that take place within an MIPG reactor can be simulated and observed[60], [180]. By allowing the user to understand the multiphysics taking place within a MIPG reactor, expensive and tedious experimentation can be reduced and further optimized[49]. ANSYS® Fluent offers some benefits over other CFD modeling software, especially for first time users. ANSYS® Fluent contains an intuitive and robust graphical user interface (GUI) as well as a highly integrated support system[176]. Both the GUI and the support system aid the user to easily define solver settings for a model. A disadvantage of ANSYS® Fluent is that it is a closed source platform which can make it harder to modify the solver with user defined functions (UDF)[56], [62], [63]. For simulations that necessitate a high degree of personalization and where the user has a firm grasp of how to modify and customize open source software, OpenFOAM® is a great alternative CFD modeling software to use[64], [65], [176]. Machine learning (ML) algorithms can be informed by numerical models in order to build an accurate representations of the modeled system [181]. Additionally, the synthesis of ML and numerical models has the potential to accelerate high-fidelity fluid simulation, improve turbulence modeling, and enhance reduced-order-models[182]. ML algorithms identify patterns within a data set. These algorithms have been shown to be very functional and accurate with non-linear and highly variable time-dependent data commonly found in plasma gasification reactors[81], [83].

The purpose of this study is to compare ML algorithms that can predict the proportion of the area in the reactor that is above 2000K within a two-dimensional (2D) MIPG reactor given geometry and temperature inputs. 644 CFD models were simulated within ANSYS® Fluent to create a data set for the machine learning algorithms. The geometry and temperature inputs within the CFD models are based on experimental MIPG (EMIPG) reactors from a literature review of 13 different experiments. Thermal plasma is commonly defined as the temperature range from approximately 2000K to 30000K and by staying in this temperature range, full combustion of the waste can be achieved[183]. A magnetron is responsible for providing the microwave to the reactor, and the power supply to it has a direct effect on the temperature of the plasma flame within the EMIPG[184]. G.S. Ho et al. determined that fuel retention time, the amount of time that the MSW has in contact with the plasma flame, is the key parameter that affects plasma gasification performance[185]. Therefore, a ML algorithm that is able to predict the area within an EMIPG reactor that is experiencing a proper combustion temperature range can aid future research by allowing the user to optimize the system by determining a proper waste input rate. Furthermore, this parameter can now be estimated via a simplified algorithm instead of a time-consuming CFD software that requires the user to have a level of proficiency in order to simulate a model.

Data Selection

In this paper, a comprehensive literature review was conducted on previously studied EMIPG systems. The data from the literature review that is relevant to informing

the ANSYS® Fluent model in this study is shown in Table 13. In Table 13, the reactor diameters varied between 2.54cm-5.8cm and their lengths varied from 22.5cm-100cm. All EMIPG reactors in the review were quartz tubes and the diameter reported in Table 13 is the respective inner diameter of each reactor. Table 13 also shows that the power ranges from 1-6kW for each EMIPG system with a plasma temperature range from 973-6500K.

Table 13. Reactor descriptions for reviewed EMIPG systems

Source	Reactor Diameter	Reactor Length	Plasma Temperature
[29]	3cm	45cm	Up to 6500K
[30]	3cm	35cm	Up to 6500K
[19]	3cm	50cm	973-2173K
[186]	5.8cm	100cm	Above 3300K
[32]	5.8cm	100cm	Not Specified
[26]	3cm	Not Specified	2000-6500K
[33]	2.85cm	Not specified	Up to 5300K
[34]	2.54cm	22.5cm	5446-6100K
[184]	2.9cm	35cm	1063-1121K
[36]	3.3cm	Not Specified	Not Specified
[37]	2.9cm	Not Specified	1500K
[187]	3.1cm	Not Specified	4000-5000K
[188]	5cm	75cm	Up to 6000K

Modeling an EMIPG reactor in ANSYS FLUENT

In this study, ANSYS® Fluent is used to simulate the complex fluid dynamics and reactions that take place within an EMIPG reactor based on a series of assumptions that were found during a literature review of these reactors. Establishing a working CFD model of an EMIPG reactor will allow for an understanding of the thermodynamic interactions that take place within it, and thus solve for what proportion of the reactor's area contains a plasma flame with proper MSW combustion temperature conditions (>2000K). The CFD model used in this study contains Navier-Stokes equations to solve

for the fluid motion within the reactor, the energy equation to solve for the temperature distribution within the model, and the standard k-ε model to apply the effects of turbulence. This modeling approach is known as the Reynolds-averaged Navier-Stokes simulation (RANS) and is widely used for plasma reactor modeling as it helps to minimize computational effort[1]. The fluid motion is simplified within the reactor using the Eulerian-Eulerian approach that treats the gas and solid phases as a single continuum[1]. The transport equations are all solved using the finite volume method which discretizes the geometry of the reactor into two dimensional quadrilateral elements which allow the mathematical models to be solved within each element[1]. Once each element has been solved, the solutions can then be synthesized, allowing for the entire fluid motion within the reactor to be described[1].

Modeling Assumptions, Boundary Conditions, and Limitations

Due to the complicated nature of developing a solver for an EMIPG reactor, a set of assumptions must be made to develop a reliable solution. The first assumption is that the model is set to be pressure-based as the fluid inside of the reactor is assumed to have incompressible flow. Additionally, the fluid flow within the model is assumed to be fully turbulent. The next assumption is that the velocity formulation is set to absolute since the majority of flow within the EMIPG reactor is not assumed to be rotating. Additionally, the model is not a function of time as the scheme is set to steady state. Finally, the acceleration of gravity on the model is assumed as -9.81 m/s^2 along the Y-axis of the coordinate flame.

The boundary conditions for the model were informed by the literature review on EMIPG reactors. These boundary conditions include:

- A velocity inlet with fluid entering at $0.1\frac{m}{s}$ normal to the inlet. This a realistic rate for fluid within an EMIPG system to enter the reactor as a carrier/plasma forming gas[29], [30], [32]–[34], [36], [37], [175], [186], [187].
- A plasma flame sized to the relative diameter of the model.
- A 2-D model was used to describe the EMIPG reactor which has been shown to work in past literature, as well as aided in computational effort[56].
- A pressure outlet where the pressure is equal to atmospheric which is typical for an EMIPG system reactor[1].
- The sidewalls of the reactor set with thermal conditions of 300K due to the average temperature of input plasma forming gases. These carrier gases are typically tangentially injected into the reactor which allow them to insulate the sidewalls of the reactor by stabilizing and centering the plasma flame within it through a vortex effect[1].

The CFD modeling was conducted by using ANSYS® Fluent 2021 R1 Academic software. This software is a student version of ANSYS® Fluent.

Modeling Geometry and Meshing

The geometry for the EMIPG reactor model is designed in two-dimensions using ANSYS® DesignModeler software. The model consists of a symmetrical rectangle that has one edge on the top as the inlet and an edge on the bottom as an outlet. The two edges

perpendicular to the inlet and outlet are defined as the boundaries of the wall and the inner space of the rectangle is defined as the fluid. Both the inlet and outlet represent the diameter of a theoretical EMIPG reactor. The modeled reactor diameter and length will be varied according to possibilities found in the literature review. This two-dimensional model is describing the typical EMIPG system reactor as a quartz tube. A quartz tube is often used for these systems so that the interior of the reactor can be seen by image detection equipment that the experiment might use, as well as quartz is able to withstand a wide range of temperature conditions, and minimally contaminate the product syngas during the experimental process[1], [40].The three variables that encompass the geometry and temperature variations that will be modeled to inform the ML data set can be found in Table 14. The values that were selected for the modeling configurations of the three variables were done so to construct realistic modeling configurations of an EMIPG system within the minimum and maximum constraints of these values that was found in the literature review. Additionally, the values chosen were spread between the two constraints so that the resultant data set captures a wide distribution of varying systems within the constraints. It was important to capture as many configurations as possible and not focus on any specific parameter, since the computational effort in the modeling phase was high. One iteration of the modeled geometry of an EMIPG reactor along with its mesh configuration is shown in Figure 8.

Table 14. Geometry and temperature iterations modeled

Diameter (cm)	Lengths (cm)	Temperature Range (K)
2.5	100,90,80	900-6500 (In 100K Increments)
2.5	70,60,50,40,30	1000-6500 (in 500K increments), 2100
3	100,80,70,60,50,40, 30	1000-6500 (in 500K increments)
3.5	100,70,50,30	1000-6500 (in 500K increments), 2100
4	100,80,70,60,50,40,30	1000-6500 (in 500K increments)
4.5	100,70,50,30	1000-6500 (in 500K increments), 2100
5	100,80,70,60,50,40,30	1000-6500 (in 500K increments)
5.5	100,70,50,30	1000-6500 (in 500K increments), 2100

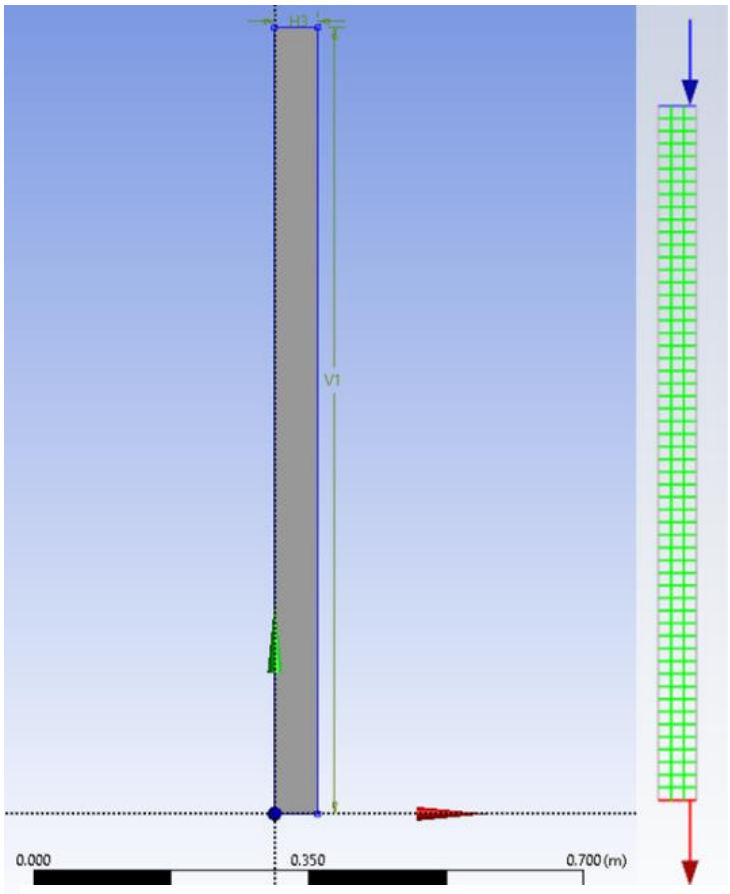

Figure 8. Numerical model geometry and meshing structure for 5.5cmx100cm EMIPG reactor

The meshing for the EMIPG reactor model was created using ANSYS® Mesh software. A meshing scheme was used to define the face of the mesh into quadrilateral elements. The default element size ratio was used so that despite the size of the geometry, the ANSYS® Fluent solver would be able to model each EMIPG reactor across a

common number of elements. Each mesh of the EMIPG reactor model was ensured to have an element quality minimum and maximum of at least 0.99.

Mathematical Modeling Equations

Multiple modeling equations were used within the CFD software to achieve the EMIPG reactor model. This model is a single-phase incompressible fluid model, with no other physical effects (i.e. combustion). Therefore, Navier-Stokes equations are solved for the fluid phase modeling using the assumed time-averaged steady-state conditions. The governing equations solved for the conservation of mass are shown by equation 14; for the conservation of momentum by equations 15.1, 15.2, 15.3; and for the conservation of energy by equation 16. The energy equation is used to capture and calculate the temperature distribution and changes within this computational model. The energy equation can be solved for temperature due to the assumption of an input velocity of 0.1 $\frac{m}{s}$ [189]. Low speed flows allow for the total energy per unit mass to be related directly to temperature, thus converting the energy equation into an equation for temperature[190]. All equations are defined for 2D axisymmetric geometries.

Mass: $\frac{\partial \rho}{\partial t} + \frac{\partial}{\partial x}(\rho v_x) + \frac{\partial}{\partial r}(\rho v_r) + \frac{\rho v_r}{r} = S_m$ (14)

$S_m$is the mass added to the continuous phase from the inlet, x is the axial coordinate, r is the radial coordinate, $v_x$is the axial velocity, and v_r is the radial velocity[190].

Momentum (axial): $\frac{\partial}{\partial t}(\rho v_x) + \frac{1}{r}\frac{\partial}{\partial x}(r\rho v_x v_x) + \frac{1}{r}\frac{\partial}{\partial r}(\rho v_r v_x) = -\frac{\partial p}{\partial x} + F_x$ (15.1)

Momentum (radial): $\frac{\partial}{\partial t}(\rho v_r) + \frac{1}{r}\frac{\partial}{\partial x}(r\rho v_x v_r) + \frac{1}{r}\frac{\partial}{\partial r}(r\rho v_r v_r) = -\frac{\partial p}{\partial r} + F_r$ (15.2)

where: $\nabla \cdot \vec{v} = \frac{\partial v_x}{\partial x} + \frac{\partial v_r}{\partial r} + \frac{v_r}{r}$ (15.3)

p is the static pressure and $\vec{F}$ is the respective gravitational body force and external body forces.

Energy: $\frac{\partial}{\partial t}(\rho e_t) + \nabla \cdot \left(\vec{V}(\rho e_t + p)\right) = \nabla \cdot \left(k\nabla T + \left(\bar{\bar{t}} \cdot \vec{V}\right)\right) + \dot{S_g}$ (16)

e_t is the total internal energy, $\dot{S_g}$is the generation source term of energy, k is the thermal conductivity of the fluid, T is the temperature, and $\bar{\bar{t}}$ is the shear stress tensor[189].

The standard k-ε model is used to solve for the fluid flow within the EMIPG reactor. The standard k-ε model is one of the most renowned models in solving for turbulent fluid flows and allows for the determination of both turbulent lapse scale and time scale by solving two different transport equations. Thus, the turbulent kinetic energy, k, and its rate of dissipation, ε, are obtained from the transport equations 17 and 18. Following this, the turbulent viscosity, μ_t, can be solved by combining k and ε shown in equation 19[191].

For k: $\frac{\partial}{\partial t}(\rho k) + \frac{\partial}{\partial x_i}(\rho k u_i) = \frac{\partial}{\partial x_j}\left[(\mu + \frac{\mu_t}{\sigma_k})\frac{\partial k}{\partial x_j}\right] + G_k + G_b - \rho\varepsilon - Y_M + S_k$ (17)

For ε: $\frac{\partial}{\partial t}(\rho \varepsilon) + \frac{\partial}{\partial x_i}(\rho \varepsilon u_i) = \frac{\partial}{\partial x_j}\left[(\mu + \frac{\mu_t}{\sigma_\varepsilon})\frac{\partial \varepsilon}{\partial x_j}\right] + C_{1e}\frac{\varepsilon}{k}(G_k + C_{3e}G_b) - C_{2e}\rho\frac{\varepsilon^2}{k} + S_\varepsilon$ (18)

G_k represents the generation of turbulence kinetic energy due to the mean velocity gradients, G_b is the generation of turbulence kinetic energy due to buoyancy, and

$Y_M$represents the contribution of the fluctuating dilation in compressible turbulence to the overall dissipation rate. σ_k and σ_ε are the turbulent Prandtl numbers for k and ε, respectively. S_k and S_ε are user-defined source terms[191].

Turbulent (eddy) viscosity: $\mu_t = \rho C_\mu \frac{k^2}{\varepsilon}$ (19)

The model constants $C_{1\varepsilon}$, $C_{2\varepsilon}$, C_μ, σ_k, σ_ε for equations 17, 18, and 19 have the following default values:

$C_{1\varepsilon} = 1.44, C_{2\varepsilon} = 1.92, C_\mu = 0.09, \sigma_k = 1.0, \sigma_\varepsilon = 1.3$

These default values have been determined from experiments with air and water for fundamental turbulent shear flows and have been found to work successfully for a wide range of wall-bounded and free shear flows[191].

Machine Learning Algorithms

This paper utilizes a total of 6 statistical ML models belonging to three different classes of regression algorithms. Linear regression, gradient boosting machines (GBM), and a deep neural network (DNN) are the three different classes of regression algorithms used in this paper. Regression algorithms were utilized due to the numerical nature of the data set. All ML models were created using Python 3. Additionally, the following libraries were utilized in order to construct the models and obtain statistical information describing them: Pandas, scikit-learn (with NumPY, SciPY, and matplotlib), and TensorFlow.

Linear Regression ML model

The simplest ML model utilized was a linear regression model. The type of linear regression used by the model was ordinary least squares linear regression. A linear model with coefficients shown in equation 20 is fit in order to reduce the residual sum of squares between the observed targets in the data set and the targets that were predicted by the linear approximation[192].

Linear Model: $\hat{y} = b_1 x + b_0$ (20)

Where b_1 and b_0 are chosen by minimizing the total sum of squares of the difference between the calculated and observed values of shown in equation 21.

$$\sum_{i=1}^{n}(y_i - \hat{y}_i)^2 = \sum_{i=1}^{n}(y_i - b_1 x_1 - b_0)^2 = \sum_{i=1}^{n}(\widehat{\in}_i)^2 = \min \quad (21)$$

Where $\hat{y}_i$ is the predicted value for the ith observation, y_i is the actual value for the ith observation, $\widehat{\in}_i$ is the residual for the ith observation, and n is the total number of observations.

Gradient Boosting ML Models

GBM is an ensemble or iterative learning model that uses decision trees for regression[144]. GBM uses a technique called gradient boosted trees in order to create a model in which every predictor corrects the predecessor's error; as this loss gradient is minimized, the model is fit[145][146].The GBM algorithm is expressed as an additive model of decision trees in equation 22.

Generalized GBM model: $f_m(x) = \sum_{m=1}^{M} T(x, \theta_m),\ T(x, \theta_m)$ (22)

Where θ_m is the parameter of the decision tree and M is the number of decision trees. The algorithm then uses a loss function in order to optimize the next learner parameter shown by equation 23[145].

GBM Loss Function: $\theta_{m+1} = \text{argmin} \sum_{t=1}^{N} L\left(y_t, F_m(x) + h(x, \theta_{m+1})\right)$ (23)

Four GBM algorithms were used with the modeled data set within this paper from three different libraries. These algorithms were a gradient boosting regressor (GBR), a histogram-based gradient boosting regressor (HGBR), XGBoost, and LightGBM. Multiple types of GBM algorithms were used in this paper in order to test different implementations of the GBM method; different libraries and GBM schemes tune different hyperparameters. Many differences in GBM models exist because some models, such as the HGBR and LightGBM, value model speed of fit, while others, such as XGBoost, value computational efficiency for better model performance.

Deep Neural Network ML Model

DNNs are a ML model that utilize artificial neural networks (ANNs). An ANN consists of an input and an output layer that contains a hidden layer in between. The hidden layer stores and evaluates the relationship and contribution of an input to an output, as well as stores information regarding an input's value and realizes the significance of combinations of inputs. These ANNs work similarly to the human brain in that they train themselves through experience and find patterns in order to determine an output[193]. ANNs are black-box models since they do not create analytical results, only

numerical ones[194]. The hidden layer, shown in equation 24, sums the input signals and uses an activation function to produce an output signal[195].

Hidden Layer Activation Function Equation: $y_j = f(\sum_{i=1} W_{ij} x_i + b_j)$ (24)

Where f is the activation function, W_{ij} is the weight of the link between the i_{th} input and the j_{th} neuron and $b_j$is the bias for the unit j[195]. The output data generated by the neurons are gathered into a layer and each output neuron, Q_k sums the weighted input signal and performs the activation function shown by equation 25[195], [196].

Output Neuron Activation Function: $Q_k = f_{activation} \sum_{j=1} V_{jk} y_j + b_k$ (25)

The weighted connection W_{ij} between neurons in contiguous layers is optimized through nonlinear algorithms[195]. The error within the difference of the predicted and target values is calculated, and then the optimization algorithm adjusts the weights accordingly. Following many iterations of this method, the weights can be determined[195]. DNNs use multiple hidden layers within their framework which is why they are named ‘deep’ as their model’s layers are multiple layers deep. A visualization of the DNN that was used in this paper is shown in Figure 9 and the details of the model are shown in Table 15.

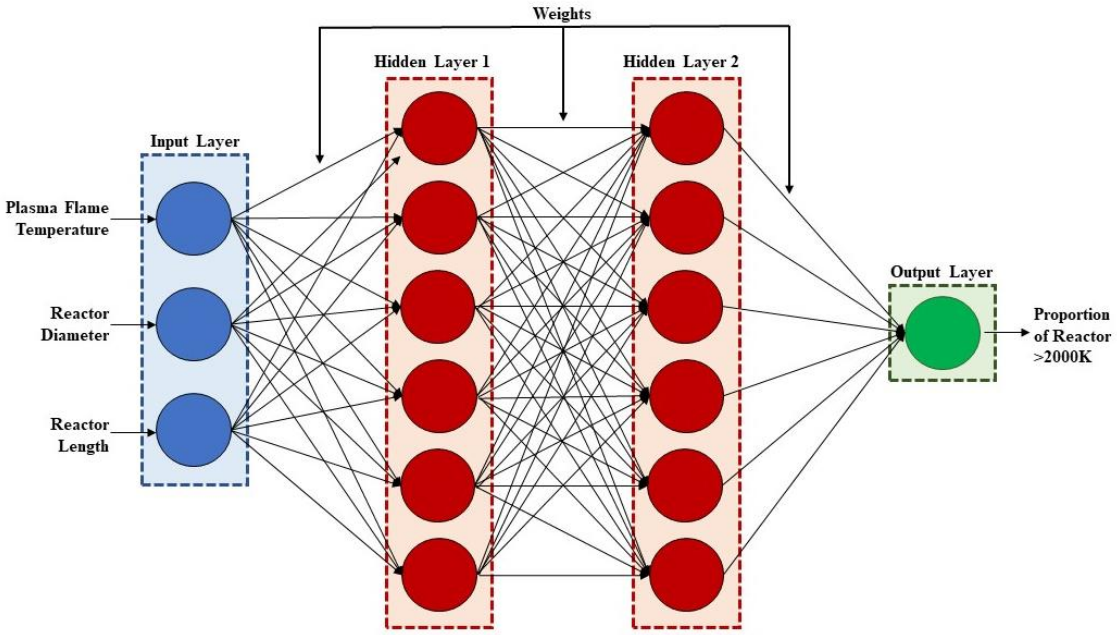

Figure 9. DNN model structure to predict the proportion of reactor >2000K in an EMIPG reactor

Table 15. DNN model characteristics

Detail	**Specification**
Network Type	Feed Forward Neural Network
Number of Layers	2
Hidden Layers	Non-linear, Dense layers with ReLU*
Output Layer	Linear Dense single-output layer
Optimizer	Adam
Learning Rate	0.001
Number of Neurons in the Input Layer	3 (Plasma Flame Temperature, Reactor Diameter, Reactor Length)
Total Parameters	1,006,008
Trainable Parameters	1,006,001
Non-trainable Parameters	7
Number of Neurons in Hidden Layer 1	1000
Number of Neurons in Hidden Layer 2	1000
Number of Neurons in the Output Layer	1 (Ratio of Reactor > 2000K)
Number of Epochs**	100

* rectified linear activation function[197], **A single iteration of the DNN using all training data

Performance of the ML Algorithms

Each value within a feed-forward neural network transitions between the input and output and proportionally between the hidden layers of the model[195]. Errors within the model are then determined and propagated back to the model where the weight and bias values of the previous layer in the model are changed for error reduction[195]. The error within all models used in this paper compare the difference between the estimated and actual values provided by the data set. In order to compare the prediction accuracy between the types of models used, the Mean Absolute Error (MAE) is calculated in Equation 26.

$$MAE = \frac{1}{n}\sum_{i=1}^{n}\left|Y_{predicted} - Y_{actual}\right| \qquad (26)$$

Where "n" is the number of instances that values transition between the input and output layer, "$Y_{predicted}$" is the generated value from the DNN model, and "Y_{actual}" is the target value. The MAE also known as median regression was used as a prediction of error in order to compare all of the ML models. The MAE was used to quantify how close the predictions are to the outcomes, and thus allowed for easy computational efficiency when it came to comparing the models. Additionally, the MAE was easier to fit across all the models in order to create a standard comparison. The DNN and GBM models used a loss function within the model themselves known as Mean Squared Error (MSE) in order to create a more accurate model. The MSE loss function is shown in Equation 27.

$$MSE = \frac{1}{n}\sum_{i=1}^{n}\left(Y_{predicted} - Y_{actual}\right)^2 \qquad (27)$$

CFD Model Description and Resultant Data Set

Each iteration of the CFD model of an EMIPG reactor solved for the temperature distribution in its interior, displayed in Figure 3. Figure 3 also shows the scaled residuals for all equations within the model following the solver iteration. The residuals were used to ensure that the solution by the solver was accurate. At the end of each solver iteration, the computer was set to sum the residuals over 1000 iterations. By ensuring that the residuals decayed to an extremely small value and leveled out the solution could be trusted as correct[198]. Most iterations finished rounding off and then leveled out at

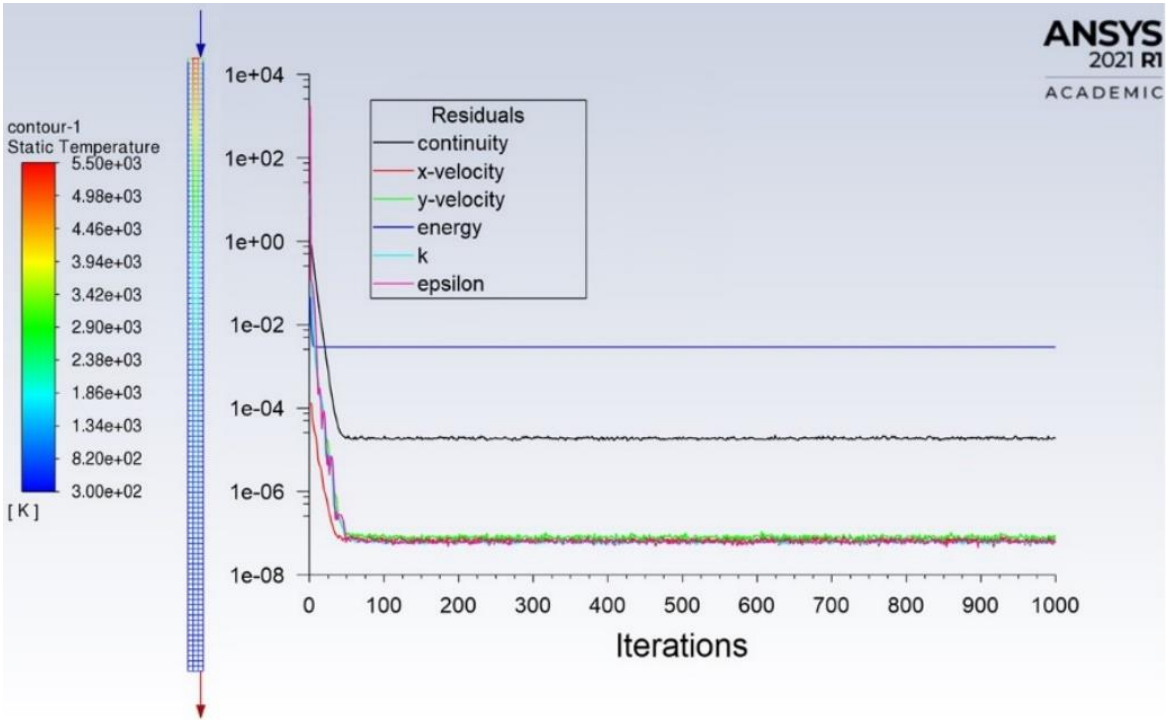

Figure 10. CFD solution for EMIPG reactor with contour diagram and scaled residuals

approximately 50 iterations. The input parameters for the model in Figure 10 was a 2.5cm diameter by 100cm reactor with a 5500K plasma flame.

Once ANSYS® Fluent was able to solve for an iteration of an EMIPG reactor, the histogram function was utilized to obtain the number of elements within the model that had a temperature greater than 2000K which is the temperature that allows for the benefits of plasma flame combustion and the number of elements that were below 2000K[183]. These values could then be used to create a ratio which shows the proportion of area within the EMIPG reactor model that was experiencing true plasma flame temperatures. A demonstration of the method to create the proportion for the EMIPG Reactor model in Figure 3 is shown in Table 16.

Table 16. Resultant proportion for one iteration of a CFD model

Reactor Input Parameters	**Ratio**	**Proportion of area within an EMIPG Reactor >2000K**
Temperature= 5500K Diameter= 2.5cm, Length= 100cm	$\frac{319\ elements\ above\ 2000K}{884\ elements\ below\ 2000K}$	$\approx .26517041$

All the proportions shown in Table 16 were gathered for each respective iteration and put into tabular form along with the input parameters for the model. The first few rows of the dataset, as well as the last row, are shown in Table 17. This dataset was used to inform the ML models. Table 18 is a table of statistics that describes the entirety of the dataset. Figure 11 shows a pair plot of the dataset that was used to visually inspect the dataset. The top row of Figure 11 indicates that the proportion of EMIPG reactor greater than 2000K is a function of all the other parameters. The following rows show the input parameters as functions of each other. The pair plot in Figure 11 shows that none of the data is a great linear predictor of the chaos within the dataset. This will allow for the ML

models to be able to demonstrate their ability to pick out the nuances that each specific input parameter creates in order to create the most accurate model.

Table 17. Demonstration of dataset used to inform the ML models

Model Number	Diameter	Length	Temperature	Proportion of EMIPG Reactor >2000K
1	2.5	100	2000	0.0024937656
2	2.5	100	2100	0.016625104
3	2.5	100	2200	0.029925187
4	2.5	100	2300	0.03990025
…	…	…	…	…
644	5.0	30	6500	0.8029567

Table 18. Table of statistics describing the dataset used to inform the ML models

Parameter	Count	Mean	Std.	Min.	25%	50%	75%	max
Diameter	644	3.571429	1.060909	2.5	2.5	3.5	4.5	5.5
Length	644	68.726708	24.518882	30	50	70	90	100
Temperature	644	3693.167702	1703.518424	900	2100	3500	5300	6500
Proportion	644	0.374670	0.315021	0	0.039271	0.303181	0.757032	0.848485

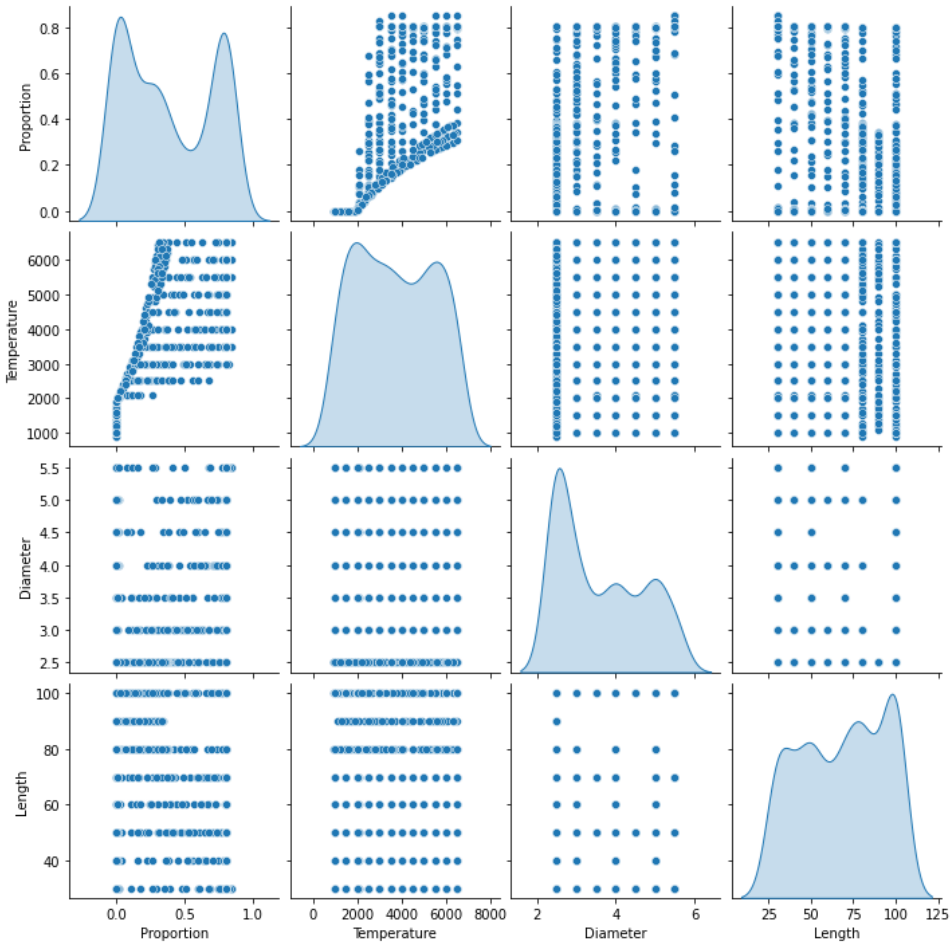

Figure 11. Pair plot of dataset from CFD model

Model Validation

The dataset, which represents the culmination of the CFD model solutions by the CFD modeling, must be demonstrably accurate so that the ML models can be accurate predictors of the plasma conditions within an EMIPG reactor. The initial correlations found within the dataset have been observed by previous experiments showing that the CFD model is reasonably accurate. Figure 12 shows a correlation matrix for the dataset displaying the Spearman's coefficient as a function of each input parameter within the entire dataset provided by the CFD model. As shown in Figure 12, the proportion of

plasma flame within the EMIPG reactor increases with diameter. Previous research conducted by Hong et al. demonstrated that the volume of plasma flame is a positive function of the flame's diameter[175]. Additionally, research by Arpia et al. and Li et al. displayed that the temperature distribution within the reactor is dependent on plasma flame temperature, supporting the positive correlation between these two parameters in Figure 12[199], [200].

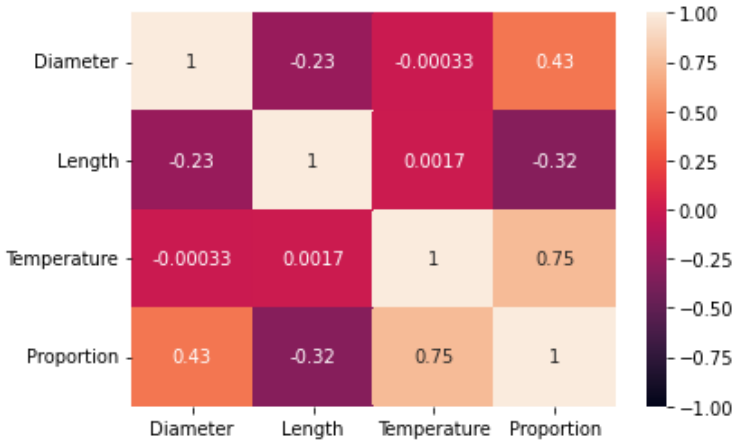

Figure 12. Correlation matrix of the dataset provided by CFD simulations

Linear Regression ML Models

A linear regression ML model was run for each individual input parameter against the output proportion (area >2000K within EMIPG reactor), as well as for the combination of all input parameters affecting the distribution. In order to increase the generalization capability of the linear regression model, the dataset was divided into two sets: 80% (515 models) of the dataset was used as a training set, and 20% (129 models) of the data was used as a validation dataset. A cross-validation of 10 random splits was used. The individual parameters were run using the linear regression ML model to show the effect they have on the temperature distribution. By observing this effect, the

parameters can be compared to the linear regression model that used all inputs in order to determine that the linear regression model benefits from the synthesis of the parameters. Figure 13 shows the trendline built by the predictions from the linear regression model for the diameter, temperature, and length parameters. The Spearman's correlation coefficients comparing diameter to proportion is 0.43, temperature to proportion is 0.75, and length to proportion is -0.32 which are also shown in Figure 12. The Spearman's correlation coefficients confirm what Figure 11 shows that there is a poor linear relationship between the input and output parameters. The strongest correlation, found with the input parameter temperature predicting the proportion can be reasonably assumed as the temperature has a direct effect on the intensity of the plasma flame.

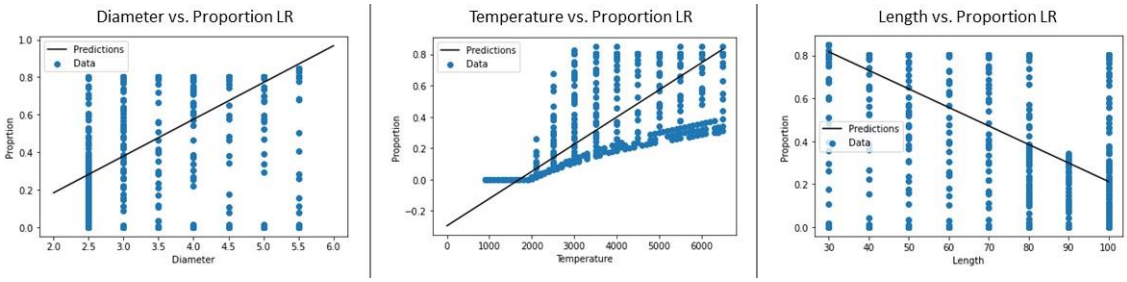

Figure 13. Input parameter vs. proportion with linear regression prediction and dataset

It can be seen in Figure 14 that the MAE was settled in approximately five epochs. The MAE value converged to a minimum value as the number of iterations increased; however, at around 5 epochs the MAE value continued steadily through 100. This trend shows that the weights and biases of the linear regression model were not changing significantly during the remaining iterations. The resulting MAE for the linear regression model with all parameters was 0.105. The error between the test and training

set for the proportion prediction is shown by Figure 14 for the 100 epochs. The result of the training dataset is shown by the loss function, and the val_loss shows the test set. Because the val_loss is the test set, the val_loss function is a good observation of how the model performs on unseen data.

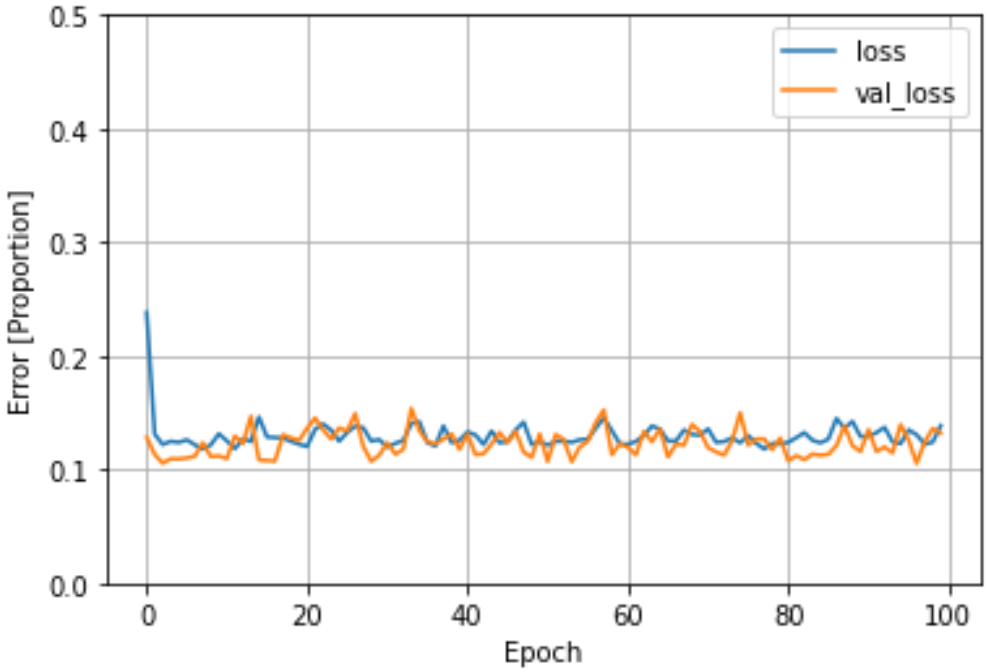

Figure 14. Linear regression model with all input parameters, 100 epochs

Gradient Boosting ML Models

For the GBM model, in order to increase the generalization capability, the dataset was divided into two sets: 80% (515 models) of the dataset was used as a training set, and 20% (129 models) of the data was used as a validation dataset. A cross-validation of 10 random splits was used. There is no specific amount that each dataset needs to be in order to yield results from the models. The training dataset is commonly chosen to be much larger than the test dataset in order to expose the model to more samples and variation

within the totality of the dataset[145]. The results from the CFD model were randomly assigned to either the training or validation dataset. The four GBM ML models proved to be excellent models for the given EMIPG reactor. All the GBM models were run with 10^5 n_estimators. The n_estimators with the GBM models represent the number of iterations, or trees, in each ensemble. The relationship between the n_estimators used in each model and the prediction accuracy of proportion of plasma flame within an EMIPG reactor are shown in Figure 15.

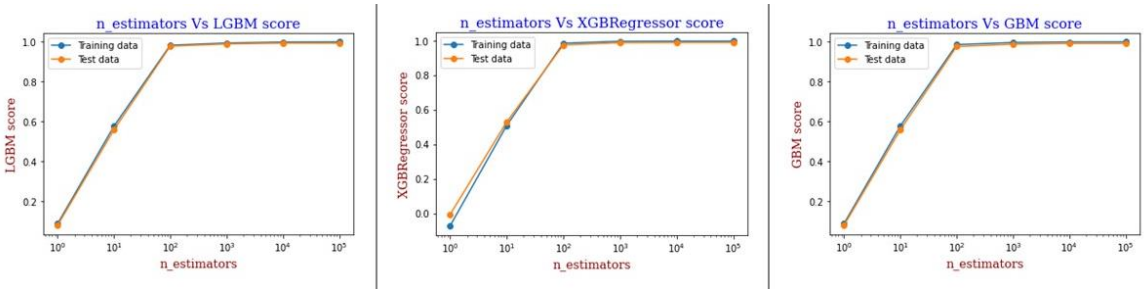

Figure 15. n_estimators vs GBM models: LightGBM (LGBM), XGBoost, GBR respectively from left to right

Figure 15 demonstrates that the prediction accuracy is settled at approximately 10^2 n_estimators and then continues steadily through 10^5. Since the HGBR model utilizes a bucketing technique with the data, this model was not compared with n_estimators. The best fitting model of the GBM method was the standard GBR which achieved an MAE of .015 with a standard deviation of .003. The rest of the GBM methods results are shown in Table 19. Shown in Table 19, the GBM methods accuracy, in order from best to worst fit is GBR, LightGBM, XGboost, and then HGBR. The HGBR was expected to be the least accurate model as it uses a histogram-based approach to achieve a quicker result, thus sacrificing the model's accuracy.

Table 19. Comparison of GBM model results with 10^5 n_estimators

GBM Method	MAE	Standard Deviation
GBR	.015	.003
LightGBM	.016	.003
XGboost	.019	.003
HGBR	.028	.005

DNN ML Models

Similar to the GBM model, the DNN model was divided into two datasets: 80% of the dataset was used as a training set, and 20% of the data was used as a validation dataset. A cross-validation of 10 random splits was used. The number of neurons in both hidden layers was tested between 10 and 10^5; 10^3 was used, as this provided the lowest MAE.

The DNN model was run for each input parameter in order to observe the relationship of the model with the three input parameters. In Figure 16, the predictions are shown against the dataset values for the diameter, temperature, and length. In Figure 17 the model's error is described through 100 passes of the training set (epochs) for the diameter, temperature, and length. The comparison between Figure 16 and Figure 13 demonstrates the advantage that DNNs have over linear regression ML models. The DNN model allows the predictions to follow a non-linear path that is able to accurately describe the chaotic results within the CFD model dataset. Figure 16 raised some concern as to whether a non-linear function might offer an optimal solution for a prediction of the dataset as each of the parameters seem to be following a non-linear function. Subsequent to this discovery, a polynomial model with cross-validation and least absolute shrinkage and selection operator (LASSO) regularization was used to develop a polynomial

prediction model for the given training and testing dataset with 5 random splits. This model showed that the non-linear regression ML model could only achieve a MAE of 0.036 which is not better than either the GBM ML models or the DNN model.

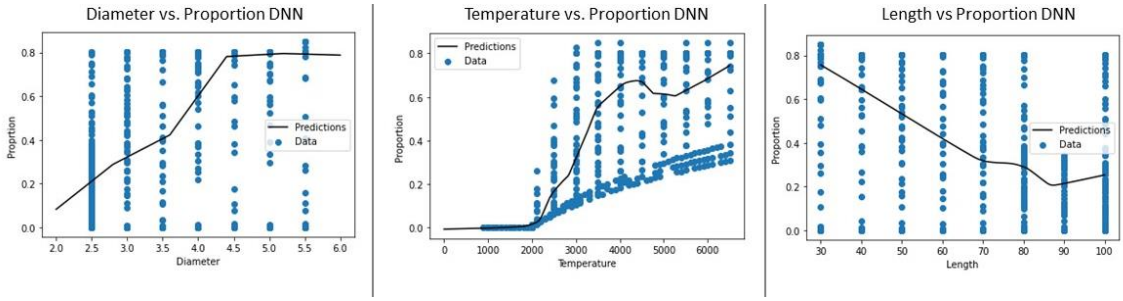

Figure 16. DNN model for diameter, temperature, and length predictions vs. dataset

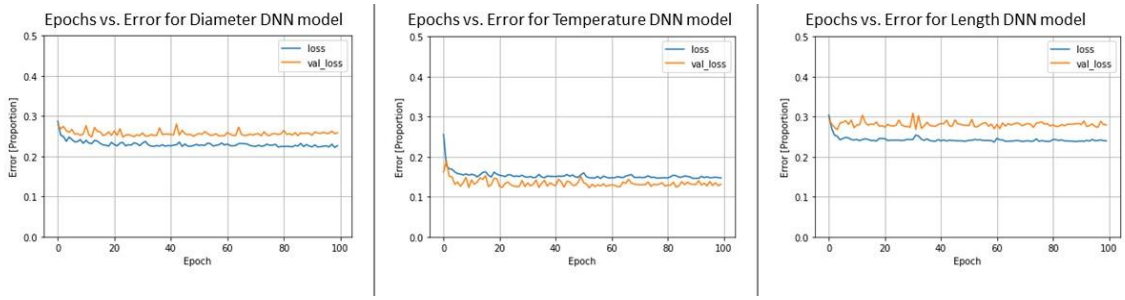

Figure 17. DNN model for diameter, temperature, and length error for 100 epochs

The same DNN model was run with all input parameters, and its error over 100 epochs is described in Figure 18. The epochs for the DNN model with all parameters have significantly less variation between the training and testing data when compared to when the DNN model was ran against the individual parameters. This shows that the weights and biases of the DNN model were not changing between iterations, indicating

that the model is a good fit. The DNN model seems to have minimized its error and leveled off at approximately 20 epochs.

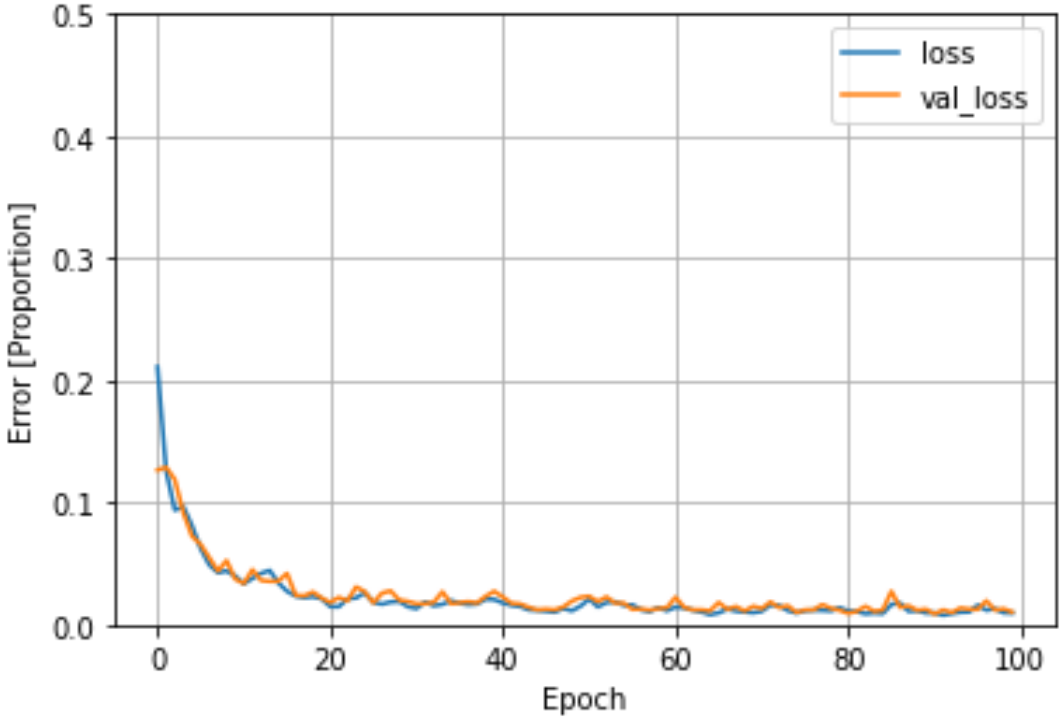

Figure 18. DNN model of all inputs over 100 epochs

The error within the DNN model of all inputs is shown further in Figure 19. In Figure 19, image “A” shows the predictions of the proportion by the DNN model against the true values of the proportion in the dataset. In Figure 19, image “B” shows a histogram of the prediction error for the proportion by the DNN model is shown. The histogram contains 20 bins. Both figures indicate that the DNN model is a good fit model for the prediction of the proportion of plasma flame within an EMIPG reactor.

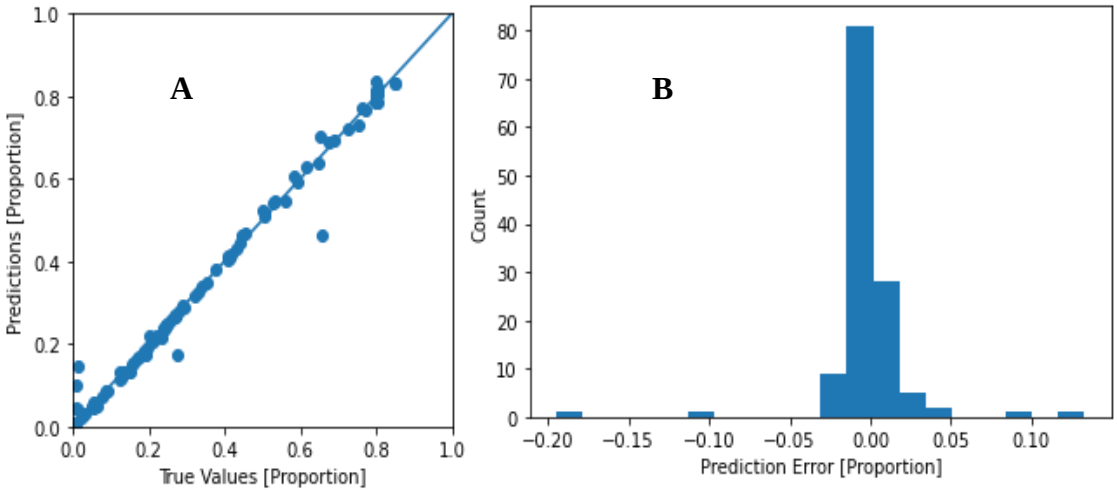

Figure 19. (A) True value vs. DNN prediction, (B) Histogram of DNN prediction error

The results of the MAE by the DNN models are shown in Table 20. It is clear that the synthesis of all input parameters informs the DNN model to make a much more accurate prediction. Only the DNN model that utilizes all input parameters is a satisfactory model. This demonstrates how DNN models are unique to each dataset. Even the most accurate individual DNN parameter was found to have a worse result than the linear regression model. The DNN relies on the uniqueness of the dataset including all input and output parameters in order to create a personalized prediction for it.

Table 20. Comparison of DNN model results

DNN Input Parameters	**MAE**
Temperature	.177
Diameter	.210
Length	.228
All Inputs	**.011**

Comparison of all ML Models

The results of all the ML models are shown in terms of the MAE of their predictions in Table 21. Table 21 shows that the most accurate model was the DNN ML model. This result was expected as these models are typically found to be the best type of ML model when it comes to describing the gasification process and predicting CFD solutions[195]. The GBM models, specifically the GBR model were able to achieve satisfactory predictions as long as the amount of n_estimators used was high enough in order to maximize the prediction accuracy. Finally, the linear regression model proved to be the least accurate ML model as forcing a linear prediction within the dataset severely limits its ability to find and skew towards the patterns and specificity within the seemingly tumultuous data.

Table 21. Comparison of all ML models with all input parameters

ML Model	MAE
Linear regression	.101
Non-linear regression	.036
GBR	.015
HGBR	.028
XGBoost	.019
LightGBM	.016
DNN	.011

Conclusion

The proportion of area greater than 2000K within an EMIPG reactor given variable inputs of diameter, length, and plasma flame temperature were examined with a CFD model developed by ANSYS® Fluent. To test the accuracy of this newly developed CFD model, the results of the dataset were then compared with the literature.

A dataset of 644 CFD modeling iterations containing three different input variables and one output variable was used to train six different ML models. The best ML model to predict the proportion of plasma flame within an EMIPG reactor was found to be the DNN followed closely by the GBR model. The linear regression model proved to add contrast and show the advantages that non-linear ML models have to accurately model the non-linear and highly variable time-dependent data commonly found in plasma gasification reactors.

In conclusion, ML models can be used to provide accurate prediction algorithms for EMIPG reactors based on CFD solutions. The ML models allow a user who has no experience with CFD software to understand parameters effecting EMIPG reactors. More importantly, calculations that take a long time using the numerical methods in CFD software can be quickly and accurately modeled with ML models. This study demonstrated that by using the input parameters of the diameter and length of an EMIPG reactor as well as the temperature of the initialized plasma flame, the proportion of the EMIPG reactor that has optimal combustion conditions can be estimated.

More broadly, this study aims to demonstrate that CFD solutions can be synthesized with ML algorithms that are able to provide accurate and fast solutions for specific problems. The availability and ease of use of a ML algorithm can allow someone who has no technical experience in the CFD field to yield equivalent results. This allows for more availability of data and, hopefully, faster process improvement when it comes to sustainable future technologies such as WtE. Additionally, the incorporation of ML with

numerical solutions has the potential to improve overall solution accuracy and better represent the phenomena in real-life WtE systems.

V. Conclusions and Recommendations

Conclusions of Research

This thesis focused on numerically modeling an experimental plasma gasification reactor to produce a dataset used by a machine learning model to properly estimate the proportion of the reactor that is >2000K. This was accomplished by addressing the following objectives:

1. Understand experimental plasma gasification systems and reactors and determine how they can be evaluated numerically.
2. Understand machine learning models and determine the appropriate machine learning models that can be used with gasification systems.
3. Apply the knowledge of experimental plasma gasification systems, numerical solutions, and machine learning models to synthesize these concepts and estimate the proportion of the reactor that is >2000K.

The first objective was accomplished by a thorough review of existing literature in Chapter 2 on experimental microwave-induced plasma gasification systems as well as existing computational fluid dynamics software that has been used to successfully model these systems. By reviewing this literature, the physical systems are understood as well as the governing equations that can be used to numerically solve for them. Additionally, this literature review also served to compare and contrast a variety of computational fluid dynamics software suites that have been used to model experimental microwave-induced plasma gasification systems.

The second objective was accomplished in Chapter 3 by a thorough review of existing literature on machine learning models for regression that have been used to successfully predict parameters of gasification systems. In this literature review, the accuracy of such machine learning models was tabularly compared. Through this comparison, an insight into successful machine learning model architecture for accurate system predictions was exposed.

The third objective was accomplished in Chapter 4 by synthesizing what has been learned in both Chapter 2 and 3 to create a successful numerical modeling solution for an experimental microwave-induced plasma gasification system. This solution was then iterated with varying parameters and a dataset was informed that was used by multiple machine learning algorithms. The results of these machine learning algorithms demonstrated that a machine learning algorithm can be applied to both efficiently and accurately predict the proportion of temperature that is greater than 2000K within an experimental microwave-induced plasma gasification reactor.

Contribution of Research

This thesis effort contributed to the development and advancement of the following areas:

1. Understanding of experimental microwave-induced plasma gasification systems.
2. Understanding of how to use computational fluid dynamics software to numerically model an experimental microwave-induced plasma gasification system reactor.

3. Understanding of how machine learning models can be used with gasification systems.
4. Identification of how to numerically model an experimental microwave-induced plasma gasification system to inform machine learning models that can make efficient and accurate predictions.

Significance of Research

The significance of this research is that this thesis not only will further optimize future experimental microwave-induced plasma gasification systems, but it also serves as a framework for showing how machine learning algorithms can be aided by computational fluid dynamics software in order to support waste-to-energy technologies.

Additionally, this thesis has produced the development of a peer-reviewed journal article that has expanded the greater academic and military community's understanding of the topics discussed within it.

Future Research recommendations

While the research performed advances the application of CFD and ML models with experimental microwave-induced plasma gasification systems, future research should explore:

1. Inclusion of a much larger dataset with various experimental and numerically modeled data. This thesis used the strict 644 datapoints that were created by the numerical model. Future research may benefit from utilizing larger datasets of existing experimental and numerically modeled solutions.

2. Creating an experimental system that can inform a dataset. While this thesis used only solutions from numerical modeling, perhaps more insight into machine learning application of these systems could be found by creating a representative small-scale system.
3. Other waste-to-energy systems. This thesis focused strictly on the application of models that simulated an experimental microwave-induced plasma gasification system. Other waste-to-energy systems can also benefit by machine learning application.
4. Focus on other predictive parameters. While this thesis focused primarily on the temperature proportion of the reactor, other parameters such as chemical composition of the resultant syngas or conversion efficiency could also be applied.

Exploration of any of these recommended research areas will aid in the future development and optimization of full-scale waste-to-energy technologies that can support both the USDoD and greater humanity to combat climate change.

Appendices

Appendix A: Numerically Modelling an EMIPG reactor using ANSYS Fluent

A.1: Open ANSYS Workbench

A.2: Set the units in ANSYS Workbench to Metric.

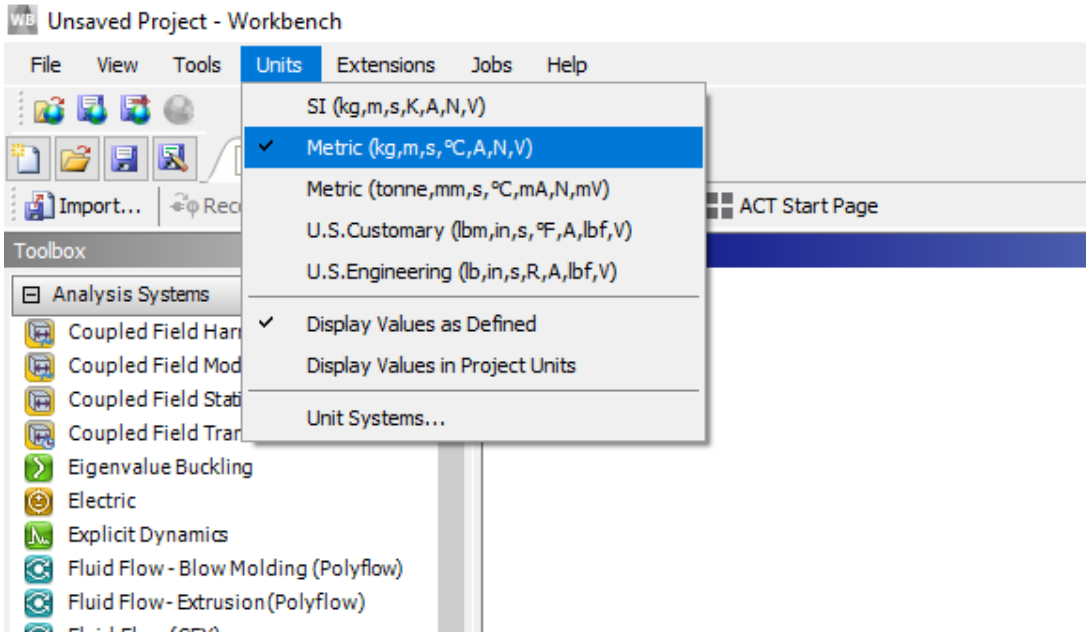

A.3: Drag and drop the geometry modeler onto the project schematic

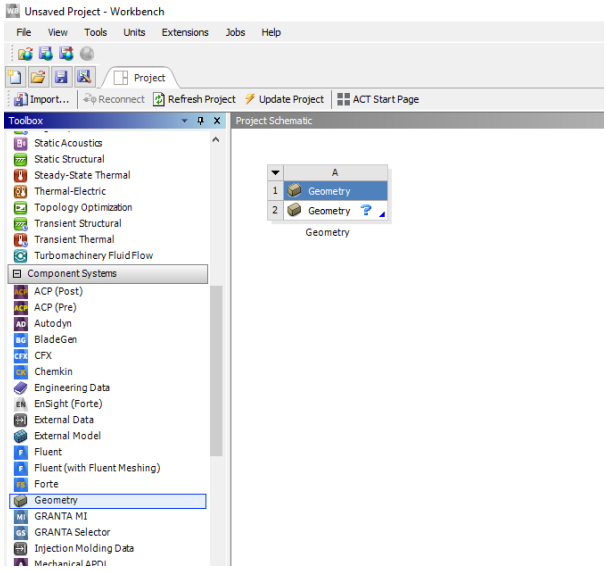

A.4: Right click and open new DesignModeler Geometry

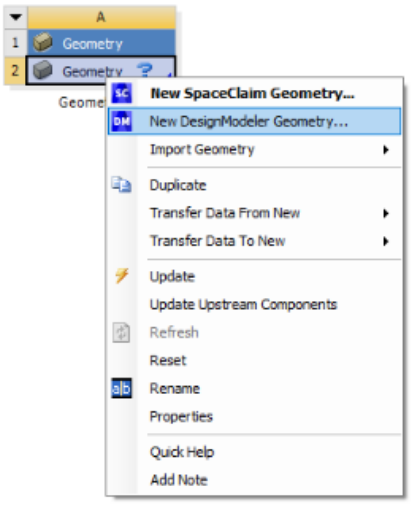

A.5 Under the Properties, ensure that 2D is selected

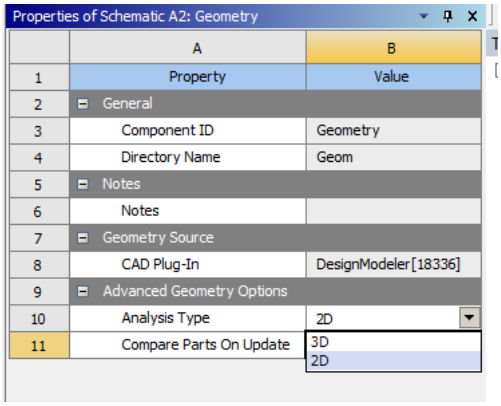

A.6 In the DesignModeler select the XYPlane and then select new sketch

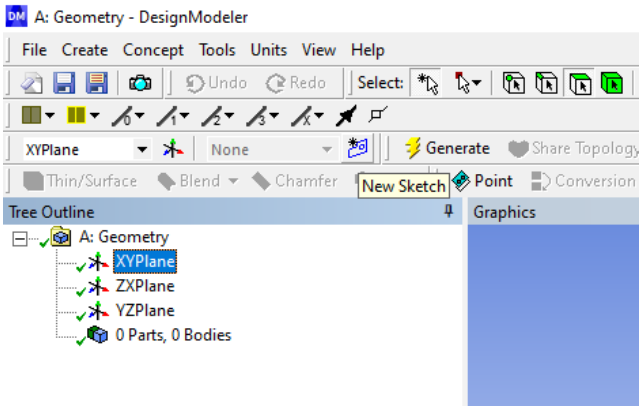

A.7 Select the Sketching tab and then select Rectangle.

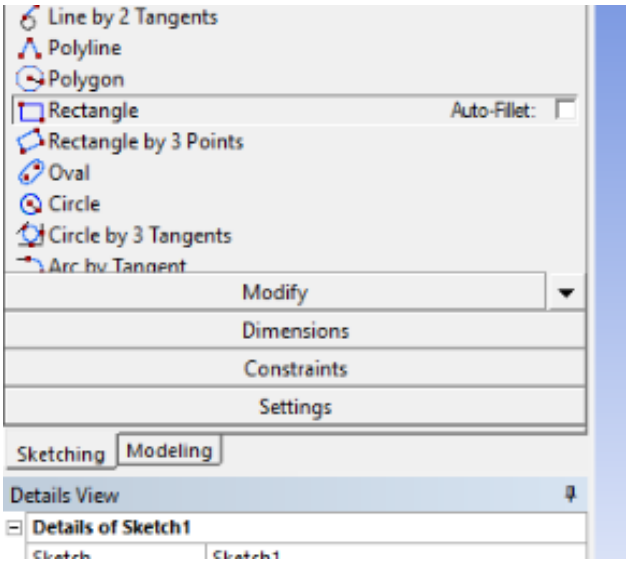

A.8 Draw the rectangle starting at the given origin

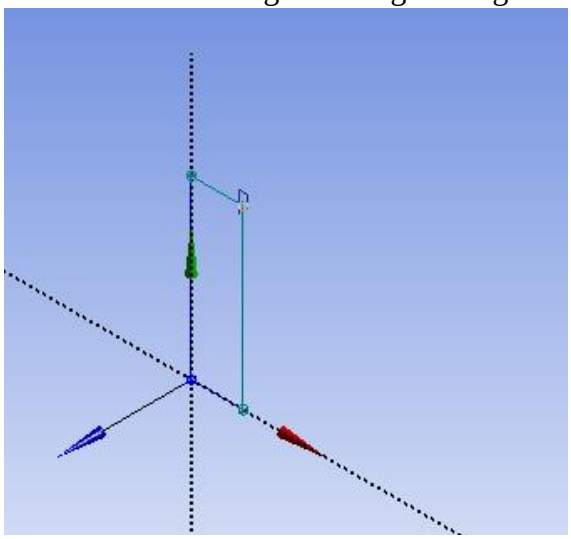

A.9 Select dimensions and then select horizontal.

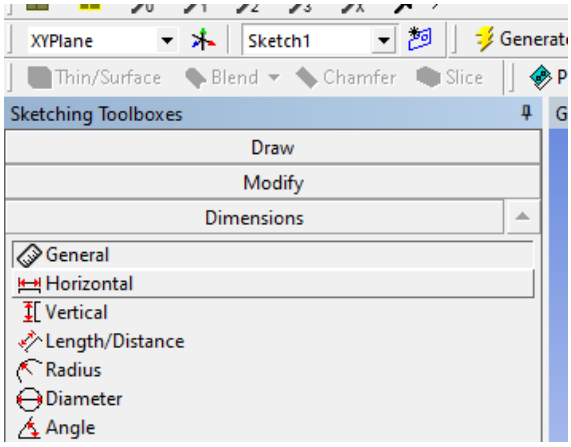

A.10 Draw the horizontal on the rectangle and edit dimensions under the detail view.

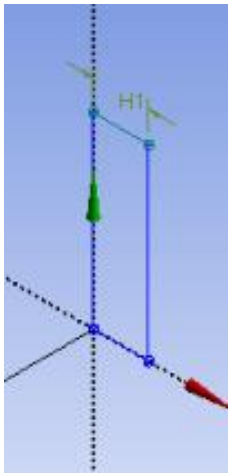

A.11 Repeat steps A.9 and A.11 in the vertical dimension.

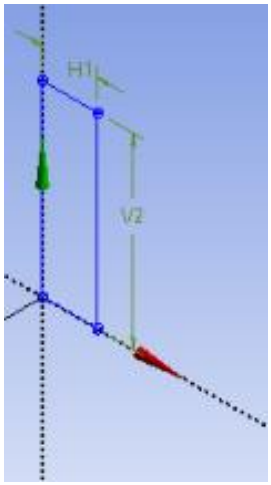

A.12 Select and label the top edge as inlet, the bottom edge as outlet, and the two side edges as walls. Ensure that the interior face is selected and label as fluid. Then generate the geometry.

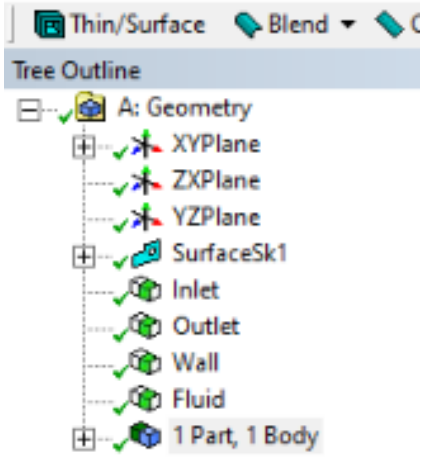

A. 13 Close DesignModeler click and drag ANSYS Mesh onto the project schematic and connect it to the geometry.

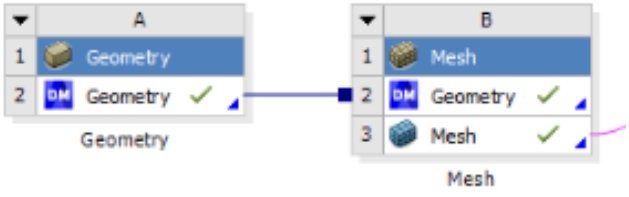

A.14 Open ANSYS Meshing click on Mesh and ensure that capture curvature and proximity are enabled. In the quality toolbox set the smoothing to high and then generate the mesh. Under the mesh control table select face meshing and make sure that quadrilaterals are set to default for the method.

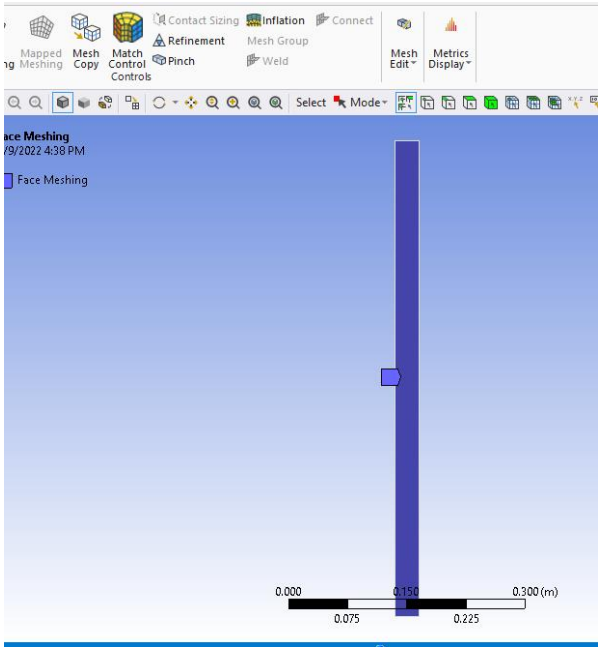

A.15 Close ANSYS Mesh after ensuring Mesh quality and drag ANSYS Fluent into the project schematic.

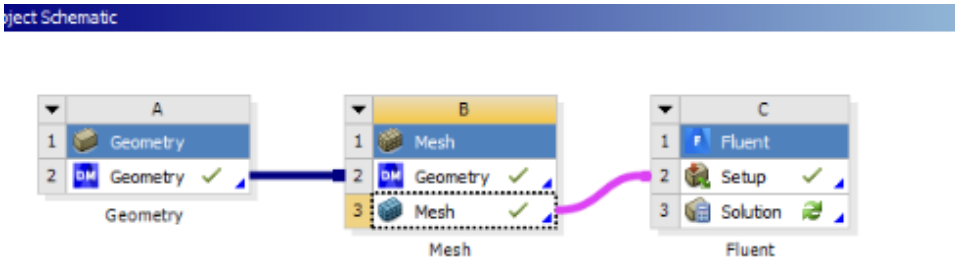

A.16 Define general boundary conditions of the problem.

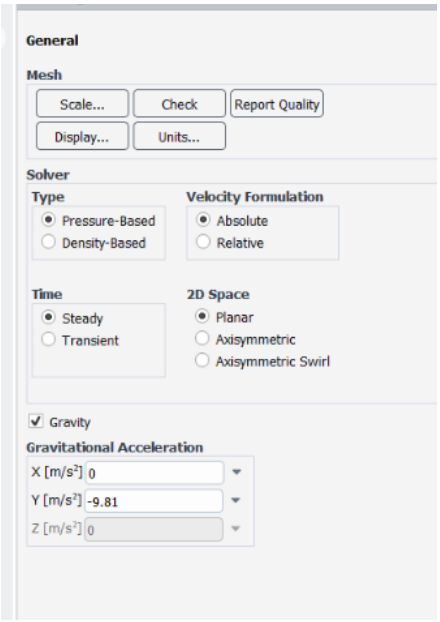

A.17 Turn on the energy equation.

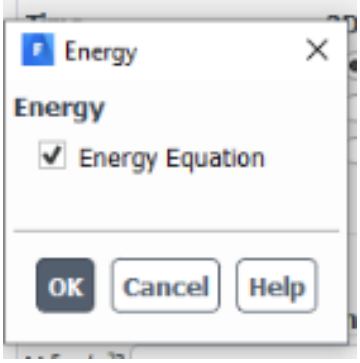

A.18 Set the viscous model with appropriate transport equations.

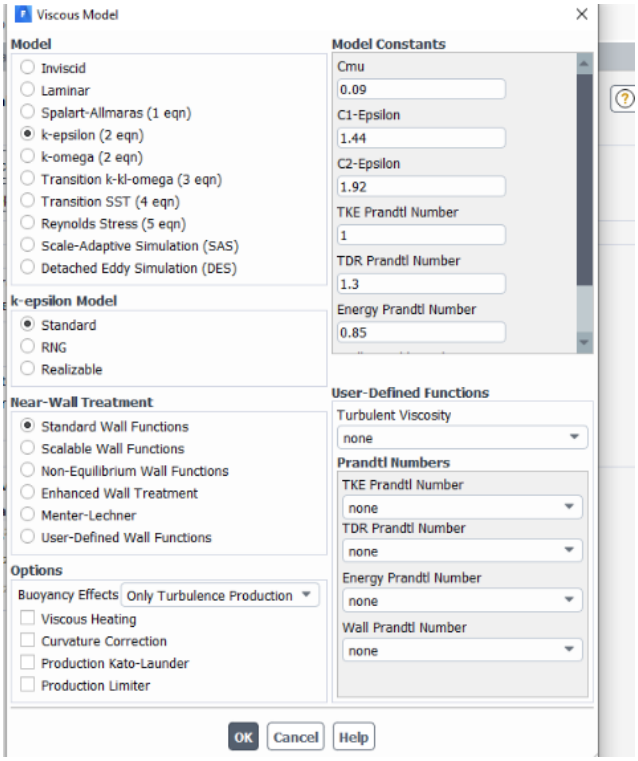

A.19 Set all boundary conditions as the correct type based on the model.

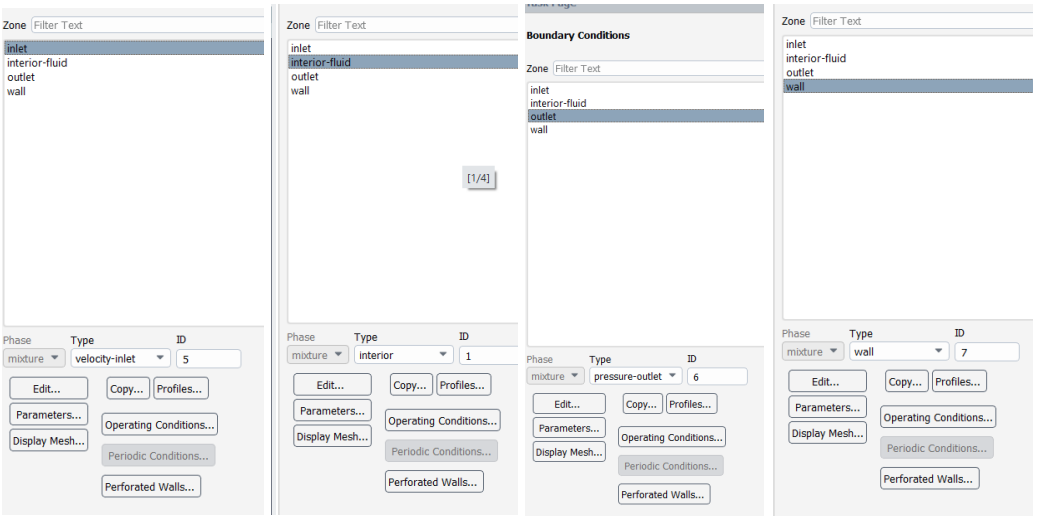

A.20 Set initialization process and initialize the solution.

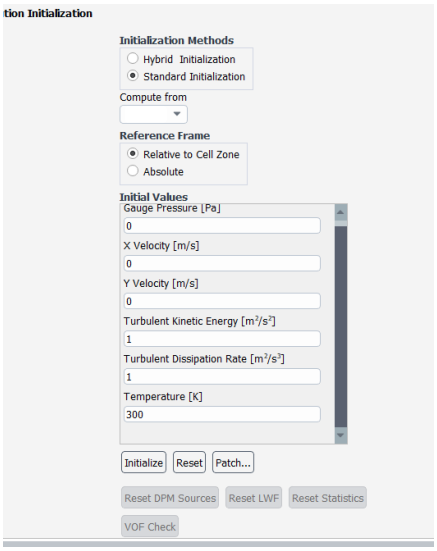

A.21 Set calculation process and run calculation.

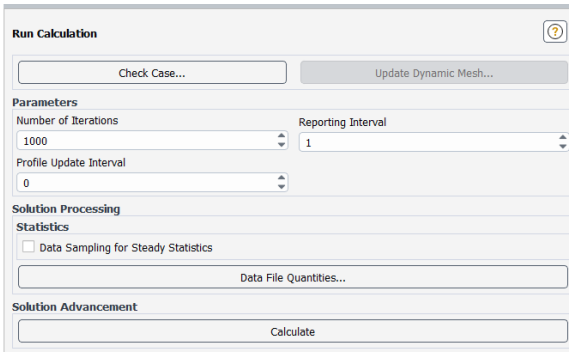

A. 22 Check residuals of solution

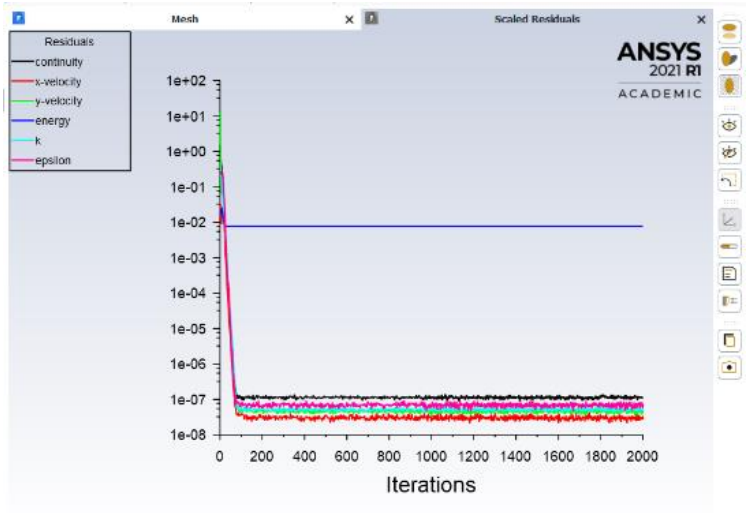

A.21 Once the residuals of the solution are satisfied, open histogram from plots. Select for the histogram to calculate and print results. Following this, configure the histogram to solve for the proper temperature zone.

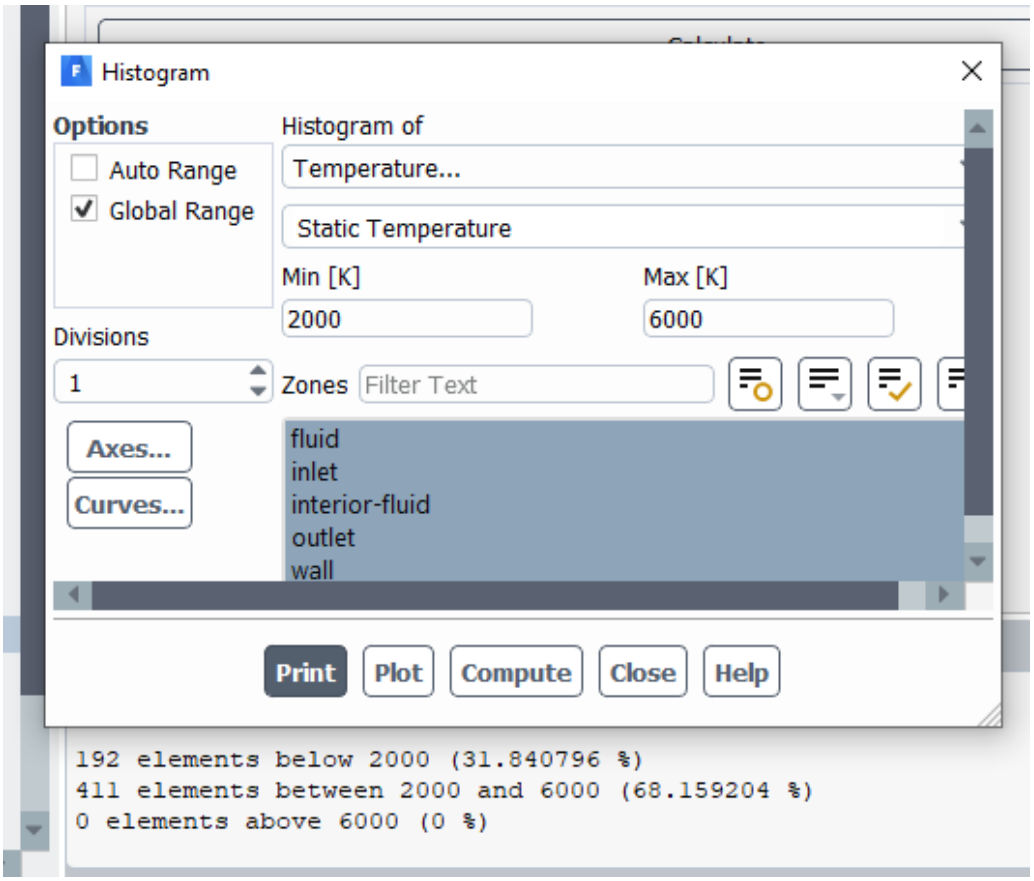

Appendix B: Code for the LR and DNN ML Models

```
normalizer = tf.keras.layers.Normalization(axis=-1)
```

+ Code

```
[ ] normalizer.adapt(np.array(train_features))
```

```
[ ] print(normalizer.mean.numpy())
```

```
[ ] first = np.array(train_features[:1])

    with np.printoptions(precision=2, suppress=True):
      print('First example:', first)
      print()
      print('Normalized:', normalizer(first).numpy())
```

```
[ ] #Linear Regression via one variable (temperature)
```

```
[ ] temperature = np. array(train_features['Temperature'])

    temperature_normalizer = layers.Normalization(input_shape=[1,], axis=None)
    temperature_normalizer.adapt(temperature)
```

```
[ ] temperature_model = tf.keras.Sequential([temperature_normalizer, layers.Dense(units=1)])

    temperature_model.summary()
```

```
[ ] temperature_model.predict(temperature[:10])
```

```
[ ] temperature_model.compile(optimizer=tf.optimizers.Adam(learning_rate=0.1), loss='mean_absolute_error')
```

```
[ ] %%time
    history = temperature_model.fit(train_features['Temperature'], train_labels, epochs=100, verbose=0, validation_split = 0.2)
```

```
[ ] hist = pd.DataFrame(history.history)
    hist['epoch'] = history.epoch
    hist.tail()
```

```
[ ] def plot_loss(history):
      plt.plot(history.history['loss'], label='loss')
      plt.plot(history.history['val_loss'], label='val_loss')
      plt.ylim([0,.5])
      plt.xlabel('Epoch')
      plt.ylabel('Error [Proportion]')
    test_features = test_dataset.copy()

    train_labels = train_features.pop('Proportion')
    test_labels = test_features.pop('Proportion')
```

```
[ ] train_dataset.describe().transpose()[['mean', 'std']]
```

```
  plt.plot(history.history['loss'], label='loss')
  plt.plot(history.history['val_loss'], label='val_loss')
  plt.ylim([0,.5])
  plt.xlabel('Epoch')
  plt.ylabel('Error [Proportion]')
  plt.legend()
  plt.grid(True)
```

```
[ ] plot_loss(history)
```

```
[ ] test_results = {}

    test_results['temperature_model'] = temperature_model.evaluate(
        test_features['Temperature'],
        test_labels, verbose=0)
```

```
[ ] x = tf.linspace(0, 6500, 6501)
    y=temperature_model.predict(x)
```

```
[ ] def plot_temperature(x, y):
      plt.scatter(train_features['Temperature'], train_labels, label='Data')
      plt.plot(x, y, color='k', label='Predictions')
      plt.xlabel('Temperature')
      plt.ylabel('Proportion')
      plt.legend()
```

```
[ ] plot_temperature(x,y)
```

```
[ ] #Linear Regression via one variable (Diameter)
```

```
[ ] diameter = np.array(train_features['Diameter'])

    Diameter_normalizer = layers.Normalization(input_shape=[1,], axis=None)
    Diameter_normalizer.adapt(diameter)
```

```
    diameter_model = tf.keras.Sequential([Diameter_normalizer, layers.Dense(units=1)])

    diameter_model.summary()
```

```
    diameter_model.predict(diameter[:10])
```

```
[ ] diameter_model.compile(optimizer=tf.optimizers.Adam(learning_rate=0.1), loss='mean_absolute_error')
```

```
[ ] %%time
    history = diameter_model.fit(train_features['Diameter'], train_labels, epochs=100, verbose=0, validation_split = 0.2)
```

```
[ ] hist = pd.DataFrame(history.history)
    hist['epoch'] = history.epoch
    hist.tail()
```

```
[ ] def plot_loss(history):
      plt.plot(history.history['loss'], label='loss')
      plt.plot(history.history['val_loss'], label='val_loss')
      plt.ylim([0,.5])
      plt.xlabel('Epoch')
      plt.ylabel('Error [Proportion]')
      plt.legend()
      plt.grid(True)
```

```
[ ] plot_loss(history)
```

```
[ ] test_results = {}

    test_results['diameter_model'] = diameter_model.evaluate(
        test_features['Diameter'],
        test_labels, verbose=0)
```

```
[ ] x = tf.linspace(2, 6, 6)
    y=diameter_model.predict(x)
```

```
[ ] def plot_diameter(x, y):
      plt.scatter(train_features['Diameter'], train_labels, label='Data')
      plt.plot(x, y, color='k', label='Predictions')
      plt.xlabel('Diameter')
      plt.ylabel('Proprtion')
      plt.legend()
```

```
[ ] plot_diameter(x,y)
```

```
[ ] #Linear Regression via one variable (Length)
```

```
[ ] length = np. array(train_features['Length'])

    length_normalizer = layers.Normalization(input_shape=[1,], axis=None)
    length_normalizer.adapt(length)
```

```
[ ] length_model = tf.keras.Sequential([length_normalizer, layers.Dense(units=1)])

    length_model.summary()
```

```
[ ] length_model.predict(length[:10])
```

```
[ ] length_model.compile(optimizer=tf.optimizers.Adam(learning_rate=0.1), loss='mean_absolute_error')
```

```
[ ] %%time
    history = length_model.fit(train_features['Length'], train_labels, epochs=100, verbose=0, validation_split = 0.2)
```

```
[ ] hist = pd.DataFrame(history.history)
    hist['epoch'] = history.epoch
    hist.tail()
```

```
[ ] def plot_loss(history):
      plt.plot(history.history['loss'], label='loss')
      plt.plot(history.history['val_loss'], label='val_loss')
      plt.ylim([0,.5])
      plt.xlabel('Epoch')
      plt.ylabel('Error [Proportion]')
      plt.legend()
      plt.grid(True)
```

```
[ ] plot_loss(history)
```

```
    test_results = {}

    test_results['length_model'] = length_model.evaluate(
        test_features['Length'],
        test_labels, verbose=0)
```

```
[ ] x = tf.linspace(30, 100, 100)
    y=length_model.predict(x)
```

```
[ ] def plot_length(x, y):
      plt.scatter(train_features['Length'], train_labels, label='Data')
      plt.plot(x, y, color='k', label='Predictions')
      plt.xlabel('Length')
      plt.ylabel('Proportion')
      plt.legend()
```

```
[ ] plot_length(x,y)

[ ] #Linear Regression with All Inputs

[ ] linear_model = tf.keras.Sequential([normalizer, layers.Dense(units=1)])

[ ] linear_model.predict(train_features[:10])

[ ] linear_model.layers[1].kernel

[ ] linear_model.compile(optimizer=tf.optimizers.Adam(learning_rate=0.1), loss='mean_absolute_error')

[ ] %%time
    history = linear_model.fit(train_features, train_labels, epochs=100, verbose=0, validation_split=0.2)

[ ] plot_loss(history)

[ ] test_results = {}
    test_results['linear_model']= linear_model.evaluate(test_features, test_labels, verbose=0)

[ ] #Regression with a single-input deep neural network (Temperature)

[ ] def build_and_compile_model(norm):
      model = keras.Sequential([norm, layers.Dense(1000, activation='relu'),layers.Dense(1000, activation='relu'),layers.Dense(1)])

      model.compile(loss='mean_absolute_error', optimizer= tf.keras.optimizers.Adam(0.001))

      return model

[ ] dnn_temperature_model = build_and_compile_model(temperature_normalizer)

[ ] dnn_temperature_model.summary()

    %%time
    history = dnn_temperature_model.fit(
        train_features['Temperature'],
        train_labels,
        validation_split=0.2,
        verbose=0, epochs=100
    )
```

```
[ ] plot_loss(history)
```

```
[ ] x = tf.linspace(0,6500,6501)
    y = dnn_temperature_model.predict(x)
```

```
[ ] plot_temperature(x, y)
```

```
[ ] test_results['dnn_temperature_model'] = dnn_temperature_model.evaluate(
        test_features['Temperature'], test_labels, verbose=0
    )
```

```
[ ] #Regression with a single-input deep neural network (Diameter)
```

```
[ ] def build_and_compile_model(norm):
      model = keras.Sequential([norm, layers.Dense(1000, activation='relu'),layers.Dense(1000, activation='relu'),layers.Dense(1)])

      model.compile(loss='mean_absolute_error', optimizer= tf.keras.optimizers.Adam(0.001))

      return model
```

```
[ ] dnn_diameter_model = build_and_compile_model(Diameter_normalizer)
```

```
[ ] dnn_diameter_model.summary()
```

```
[ ] %%time
    history = dnn_diameter_model.fit(
        train_features['Diameter'],
        train_labels,
        validation_split=0.2,
        verbose=0, epochs=100
    )
```

```
[ ] plot_loss(history)
```

```
[ ] x = tf.linspace(2,6,6)
    y = dnn_diameter_model.predict(x)
```

```
[ ] plot_diameter(x, y)
```

```
[ ] test_results['dnn_diameter_model'] = dnn_diameter_model.evaluate(
        test_features['Diameter'], test_labels, verbose=0
    )
```

```
#Regression with a single-input deep neural network (Length)
```

```
def build_and_compile_model(norm):
  model = keras.Sequential([norm, layers.Dense(1000, activation='relu'),layers.Dense(1000, activation='relu'),layers.Dense(1)])

  model.compile(loss='mean_absolute_error', optimizer= tf.keras.optimizers.Adam(0.001))

  return model
```

```
dnn_length_model = build_and_compile_model(length_normalizer)
```

```
dnn_length_model.summary()
```

```
%%time
history = dnn_length_model.fit(
    train_features['Length'],
    train_labels,
    validation_split=0.2,
    verbose=0, epochs=100
)
```

```
plot_loss(history)
```

```
x = tf.linspace(30,100,100)
y = dnn_length_model.predict(x)
```

```
plot_length(x, y)
```

```
test_results['dnn_length_model'] = dnn_length_model.evaluate(
    test_features['Length'], test_labels, verbose=0
)
```

```
#Regression using a DNN and All Inputs
```

```
dnn_model = build_and_compile_model(normalizer)
dnn_model.summary()
```

```
%%time
history = dnn_model.fit(
    train_features,
    train_labels,
    validation_split=0.2,
```

```
        validation_split=0.2,
        verbose=0, epochs=100
    )
```

```
[ ] plot_loss(history)
```

```
[ ] test_results['dnn_model'] = dnn_model.evaluate(test_features, test_labels, verbose=0)
```

```
[ ] pd.DataFrame(test_results, index=['Mean absolute error [Proportion]']).T
```

```
[ ] test_predictions= dnn_model.predict(test_features).flatten()

    a = plt.axes(aspect='equal')
    plt.scatter(test_labels, test_predictions)
    plt.xlabel('True Values [Proportion]')
    plt.ylabel('Predictions [Proportion]')
    lims = [0, 1]
    plt.xlim(lims)
    plt.ylim(lims)
    _= plt.plot(lims, lims)
```

```
[ ] error = test_predictions - test_labels
    plt.hist(error, bins=20)
    plt.xlabel('Prediction Error [Proportion]')
    _ = plt.ylabel('Count')
```

```
[ ] dnn_model.save('dnn_model')
```

```
[ ] reloaded = tf.keras.models.load_model('dnn_model')

    test_results['reloaded'] = reloaded.evaluate(
        test_features, test_labels, verbose=0)
```

```
[ ] pd.DataFrame(test_results, index=['Mean absolute error [Ratio]']).T
```

Appendix C: Code for GBM ML Models

```
[ ] import pandas as pd
    import numpy as np
    from sklearn import linear_model
    from sklearn.model_selection import train_test_split
    import matplotlib.pyplot as plt
    from sklearn import preprocessing
    from scipy import stats
```

```
    from google.colab import files
    uploaded= files.upload()
```

```
    df= pd.read_excel('Compilation.xlsx')
```

```
    df.head()
```

```
[ ] df.tail()
```

```
[ ] df1=df[['Diameter', 'Length', 'Temperature']]
    df2=df['Proportion']
```

```
[ ] print(df1.max())
```

```
[ ] X= preprocessing.StandardScaler().fit_transform(df1)
    Y= df2
```

```
[ ] X_train, X_test, Y_train, Y_test = train_test_split(X, Y, test_size=0.2)
```

```
[ ] from sklearn.ensemble import GradientBoostingRegressor
```

```
[ ] GBM = GradientBoostingRegressor(n_estimators=100000, learning_rate=0.05, max_features=3, max_depth=3, random_state=0)
    GBM.fit(X_train, Y_train)
```

```
[ ] from sklearn.metrics import mean_absolute_error
    from sklearn.model_selection import cross_val_score
    from sklearn.model_selection import RepeatedKFold
    from sklearn.metrics import r2_score
    from numpy import mean
    from numpy import std
    cv = RepeatedKFold(n_splits=10, n_repeats=3, random_state=1)
```

```
cv = RepeatedKFold(n_splits=10, n_repeats=3, random_state=1)
n_scores = cross_val_score(GBM, X_train, Y_train, scoring='neg_mean_absolute_error', cv=cv, n_jobs=-1, error_score='raise')
print('MAE: %.3f (%.3f)' % (mean(n_scores), std(n_scores)))
```

```
[ ] from sklearn.experimental import enable_hist_gradient_boosting
    from sklearn.ensemble import HistGradientBoostingRegressor
```

```
[ ]   HGBM = HistGradientBoostingRegressor(learning_rate=0.05)
      HGBM.fit(X_train, Y_train)
```

```
[ ] from sklearn.metrics import mean_absolute_error
    from sklearn.model_selection import cross_val_score
    from sklearn.model_selection import RepeatedKFold
    from numpy import mean
    from numpy import std
    cv = RepeatedKFold(n_splits=10, n_repeats=3, random_state=1)
    n_scores = cross_val_score(HGBM, X_train, Y_train, scoring='neg_mean_absolute_error', cv=cv, n_jobs=-1, error_score='raise')
    print('MAE: %.3f (%.3f)' % (mean(n_scores), std(n_scores)))
```

```
MAE: -0.028 (0.005)
```

```
[ ] from xgboost import XGBRegressor
```

```
[ ] XGB = XGBRegressor(n_estimators=100000, learning_rate=0.05, max_features=3, max_depth=3, random_state=0)
    XGB.fit(X_train, Y_train)
```

```
[ ] from sklearn.metrics import mean_absolute_error
    from sklearn.model_selection import cross_val_score
    from sklearn.model_selection import RepeatedKFold
    from sklearn.metrics import r2_score
    from numpy import mean
    cv = RepeatedKFold(n_splits=10, n_repeats=3, random_state=1)
    n_scores = cross_val_score(XGB, X_train, Y_train, scoring='neg_mean_absolute_error', cv=cv, n_jobs=-1, error_score='raise')
    print('MAE: %.3f (%.3f)' % (mean(n_scores), std(n_scores)))
```

```
[ ] from lightgbm import LGBMRegressor
```

```
[ ] LGBM = LGBMRegressor(n_estimators=10000, learning_rate=0.05, max_features=3, max_depth=3, random_state=0)
    LGBM.fit(X_train, Y_train)
```

```
from sklearn.metrics import mean_absolute_error
from sklearn.model_selection import cross_val_score
from sklearn.model_selection import RepeatedKFold
from sklearn.metrics import r2_score
from numpy import mean
cv = RepeatedKFold(n_splits=10, n_repeats=3, random_state=1)
n_scores = cross_val_score(LGBM, X_train, Y_train, scoring='neg_mean_absolute_error', cv=cv, n_jobs=-1, error_score='raise')
print('MAE: %.3f (%.3f)' % (mean(n_scores), std(n_scores)))
```

References

[1] O. Sedej and E. Mbonimpa, “CFD Modeling of a Lab-Scale Microwave Plasma Reactor for Waste-to-Energy Applications: A Review,” *Gases 2021, Vol. 1, Pages 133-147*, vol. 1, no. 3, pp. 133–147, Jul. 2021, doi: 10.3390/GASES1030011.

[2] D. Menniti, A. Burgio, and N. Scordino, “Population growth, sustainable development, energy resources and environmental protection: The nuclear option,” in *2007 IEEE Lausanne POWERTECH, Proceedings*, 2007, pp. 1812–1816, doi: 10.1109/PCT.2007.4538592.

[3] S. Kaza, L. Yao, P. Bhada-Tata, and F. Van Woerden, “WHAT A WASTE 2.0 A Global Snapshot of Solid Waste Management to 2050 OVERVIEW.”

[4] G. Charis *et al.*, “Waste to Energy Opportunities in Botswana: A Case Study Review,” Nov. 2019, doi: 10.1109/IRSEC48032.2019.9078153.

[5] S. Frimpong, “Global Energy Security: The Case for a Multifaceted Solution Strategy,” *J. Energy Eng.*, vol. 134, no. 4, pp. 109–110, Dec. 2008, doi: 10.1061/(asce)0733-9402(2008)134:4(109).

[6] O. S. Shittu, I. D. Williams, and P. J. Shaw, “Global E-waste management: Can WEEE make a difference? A review of e-waste trends, legislation, contemporary issues and future challenges,” *Waste Management*, vol. 120. Elsevier Ltd, pp. 549–563, Feb. 01, 2021, doi: 10.1016/j.wasman.2020.10.016.

[7] M. S. Haque, S. Uddin, S. M. Sayem, and K. M. Mohib, “Coronavirus disease 2019 (COVID-19) induced waste scenario: A short overview,” *J. Environ. Chem. Eng.*, vol. 9, no. 1, p. 104660, Feb. 2021, doi: 10.1016/j.jece.2020.104660.

[8] Dod, “Task Force on Energy Systems for Forward/Remote Operating Bases,” Washington DC, 2016.

[9] A. Meier, M. Shah, K. Engeling, and K. Quinn, “Demonstration of Plasma Assisted Waste Conversion to Gas,” *49th Int. Conf. Environ. Syst.*, no. July, pp. 1–13, 2019.

[10] L. Tang, H. Huang, H. Hao, and K. Zhao, “Development of plasma pyrolysis/gasification systems for energy efficient and environmentally sound waste disposal,” *Journal of Electrostatics*, vol. 71, no. 5. Elsevier, pp. 839–847, Oct. 01, 2013, doi: 10.1016/j.elstat.2013.06.007.

[11] G. Perkins, “Production of electricity and chemicals using gasification of municipal solid wastes,” in *Waste Biorefinery*, Elsevier, 2020, pp. 3–39.

[12] N. I. Blaisi, J. G. Roessler, B. E. Watts, J. Paris, C. C. Ferraro, and T. G. Townsend, “Construction material properties of high temperature arc gasification slag as a portland cement replacement,” 2018, doi: 10.1016/j.jclepro.2018.05.277.

[13] U. Arena, “Process and technological aspects of municipal solid waste gasification. A review,” *Waste Manag.*, vol. 32, no. 4, pp. 625–639, Apr. 2012, doi: 10.1016/j.wasman.2011.09.025.

[14] P. Breeze, “Advanced Waste-to-Energy Technologies,” in *Energy from Waste*, Elsevier, 2018, pp. 65–75.

[15] H. Sekiguchi and T. Orimo, “Gasification of polyethylene using steam plasma generated by microwave discharge,” *Thin Solid Films*, vol. 457, no. 1, pp. 44–47, 2004, doi: 10.1016/j.tsf.2003.12.035.

[16] H. S. Uhm, Y. H. Na, Y. C. Hong, D. H. Shin, and C. H. Cho, “Production of hydrogen-rich synthetic gas from low-grade coals by microwave steam-plasmas,” *Int. J. Hydrogen Energy*, vol. 39, no. 9, pp. 4351–4355, 2014, doi: 10.1016/j.ijhydene.2014.01.020.

[17] A. Sanlisoy and M. O. Carpinlioglu, “A review on plasma gasification for solid waste disposal,” *Int. J. Hydrogen Energy*, vol. 42, no. 2, pp. 1361–1365, 2017, doi: 10.1016/j.ijhydene.2016.06.008.

[18] G. S. Ho, H. M. Faizal, and F. N. Ani, “Microwave induced plasma for solid fuels and waste processing: A review on affecting factors and performance criteria,” *Waste Manag.*, vol. 69, pp. 423–430, 2017, doi: 10.1016/j.wasman.2017.08.015.

[19] E. Delikonstantis *et al.*, “Biomass gasification in microwave plasma: An experimental feasibility study with a side stream from a fermentation reactor,” *Chem. Eng. Process. - Process Intensif.*, vol. 141, p. 107538, Jul. 2019, doi: 10.1016/j.cep.2019.107538.

[20] T. N. Wu, “Environmental perspectives of microwave applications as remedial alternatives: Review,” *Practice Periodical of Hazardous, Toxic, and Radioactive Waste Management*, vol. 12, no. 2. American Society of Civil Engineers, pp. 102–115, Apr. 01, 2008, doi: 10.1061/(ASCE)1090-025X(2008)12:2(102).

[21] M. T. Munir, I. Mardon, S. Al-Zuhair, A. Shawabkeh, and N. U. Saqib, “Plasma gasification of municipal solid waste for waste-to-value processing,” *Renew. Sustain. Energy Rev.*, vol. 116, no. October, p. 109461, 2019, doi: 10.1016/j.rser.2019.109461.

[22] F. Saleem, J. Harris, K. Zhang, and A. Harvey, “Non-thermal plasma as a

promising route for the removal of tar from the product gas of biomass gasification – A critical review," *Chem. Eng. J.*, vol. 382, no. September 2019, p. 122761, 2020, doi: 10.1016/j.cej.2019.122761.

[23] F. Saleem *et al.*, "A comparison of the decomposition of biomass gasification tar compound in CO, CO2, H2 and N2 carrier gases using non-thermal plasma," *J. Energy Inst.*, vol. 97, pp. 161–168, Aug. 2021, doi: 10.1016/j.joei.2021.04.013.

[24] S. Dharmaraj *et al.*, "Pyrolysis: An effective technique for degradation of COVID-19 medical wastes," *Chemosphere*, vol. 275. Elsevier Ltd, p. 130092, Jul. 01, 2021, doi: 10.1016/j.chemosphere.2021.130092.

[25] C. Chicone, "Problems and Projects: Waveguides, Lord Kelvin's Model," in *An Invitation to Applied Mathematics*, Elsevier, 2017, pp. 775–791.

[26] Y. C. Hong *et al.*, "Syngas production from gasification of brown coal in a microwave torch plasma," *Energy*, vol. 47, no. 1, pp. 36–40, 2012, doi: 10.1016/j.energy.2012.05.008.

[27] C. R. Ellison, R. Hoff, C. Mărculescu, and D. Boldor, "Investigation of microwave-assisted pyrolysis of biomass with char in a rectangular waveguide applicator with built-in phase-shifting," *Appl. Energy*, vol. 259, p. 114217, Feb. 2020, doi: 10.1016/j.apenergy.2019.114217.

[28] H. Sun, J. Lee, and M. S. Bak, "Experiments and modeling of atmospheric pressure microwave plasma reforming of a methane-carbon dioxide mixture," *J. CO2 Util.*, vol. 46, p. 101464, Apr. 2021, doi: 10.1016/j.jcou.2021.101464.

[29] S. Vecten *et al.*, "Experimental study of steam and carbon dioxide microwave plasma for advanced thermal treatment application," *Energy*, vol. 207, p. 118086, Sep. 2020, doi: 10.1016/j.energy.2020.118086.

[30] S. Vecten, M. Wilkinson, N. Bimbo, R. Dawson, and B. M. J. Herbert, "Experimental investigation of the temperature distribution in a microwave-induced plasma reactor," *Fuel Process. Technol.*, vol. 212, p. 106631, Feb. 2021, doi: 10.1016/j.fuproc.2020.106631.

[31] S. J. Yoon and J. G. Lee, "Syngas Production from Coal through Microwave Plasma Gasification: Influence of Oxygen, Steam, and Coal Particle Size," 2011, doi: 10.1021/ef2013584.

[32] S. J. Yoon, Y. M. Yun, M. W. Seo, Y. K. Kim, H. W. Ra, and J. G. Lee, "Hydrogen and syngas production from glycerol through microwave plasma gasification," *Int. J. Hydrogen Energy*, vol. 38, no. 34, pp. 14559–14567, Nov.

2013, doi: 10.1016/j.ijhydene.2013.09.001.

[33] D. H. Shin *et al.*, “A pure steam microwave plasma torch: Gasification of powdered coal in the plasma,” *Surf. Coatings Technol.*, vol. 228, no. SUPPL.1, pp. S520–S523, Aug. 2013, doi: 10.1016/j.surfcoat.2012.04.071.

[34] L. Su, R. Kumar, B. Ogungbesan, and M. Sassi, “Experimental investigation of gas heating and dissociation in a microwave plasma torch at atmospheric pressure,” *Energy Convers. Manag.*, vol. 78, pp. 695–703, Feb. 2014, doi: 10.1016/j.enconman.2013.12.001.

[35] K. C. Lin, Y. C. Lin, and Y. H. Hsiao, “Microwave plasma studies of Spirulina algae pyrolysis with relevance to hydrogen production,” *Energy*, vol. 64, pp. 567–574, Jan. 2014, doi: 10.1016/j.energy.2013.09.055.

[36] C. H. Tsai and K. T. Chen, “Production of hydrogen and nano carbon powders from direct plasmalysis of methane,” *Int. J. Hydrogen Energy*, vol. 34, no. 2, pp. 833–838, Jan. 2009, doi: 10.1016/j.ijhydene.2008.10.061.

[37] Y. F. Wang, Y. S. You, C. H. Tsai, and L. C. Wang, “Production of hydrogen by plasma-reforming of methanol,” *Int. J. Hydrogen Energy*, vol. 35, no. 18, pp. 9637–9640, Sep. 2010, doi: 10.1016/j.ijhydene.2010.06.104.

[38] G. S. J. Sturm, A. N. Munoz, P. V. Aravind, and G. D. Stefanidis, “Microwave-Driven Plasma Gasification for Biomass Waste Treatment at Miniature Scale,” *IEEE Trans. Plasma Sci.*, vol. 44, no. 4, pp. 670–678, 2016, doi: 10.1109/TPS.2016.2533363.

[39] B. Hrycak, D. Czylkowski, R. Miotk, M. Dors, M. Jasinski, and J. Mizeraczyk, “Application of atmospheric pressure microwave plasma source for hydrogen production from ethanol,” in *International Journal of Hydrogen Energy*, Sep. 2014, vol. 39, no. 26, pp. 14184–14190, doi: 10.1016/j.ijhydene.2014.02.160.

[40] X. Su, H. Jin, L. Guo, S. Guo, and Z. Ge, “Experimental study on Zhundong coal gasification in supercritical water with a quartz reactor: Reaction kinetics and pathway,” 2015, doi: 10.1016/j.ijhydene.2015.02.110.

[41] A. Chanthakett, M. T. Arif, M. M. K. Khan, and A. M. T. Oo, “Performance assessment of gasification reactors for sustainable management of municipal solid waste,” *J. Environ. Manage.*, vol. 291, p. 112661, Aug. 2021, doi: 10.1016/j.jenvman.2021.112661.

[42] A. Okino *et al.*, “Development of a new multi-plasma gas inductively coupled plasma torch,” in *IEEE International Conference on Plasma Science*, 2004, p. 306,

doi: 10.1109/plasma.2004.1339986.

[43] G. Pintsuk and A. Hasegawa, “Tungsten as a Plasma-Facing Material,” in *Comprehensive Nuclear Materials*, Elsevier, 2020, pp. 19–53.

[44] W. Ebeling, “Coulomb interaction and ionization equilibrium in partially ionized plasmas,” *Physica*, vol. 43, no. 2, pp. 293–306, Jul. 1969, doi: 10.1016/0031-8914(69)90009-3.

[45] Y. Makonnen and D. Beauchemin, “The inductively coupled plasma as a source for optical emission spectrometry and mass spectrometry,” in *Sample Introduction Systems in ICPMS and ICPOES*, Elsevier, 2020, pp. 1–55.

[46] A. Pattiya, “Direct Thermochemical Liquefaction for Energy Applications Fast pyrolysis,” 2018, doi: 10.1016/B978-0-08-101029-7.00001-1.

[47] S. J. Yoon and J. G. Lee, “Hydrogen-rich syngas production through coal and charcoal gasification using microwave steam and air plasma torch,” *Int. J. Hydrogen Energy*, vol. 37, no. 22, pp. 17093–17100, 2012, doi: 10.1016/j.ijhydene.2012.08.054.

[48] B. Ibrahimoglu, A. Cucen, and M. Z. Yilmazoglu, “Numerical modeling of a downdraft plasma gasification reactor,” *Int. J. Hydrogen Energy*, vol. 42, no. 4, pp. 2583–2591, Jan. 2017, doi: 10.1016/j.ijhydene.2016.06.224.

[49] V. B. R. E. Silva and J. Cardoso, “Introduction and overview of using computational fluid dynamics tools,” in *Computational Fluid Dynamics Applied to Waste-to-Energy Processes*, Elsevier, 2020, pp. 3–28.

[50] H. Kobayashi, J. B. Howard, and A. F. Sarofim, “Coal devolatilization at high temperatures,” *Symp. Combust.*, vol. 16, no. 1, pp. 411–425, Jan. 1977, doi: 10.1016/S0082-0784(77)80341-X.

[51] P. C. Kuo, B. Illathukandy, W. Wu, and J. S. Chang, “Plasma gasification performances of various raw and torrefied biomass materials using different gasifying agents,” *Bioresour. Technol.*, vol. 314, no. June, 2020, doi: 10.1016/j.biortech.2020.123740.

[52] D. C. Park, S. J. Day, and P. F. Nelson, “Formation of N-containing gas-phase species from char gasification in steam,” *Fuel*, vol. 87, no. 6, pp. 807–814, May 2008, doi: 10.1016/j.fuel.2007.05.005.

[53] C. Gai, Y. Dong, and T. Zhang, “Distribution of sulfur species in gaseous and condensed phase during downdraft gasification of corn straw,” *Energy*, vol. 64, pp. 248–258, Jan. 2014, doi: 10.1016/j.energy.2013.11.052.

[54] P. C. Kuo, W. Wu, and W. H. Chen, “Gasification performances of raw and torrefied biomass in a downdraft fixed bed gasifier using thermodynamic analysis,” *Fuel*, vol. 117, no. PARTB, pp. 1231–1241, Jan. 2014, doi: 10.1016/j.fuel.2013.07.125.

[55] B. Ibrahimoglu and M. Z. Yilmazoglu, “Numerical modeling of a downdraft plasma coal gasifier with plasma reactions,” *Int. J. Hydrogen Energy*, vol. 45, no. 5, pp. 3532–3548, 2020, doi: 10.1016/j.ijhydene.2018.12.198.

[56] V. B. R. E. Silva and J. Cardoso, “How to approach a real CFD problem—A decision-making process for gasification,” in *Computational Fluid Dynamics Applied to Waste-to-Energy Processes*, Elsevier, 2020, pp. 29–83.

[57] S. Badzioch and P. G. W. Hawksley, “Kinetics of Thermal Decomposition of Pulverized Coal Particles,” *Ind. Eng. Chem. Process Des. Dev.*, vol. 9, no. 4, pp. 521–530, 1970, doi: 10.1021/i260036a005.

[58] P. C. Kuo, B. Illathukandy, W. Wu, and J. S. Chang, “Plasma gasification performances of various raw and torrefied biomass materials using different gasifying agents,” *Bioresour. Technol.*, vol. 314, p. 123740, Oct. 2020, doi: 10.1016/j.biortech.2020.123740.

[59] F. Fan, S. Wang, S. Yang, J. Hu, and H. Wang, “Numerical investigation of gas thermal property in the gasification process of a spouted bed gasifier,” *Appl. Therm. Eng.*, vol. 181, p. 115917, Nov. 2020, doi: 10.1016/j.applthermaleng.2020.115917.

[60] N. Couto, V. B. Silva, C. Bispo, and A. Rouboa, “From laboratorial to pilot fluidized bed reactors: Analysis of the scale-up phenomenon,” *Energy Convers. Manag.*, vol. 119, pp. 177–186, Jul. 2016, doi: 10.1016/j.enconman.2016.03.085.

[61] N. Couto *et al.*, “Numerical and experimental analysis of municipal solid wastes gasification process,” *Appl. Therm. Eng.*, vol. 78, pp. 185–195, Mar. 2015, doi: 10.1016/j.applthermaleng.2014.12.036.

[62] M. K. Thompson and J. M. Thompson, “Introduction to ANSYS and Finite Element Modeling,” in *ANSYS Mechanical APDL for Finite Element Analysis*, Elsevier, 2017, pp. 1–9.

[63] “About Ansys.” https://www.ansys.com/about-ansys (accessed Feb. 22, 2021).

[64] T. Liu and D. Zhao, “Numeric simulation and analysis of H 2-O 2 premixed combustion based on OpenFOAM,” in *Proceedings - 2012 IEEE Symposium on Robotics and Applications, ISRA 2012*, 2012, pp. 27–30, doi:

10.1109/ISRA.2012.6219111.

[65] “OpenFOAM.” https://www.openfoam.com/ (accessed May 18, 2021).

[66] “Ansys CFX | Industry-Leading CFD Software.” https://www.ansys.com/products/fluids/ansys-cfx (accessed May 18, 2021).

[67] B. Barbu, A. Iturregi, F. Berger, and E. Torres, “Numerical analysis of the electric arc simulation using ansys CFX,” in *IET Conference Publications*, 2012, vol. 2012, no. 605 CP, pp. 311–316, doi: 10.1049/cp.2012.0667.

[68] H. N. S. Yadav, M. Kumar, A. Kumar, and M. Das, “COMSOL simulation of microwave plasma polishing on different surfaces,” *Mater. Today Proc.*, Feb. 2021, doi: 10.1016/j.matpr.2021.01.266.

[69] “COMSOL Multiphysics® Software - Understand, Predict, and Optimize.” https://www.comsol.com/comsol-multiphysics (accessed May 18, 2021).

[70] S. Krusch, V. Scherer, R. Solimene, and O. Senneca, “Assessment of coal pyrolysis kinetics for Barracuda or Ansys Fluent,” in *Energy Procedia*, Feb. 2019, vol. 158, pp. 1999–2004, doi: 10.1016/j.egypro.2019.01.459.

[71] “Research and General Fluidization | CPFD Software.” https://cpfd-software.com/applications/general-fluidization/ (accessed May 18, 2021).

[72] P. H. Brunner and H. Rechberger, “Waste to energy – key element for sustainable waste management,” *Waste Manag.*, vol. 37, pp. 3–12, Mar. 2015, doi: 10.1016/J.WASMAN.2014.02.003.

[73] T. Malkow, “Novel and innovative pyrolysis and gasification technologies for energy efficient and environmentally sound MSW disposal,” *Waste Manag.*, vol. 24, no. 1, pp. 53–79, Jan. 2004, doi: 10.1016/S0956-053X(03)00038-2.

[74] B. Leckner, “Process aspects in combustion and gasification Waste-to-Energy (WtE) units,” *Waste Manag.*, vol. 37, pp. 13–25, Mar. 2015, doi: 10.1016/J.WASMAN.2014.04.019.

[75] L. Lombardi, E. Carnevale, and A. Corti, “A review of technologies and performances of thermal treatment systems for energy recovery from waste,” *Waste Manag.*, vol. 37, pp. 26–44, Mar. 2015, doi: 10.1016/J.WASMAN.2014.11.010.

[76] A. Veses *et al.*, “A pyrolysis process coupled to a catalytic cracking stage: A potential waste-to-energy solution for mattress foam waste,” *Waste Manag.*, vol. 120, pp. 415–423, Feb. 2021, doi: 10.1016/J.WASMAN.2020.09.052.

[77] S. Nanda and F. Berruti, “Municipal solid waste management and landfilling technologies: a review,” *Environ. Chem. Lett.*, vol. 19, no. 2, pp. 1433–1456, Apr. 2021, doi: 10.1007/S10311-020-01100-Y.

[78] N. B. Klinghoffer and M. J. Castaldi, “Gasification and pyrolysis of municipal solid waste (MSW),” *Waste to Energy Convers. Technol.*, pp. 146–176, 2013, doi: 10.1533/9780857096364.2.146.

[79] M. M. Hasan, M. G. Rasul, M. M. K. Khan, N. Ashwath, and M. I. Jahirul, “Energy recovery from municipal solid waste using pyrolysis technology: A review on current status and developments,” *Renew. Sustain. Energy Rev.*, vol. 145, p. 111073, Jul. 2021, doi: 10.1016/J.RSER.2021.111073.

[80] Y. Sun, Z. Qin, Y. Tang, T. Huang, S. Ding, and X. Ma, “Techno-environmental-economic evaluation on municipal solid waste (MSW) to power/fuel by gasification-based and incineration-based routes,” *J. Environ. Chem. Eng.*, vol. 9, no. 5, p. 106108, Oct. 2021, doi: 10.1016/J.JECE.2021.106108.

[81] D. S. Pandey, S. Das, I. Pan, J. J. Leahy, and W. Kwapinski, “Artificial neural network based modelling approach for municipal solid waste gasification in a fluidized bed reactor,” *Waste Manag.*, vol. 58, pp. 202–213, Dec. 2016, doi: 10.1016/J.WASMAN.2016.08.023.

[82] D. Baruah, D. C. Baruah, and M. K. Hazarika, “Artificial neural network based modeling of biomass gasification in fixed bed downdraft gasifiers,” *Biomass and Bioenergy*, vol. 98, pp. 264–271, 2017, doi: 10.1016/j.biombioe.2017.01.029.

[83] M. Puig-Arnavat, J. A. Hernández, J. C. Bruno, and A. Coronas, “Artificial neural network models for biomass gasification in fluidized bed gasifiers,” *Biomass and Bioenergy*, vol. 49, pp. 279–289, Feb. 2013, doi: 10.1016/J.BIOMBIOE.2012.12.012.

[84] H. T. Wen, J. H. Lu, and M. X. Phuc, “Applying artificial intelligence to predict the composition of syngas using rice husks: A comparison of artificial neural networks and gradient boosting regression,” *Energies*, vol. 14, no. 10, pp. 1–18, 2021, doi: 10.3390/en14102932.

[85] Y. Sun, L. Liu, Q. Wang, X. Yang, and X. Tu, “Pyrolysis products from industrial waste biomass based on a neural network model,” *J. Anal. Appl. Pyrolysis*, vol. 120, pp. 94–102, 2016, doi: 10.1016/j.jaap.2016.04.013.

[86] E. C. Vellekoop, “Artificial neural networks for determining the optimal process conditions of a gasification process,” no. 2733.

[87] S. L. Narnaware and N. L. Panwar, “Biomass gasification for climate change mitigation and policy framework in India: A review,” *Bioresour. Technol. Reports*, vol. 17, p. 100892, Feb. 2022, doi: 10.1016/J.BITEB.2021.100892.

[88] W. de Jong and J. Ruud van Ommen, *BIOMASS AS A SUSTAINABLE ENERGY SOURCE FOR THE FUTURE*. 2015.

[89] P. Basu, “Biomass Gasification, Pyrolysis and Torrefaction: Practical Design and Theory,” *Biomass Gasification, Pyrolysis Torrefaction Pract. Des. Theory*, pp. 1–530, 2013, doi: 10.1016/C2011-0-07564-6.

[90] L. Wang, C. L. Weller, D. D. Jones, and M. A. Hanna, “Contemporary issues in thermal gasification of biomass and its application to electricity and fuel production,” *Biomass and Bioenergy*, vol. 32, no. 7, pp. 573–581, Jul. 2008, doi: 10.1016/J.BIOMBIOE.2007.12.007.

[91] H. O. Kargbo, J. Zhang, and A. N. Phan, “Optimisation of two-stage biomass gasification for hydrogen production via artificial neural network,” *Appl. Energy*, vol. 302, p. 117567, Nov. 2021, doi: 10.1016/J.APENERGY.2021.117567.

[92] B. Liu and S. Ji, “Comparative study of fluidized-bed and fixed-bed reactor for syngas methanation over Ni-W/TiO2-SiO2 catalyst,” *J. Energy Chem.*, vol. 22, no. 5, pp. 740–746, Sep. 2013, doi: 10.1016/S2095-4956(13)60098-4.

[93] P. Basu, “Design of Biomass Gasifiers,” *Biomass Gasification, Pyrolysis and Torrefaction*, pp. 249–313, 2013, doi: 10.1016/B978-0-12-396488-5.00008-3.

[94] K. Suksankraisorn, S. Patumsawad, and B. Fungtammasan, “Co-firing of Thai lignite and municipal solid waste (MSW) in a fluidised bed: Effect of MSW moisture content,” *Appl. Therm. Eng.*, vol. 30, no. 17–18, pp. 2693–2697, Dec. 2010, doi: 10.1016/J.APPLTHERMALENG.2010.07.020.

[95] R. C. Boehm, Z. Yang, D. C. Bell, J. Feldhausen, and J. S. Heyne, “Lower heating value of jet fuel from hydrocarbon class concentration data and thermo-chemical reference data: An uncertainty quantification,” *Fuel*, p. 122542, Nov. 2021, doi: 10.1016/J.FUEL.2021.122542.

[96] C. SIMEONS, “GASIFICATION OF COAL,” *Coal its Role Tomorrow’s Technol.*, pp. 142–186, 1978, doi: 10.1016/B978-0-08-022712-2.50016-6.

[97] E. E. Robertson and R. D. WOOD, “PYROLYTIC GASIFICATION OF RENEWABLE BIOMASS RESOURCES,” *Sol. Energy Convers.*, pp. 1059–1089, 1979, doi: 10.1016/B978-0-08-024744-1.50043-7.

[98] N. R. Banapurmath, V. S. Yaliwal, S. Y. Adaganti, and S. S. Halewadimath,

"Power generation from renewable energy sources derived from biodiesel and low energy content producer gas for rural electrification," *Energy from Toxic Org. Waste Heat Power Gener.*, pp. 151–194, Jan. 2018, doi: 10.1016/B978-0-08-102528-4.00011-0.

[99] I. S. Hwang, J. Sohn, U. Do Lee, and J. Hwang, "CFD-DEM simulation of air-blown gasification of biomass in a bubbling fluidized bed gasifier: Effects of equivalence ratio and fluidization number," *Energy*, vol. 219, p. 119533, Mar. 2021, doi: 10.1016/J.ENERGY.2020.119533.

[100] M. Puig-Arnavat, J. A. Hernández, J. C. Bruno, and A. Coronas, "Artificial neural network models for biomass gasification in fluidized bed gasifiers," *Biomass and Bioenergy*, vol. 49, pp. 279–289, 2013, doi: 10.1016/j.biombioe.2012.12.012.

[101] J. Zhang, J. Liu, F. Evrendilek, X. Zhang, and M. Buyukada, "TG-FTIR and Py-GC/MS analyses of pyrolysis behaviors and products of cattle manure in CO2 and N2 atmospheres: Kinetic, thermodynamic, and machine-learning models," *Energy Convers. Manag.*, vol. 195, no. March, pp. 346–359, 2019, doi: 10.1016/j.enconman.2019.05.019.

[102] S. Wen, M. Buyukada, F. Evrendilek, and J. Liu, "Uncertainty and sensitivity analyses of co-combustion/pyrolysis of textile dyeing sludge and incense sticks: Regression and machine-learning models," *Renew. Energy*, vol. 151, pp. 463–474, 2020, doi: 10.1016/j.renene.2019.11.038.

[103] A. Pathy, S. Meher, and B. P, "Predicting algal biochar yield using eXtreme Gradient Boosting (XGB) algorithm of machine learning methods," *Algal Res.*, vol. 50, no. April, p. 102006, 2020, doi: 10.1016/j.algal.2020.102006.

[104] U. Özveren, F. Kartal, S. Sezer, and Z. S. Özdoğan, "Investigation of steam gasification in thermogravimetric analysis by means of evolved gas analysis and machine learning," *Energy*, vol. 239, 2022, doi: 10.1016/j.energy.2021.122232.

[105] M. W. Seo *et al.*, "Recent advances of thermochemical conversieon processes for biorefinery," *Bioresour. Technol.*, vol. 343, 2022, doi: 10.1016/j.biortech.2021.126109.

[106] A. Bahadar *et al.*, "Elucidating the effect of process parameters on the production of hydrogen-rich syngas by biomass and coal Co-gasification techniques: A multi-criteria modeling approach," *Chemosphere*, vol. 287, 2022, doi: 10.1016/j.chemosphere.2021.132052.

[107] J. Li, M. Suvarna, L. Pan, Y. Zhao, and X. Wang, "A hybrid data-driven and mechanistic modelling approach for hydrothermal gasification," *Appl. Energy*, vol.

304, 2021, doi: 10.1016/j.apenergy.2021.117674.

[108] J. Li, L. Pan, M. Suvarna, and X. Wang, “Machine learning aided supercritical water gasification for H<inf>2</inf>-rich syngas production with process optimization and catalyst screening,” *Chem. Eng. J.*, vol. 426, 2021, doi: 10.1016/j.cej.2021.131285.

[109] M. Binns and H. M. U. Ayub, “Model reduction applied to empirical models for biomass gasification in downdraft gasifiers,” *Sustain.*, vol. 13, no. 21, 2021, doi: 10.3390/su132112191.

[110] E. Chen, R. Deng, Z. Wang, and Z. Fang, “Spatial Feature Learning Based Gaussian Process Regression for Blast Furnace Raceway Temperature Prediction,” in *2021 International Conference on Electronic Information Engineering and Computer Science, EIECS 2021*, 2021, pp. 635–641, doi: 10.1109/EIECS53707.2021.9588118.

[111] S. Zhao, J. Li, C. Chen, B. Yan, J. Tao, and G. Chen, “Interpretable machine learning for predicting and evaluating hydrogen production via supercritical water gasification of biomass,” *J. Clean. Prod.*, vol. 316, 2021, doi: 10.1016/j.jclepro.2021.128244.

[112] P. V. Gopirajan, K. P. Gopinath, G. Sivaranjani, and J. Arun, “Optimization of hydrothermal gasification process through machine learning approach: Experimental conditions, product yield and pollution,” *J. Clean. Prod.*, vol. 306, 2021, doi: 10.1016/j.jclepro.2021.127302.

[113] S. Sezer and U. Özveren, “Investigation of syngas exergy value and hydrogen concentration in syngas from biomass gasification in a bubbling fluidized bed gasifier by using machine learning,” *Int. J. Hydrogen Energy*, vol. 46, no. 39, pp. 20377–20396, 2021, doi: 10.1016/j.ijhydene.2021.03.184.

[114] S. Liu, H. Ji, Z. Hou, J. Zuo, and L. Fan, “Data-Driven Online Modelling for a UGI Gasification Process using Modified Lazy Learning with a Relevance Vector Machine,” *Int. J. Appl. Math. Comput. Sci.*, vol. 31, no. 2, pp. 321–335, 2021, doi: 10.34768/amcs-2021-0022.

[115] F. Cheng, A. A. Small, and L. M. Colosi, “The levelized cost of negative CO<inf>2</inf> emissions from thermochemical conversion of biomass coupled with carbon capture and storage,” *Energy Convers. Manag.*, vol. 237, 2021, doi: 10.1016/j.enconman.2021.114115.

[116] B. V. Ayodele, S. I. Mustapa, R. Kanthasamy, M. Zwawi, and C. K. Cheng, “Modeling the prediction of hydrogen production by co-gasification of plastic and

rubber wastes using machine learning algorithms," *Int. J. Energy Res.*, vol. 45, no. 6, pp. 9580–9594, 2021, doi: 10.1002/er.6483.

[117] Z. Wang, S. Huang, G. Wen, Q. Liu, and P. Tang, "Thermal conductivity prediction and structure-property relationship of CaO-SiO<inf>2</inf>-Al<inf>2</inf>O<inf>3</inf> ternary system: A combination of molecular dynamics simulations and machine learning," *J. Mol. Liq.*, vol. 324, 2021, doi: 10.1016/j.molliq.2020.114697.

[118] Y. Wang, Z. Liao, S. Mathieu, F. Bin, and X. Tu, "Prediction and evaluation of plasma arc reforming of naphthalene using a hybrid machine learning model," *J. Hazard. Mater.*, vol. 404, 2021, doi: 10.1016/j.jhazmat.2020.123965.

[119] S. Ascher, I. Watson, and S. You, "Machine learning methods for modelling the gasification and pyrolysis of biomass and waste," *Renew. Sustain. Energy Rev.*, 2021, doi: 10.1016/j.rser.2021.111902.

[120] L. M. Joshi, R. K. Bharti, and R. Singh, "Internet of things and machine learning-based approaches in the urban solid waste management: Trends, challenges, and future directions," *Expert Syst.*, 2021, doi: 10.1111/exsy.12865.

[121] Y. Shin and D. Shin, *Deep Learning and AutoML for Dynamic Modeling of LNG Regasification Process Using Seawater*, vol. 50. 2021.

[122] *International Conference on Modeling, Simulation and Optimization, CoMSO 2020*, vol. 206. 2021.

[123] "AIAA Science and Technology Forum and Exposition, AIAA SciTech Forum 2021," 2021.

[124] M. Rzychoń, A. Zogała, and L. Róg, "An interpretable extreme gradient boosting model to predict ash fusion temperatures," *Minerals*, vol. 10, no. 6, 2020, doi: 10.3390/min10060487.

[125] A. N. Kozlov, N. V. Tomin, D. N. Sidorov, E. E. S. Lora, and V. G. Kurbatsky, "Optimal operation control of PV-biomass gasifier-diesel-hybrid systems using reinforcement learning techniques," *Energies*, vol. 13, no. 10, 2020, doi: 10.3390/en13102632.

[126] F. Elmaz and Ö. Yücel, "Data-driven identification and model predictive control of biomass gasification process for maximum energy production," *Energy*, vol. 195, 2020, doi: 10.1016/j.energy.2020.117037.

[127] F. Elmaz, Ö. Yücel, and A. Y. Mutlu, "Predictive modeling of biomass gasification with machine learning-based regression methods," *Energy*, vol. 191,

2020, doi: 10.1016/j.energy.2019.116541.

[128] Y. Xiao, H. Yin, K. Xia, Y. Zhang, and H. Qi, *Utilization of CNN-LSTM Model in Prediction of Multivariate Time Series for UCG*, vol. 12488 LNCS. 2020.

[129] "Sustainable Waste Management Workshop: Microplastics in the Environment 2020," 2020.

[130] X. Yang, Z. Ma, H. Shen, and H. Chen, "Fault diagnosis of airflow jamming fault in double circulating fluidized bed based on multi-scale feature energy and KELM | 基于多尺度特征能量-核极限学习机的双循环流化床气流堵塞故障智能诊断," *Huagong Xuebao/CIESC J.*, vol. 70, no. 7, pp. 2616–2625, 2019, doi: 10.11949/0438-1157.20181334.

[131] E. E. Ozbas, D. Aksu, A. Ongen, M. A. Aydin, and H. K. Ozcan, "Hydrogen production via biomass gasification, and modeling by supervised machine learning algorithms," *Int. J. Hydrogen Energy*, vol. 44, no. 32, pp. 17260–17268, 2019, doi: 10.1016/j.ijhydene.2019.02.108.

[132] Y. Xiao, J. Yin, Y. Hu, J. Wang, H. Yin, and H. Qi, "Monitoring and control in underground coal gasification: Current research status and future perspective," *Sustain.*, vol. 11, no. 1, 2019, doi: 10.3390/su11010217.

[133] J. Kačur, M. Durdán, M. Laciak, and P. Flegner, "A comparative study of data-driven modeling methods for soft-sensing in underground coal gasification," *Acta Polytech.*, vol. 59, no. 4, pp. 322–351, 2019, doi: 10.14311/AP.2019.59.0322.

[134] A. Y. Mutlu and O. Yucel, "An artificial intelligence based approach to predicting syngas composition for downdraft biomass gasification," *Energy*, vol. 165, pp. 895–901, 2018, doi: 10.1016/j.energy.2018.09.131.

[135] Y. Ögren, P. Tóth, A. Garami, A. Sepman, and H. Wiinikka, "Development of a vision-based soft sensor for estimating equivalence ratio and major species concentration in entrained flow biomass gasification reactors," *Appl. Energy*, vol. 226, pp. 450–460, 2018, doi: 10.1016/j.apenergy.2018.06.007.

[136] K. Wang, C. Shang, W. Ke, Y. Jiang, and D. Huang, "Automatic structure and parameters tuning method for deep neural network soft sensor in chemical industries," *Huagong Xuebao/CIESC J.*, vol. 69, no. 3, pp. 900–906, 2018, doi: 10.11949/j.issn.0438-1157.20171435.

[137] "Gaussian processes for hybridizing analytical & Data-driven decision-making," in *Education Division 2018 - Core Programming Area at the 2018 AIChE Annual Meeting*, 2018, pp. 140–142.

[138] “IET Conference Publications,” in *IET Conference Publications*, 2018, vol. 2018, no. CP749.

[139] J. Kačur, M. Laciak, M. Durdán, and P. Flegner, “Utilization of Machine Learning method in prediction of UCG data,” in *2017 18th International Carpathian Control Conference, ICCC 2017*, 2017, pp. 278–283, doi: 10.1109/CarpathianCC.2017.7970411.

[140] C. Igathinathane and U. Ulusoy, “Machine vision methods based particle size distribution of ball- and gyro-milled lignite and hard coal,” *Powder Technol.*, vol. 297, pp. 71–80, 2016, doi: 10.1016/j.powtec.2016.03.032.

[141] “59th ISA Power Industry Division Symposium 2016, POWID 2016,” 2016.

[142] S. Liu, Z. Hou, and C. Yin, “Data-driven modeling for fixed-bed intermittent gasification processes by enhanced lazy learning incorporated with relevance vector machine,” in *IEEE International Conference on Control and Automation, ICCA*, 2014, pp. 1019–1024, doi: 10.1109/ICCA.2014.6871060.

[143] W. Xu, R. Wang, X. Gu, and Y. Sun, *Assessment of Texaco syngas components using extreme learning machine based quantum neural network*, vol. 355. 2013.

[144] H. Ma, X. Yang, J. Mao, and H. Zheng, “The Energy Efficiency Prediction Method Based on Gradient Boosting Regression Tree,” *2nd IEEE Conf. Energy Internet Energy Syst. Integr. EI2 2018 - Proc.*, Dec. 2018, doi: 10.1109/EI2.2018.8581904.

[145] P. Xue, Y. Lei, and Y. Li, “Research and prediction of Shanghai-Shenzhen 20 Index Based on the Support Vector Machine Model and Gradient Boosting Regression Tree,” *Proc. - 2020 Int. Conf. Intell. Comput. Autom. Syst. ICICAS 2020*, pp. 58–62, Dec. 2020, doi: 10.1109/ICICAS51530.2020.00019.

[146] H. Li, H. Wang, G. Li, S. Li, and J. Guo, “Study on urban wastewater discharge forecasting and influence factors analysis based on stochastic gradient regression,” *3rd Int. Symp. Intell. Inf. Technol. Appl. IITA 2009*, vol. 2, pp. 483–486, 2009, doi: 10.1109/IITA.2009.143.

[147] A. V. Konstantinov and L. V. Utkin, “Interpretable machine learning with an ensemble of gradient boosting machines,” *Knowledge-Based Syst.*, vol. 222, p. 106993, Jun. 2021, doi: 10.1016/J.KNOSYS.2021.106993.

[148] J. Li, L. Pan, M. Suvarna, Y. W. Tong, and X. Wang, “Machine Learning Prediction of Syngas Composition of Hydrothermal Gasification from Wet Organic Wastes,” *Energy-proceedings*, pp. 1–4, 2020, [Online]. Available:

http://www.energy-proceedings.org/wp-content/uploads/enerarxiv/1607393109.pdf.

[149] T. Klein and W. R. L. Anderegg, “A vast increase in heat exposure in the 21st century is driven by global warming and urban population growth,” 2021, doi: 10.1016/j.scs.2021.103098.

[150] S. Khan, R. Anjum, S. T. Raza, N. Ahmed Bazai, and M. Ihtisham, “Technologies for municipal solid waste management: Current status, challenges, and future perspectives,” *Chemosphere*, vol. 288, p. 132403, Feb. 2022, doi: 10.1016/J.CHEMOSPHERE.2021.132403.

[151] S. E. Vergara and G. Tchobanoglous, “Municipal solid waste and the environment: A global perspective,” *Annu. Rev. Environ. Resour.*, vol. 37, pp. 277–309, Nov. 2012, doi: 10.1146/ANNUREV-ENVIRON-050511-122532.

[152] N. Johnstone and J. Labonne, “Generation of household solid waste in OECD countries: An empirical analysis using macroeconomic data,” *Land Econ.*, vol. 80, no. 4, pp. 529–538, 2004, doi: 10.2307/3655808.

[153] Y. Ye *et al.*, “Bio-membrane based integrated systems for nitrogen recovery in wastewater treatment: Current applications and future perspectives,” *Chemosphere*, vol. 265, p. 129076, Feb. 2021, doi: 10.1016/J.CHEMOSPHERE.2020.129076.

[154] A. V. Shah, V. K. Srivastava, S. S. Mohanty, and S. Varjani, “Municipal solid waste as a sustainable resource for energy production: State-of-the-art review,” *J. Environ. Chem. Eng.*, vol. 9, no. 4, p. 105717, Aug. 2021, doi: 10.1016/J.JECE.2021.105717.

[155] M. M. Mian, X. Zeng, A. al N. Bin Nasry, and S. M. Z. F. Al-Hamadani, “Municipal solid waste management in China: a comparative analysis,” *J. Mater. Cycles Waste Manag.*, vol. 19, no. 3, pp. 1127–1135, Jul. 2017, doi: 10.1007/S10163-016-0509-9.

[156] “Waste Management - Google Books.” https://books.google.com/books?hl=en&lr=&id=wgehDwAAQBAJ&oi=fnd&pg=PR7&ots=O8Uti_dYVB&sig=DswFHMaGfTC_FCJTOMMtzezWjWU#v=onepage&q&f=false (accessed Oct. 23, 2021).

[157] H. Cheng and Y. Hu, “Municipal solid waste (MSW) as a renewable source of energy: Current and future practices in China,” *Bioresour. Technol.*, vol. 101, no. 11, pp. 3816–3824, Jun. 2010, doi: 10.1016/J.BIORTECH.2010.01.040.

[158] N. R. Council, “Waste Incineration and Public Health,” *Waste Inciner. Public Heal.*, Oct. 1999, doi: 10.17226/5803.

[159] “Reviewing National Ambient Air Quality Standards (NAAQS): Scientific and Technical Information | US EPA.” https://www.epa.gov/naaqs (accessed Dec. 06, 2021).

[160] “Integrated Solid Waste Management: A Lifecycle Inventory: A Lifecycle Inventory - P.R. White, M. Franke, P. Hindle - Google Books.” https://books.google.com/books?hl=en&lr=&id=QzqdWOOymToC&oi=fnd&pg=PR19&ots=yRIe3AG_cM&sig=VywhICAzeWmdcYwRdghyjF6o17s#v=onepage&q&f=false (accessed Oct. 25, 2021).

[161] G. Tchobanoglous and F. Kreith, “Handbook of Solid Waste Management, Second Edition,” 2002, Accessed: Oct. 25, 2021. [Online]. Available: https://www.accessengineeringlibrary.com/content/book/9780071356237.

[162] R. Rathna, S. Varjani, and E. Nakkeeran, “Recent developments and prospects of dioxins and furans remediation,” *J. Environ. Manage.*, vol. 223, pp. 797–806, Oct. 2018, doi: 10.1016/J.JENVMAN.2018.06.095.

[163] S. Khan, H. Galstyan, N. A. Bazai, and M. Idrees, “Surface interaction of cadmium and zinc metal ions on Al2O3 nanoparticles in aqueous solution,” *https://doi.org/10.1080/03067319.2020.1796990*, 2020, doi: 10.1080/03067319.2020.1796990.

[164] Usda, “DoDI 4170.11 December 11, 2009, Inorporating Change 2, August 31, 2018,” 2009, Accessed: Nov. 23, 2021. [Online]. Available: https://apps.osd.mil/sites/DoDIIC/Pages/default.aspx.

[165] “GAO United States General Accounting Office Report to Congressional Requesters HAZARDOUS WASTE DOD Efforts to Reduce Wmte,” 1989.

[166] D. J. Chester, “AFIT Scholar Theses and Dissertations Student Graduate Works A Life Cycle Analysis of DOD Expeditionary Waste Management Practices Using Simapro,” Accessed: Oct. 25, 2021. [Online]. Available: https://scholar.afit.edu/etd/2328.

[167] “DoD’s Energy Efficiency and Renewable Energy Initiatives,” 2011, Accessed: Nov. 23, 2021. [Online]. Available: www.eesi.org.

[168] U. Department of Veterans Affairs - Airborne Hazards and B. Pit Exposures, “VA Airborne Hazards and Open Burn Pit Registry Quick Reference Sheet,” Accessed: Oct. 25, 2021. [Online]. Available:

http://www.publichealth.va.gov/airbornehazards.

[169] "Military Deployment Periodic Occupational and Environmental Monitoring Summary (POEMS): Camp Al Fallujah and vicinity, Iraq Calendar Years: (2004 to 2011)," 2004.

[170] R. Modi, H. Al Khalisy, and I. Amzuta, "BURN PITS EXPOSURE AND A CASE OF USUAL INTERSTITIAL PNEUMONIA," *Chest*, vol. 156, no. 4, p. A1259, Oct. 2019, doi: 10.1016/J.CHEST.2019.08.1134.

[171] N. Jani *et al.*, "Self-Reports of Constrictive Bronchiolitis Among Service Members Participating in the Veterans Administration and Department of Defense Airborne Hazards and Open Burn Pit Registry," *Chest*, vol. 152, no. 4, p. A822, Oct. 2017, doi: 10.1016/J.CHEST.2017.08.854.

[172] C. Chen *et al.*, "What medical waste management system may cope With COVID-19 pandemic: Lessons from Wuhan," *Resour. Conserv. Recycl.*, vol. 170, p. 105600, Jul. 2021, doi: 10.1016/J.RESCONREC.2021.105600.

[173] R. M. Sebastian and J. Louis, "Understanding waste management at airports: A study on current practices and challenges based on literature review," *Renew. Sustain. Energy Rev.*, vol. 147, p. 111229, Sep. 2021, doi: 10.1016/J.RSER.2021.111229.

[174] A. A. Erdogan and M. Zeki Yilmazoglu, "Plasma gasification of the medical waste," 2020, doi: 10.1016/j.ijhydene.2020.12.069.

[175] Y. C. Hong *et al.*, "Syngas production from gasification of brown coal in a microwave torch plasma," *Energy*, vol. 47, no. 1, pp. 36–40, Nov. 2012, doi: 10.1016/j.energy.2012.05.008.

[176] C. Ariza, C. Casado, R. Q. Wang, E. Adams, and J. Marugán, "Comparative Evaluation of OpenFOAM® and ANSYS® Fluent for the Modeling of Annular Reactors," *Chem. Eng. Technol.*, vol. 41, no. 7, pp. 1473–1483, Jul. 2018, doi: 10.1002/CEAT.201700455.

[177] H. Xia, P. G. Tucker, and W. N. Dawes, "Level sets for CFD in aerospace engineering," *Prog. Aerosp. Sci.*, vol. 46, no. 7, pp. 274–283, 2010, doi: 10.1016/J.PAEROSCI.2010.03.001.

[178] R. Q. Wang, A. W. K. Law, and E. E. Adams, "Large-eddy simulation (LES) of settling particle cloud dynamics," *Int. J. Multiph. Flow*, vol. 67, pp. 65–75, Dec. 2014, doi: 10.1016/J.IJMULTIPHASEFLOW.2014.08.004.

[179] S. Wang, H. Lu, F. Zhao, and G. Liu, "CFD studies of dual circulating fluidized

bed reactors for chemical looping combustion processes," *Chem. Eng. J.*, vol. 236, pp. 121–130, Jan. 2014, doi: 10.1016/J.CEJ.2013.09.033.

[180] "Reactor Design & Simulation | Ansys." https://www.ansys.com/solutions/solutions-by-industry/materials-and-chemical-processing/reactor-design (accessed Feb. 22, 2021).

[181] A. A. A. A. Alrashed, M. S. Gharibdousti, M. Goodarzi, L. R. de Oliveira, M. R. Safaei, and E. P. Bandarra Filho, "Effects on thermophysical properties of carbon based nanofluids: Experimental data, modelling using regression, ANFIS and ANN," *Int. J. Heat Mass Transf.*, vol. 125, pp. 920–932, Oct. 2018, doi: 10.1016/J.IJHEATMASSTRANSFER.2018.04.142.

[182] R. Vinuesa and S. L. Brunton, "The Potential of Machine Learning to Enhance Computational Fluid Dynamics."

[183] A. Ramos and A. Rouboa, "Life cycle thinking of plasma gasification as a waste-to-energy tool: Review on environmental, economic and social aspects," *Renew. Sustain. Energy Rev.*, vol. 153, p. 111762, Jan. 2022, doi: 10.1016/J.RSER.2021.111762.

[184] K. C. Lin, Y. C. Lin, and Y. H. Hsiao, "Microwave plasma studies of Spirulina algae pyrolysis with relevance to hydrogen production," *Energy*, vol. 64, pp. 567–574, 2014, doi: 10.1016/j.energy.2013.09.055.

[185] G. S. Ho, H. M. Faizal, and F. N. Ani, "Microwave induced plasma for solid fuels and waste processing: A review on affecting factors and performance criteria," *Waste Management*, vol. 69. Elsevier Ltd, pp. 423–430, Nov. 01, 2017, doi: 10.1016/j.wasman.2017.08.015.

[186] S. J. Yoon and J. G. Lee, "Syngas Production from Coal through Microwave Plasma Gasification: Influence of Oxygen, Steam, and Coal Particle Size," 2011, doi: 10.1021/ef2013584.

[187] G. S. J. Sturm, A. N. Munoz, P. V. Aravind, and G. D. Stefanidis, "Microwave-Driven Plasma Gasification for Biomass Waste Treatment at Miniature Scale," *IEEE Trans. Plasma Sci.*, vol. 44, no. 4, pp. 670–678, Apr. 2016, doi: 10.1109/TPS.2016.2533363.

[188] B. Hrycak, D. Czylkowski, R. Miotk, M. Dors, M. Jasinski, and J. Mizeraczyk, "Application of atmospheric pressure microwave plasma source for hydrogen production from ethanol," *Int. J. Hydrogen Energy*, vol. 39, no. 26, pp. 14184–14190, 2014, doi: 10.1016/j.ijhydene.2014.02.160.

[189] “ANSYS FLUENT 12.0 Theory Guide - 17.4 Energy Equation.” https://www.afs.enea.it/project/neptunius/docs/fluent/html/th/node353.htm (accessed Nov. 23, 2021).

[190] “Chapter 1. Basic Fluid Flow.”

[191] “ANSYS FLUENT 12.0 Theory Guide - 4.4.1 Standard - Model.” https://www.afs.enea.it/project/neptunius/docs/fluent/html/th/node58.htm (accessed Nov. 04, 2021).

[192] “sklearn.linear_model.LinearRegression — scikit-learn 1.0.1 documentation.” https://scikit-learn.org/stable/modules/generated/sklearn.linear_model.LinearRegression.html (accessed Nov. 06, 2021).

[193] “Biomass Gasification and Pyrolysis: Practical Design and Theory - Prabir Basu - Google Books.” https://books.google.com/books?hl=en&lr=&id=QSypbUSdkikC&oi=fnd&pg=PP1&ots=VhYs1aEqi7&sig=a_zyESQtIQG8vbKXVM8knPL1fNs#v=onepage&q&f=false (accessed Nov. 07, 2021).

[194] D. Baruah and D. C. Baruah, “Modeling of biomass gasification: A review,” *Renew. Sustain. Energy Rev.*, vol. 39, pp. 806–815, Nov. 2014, doi: 10.1016/J.RSER.2014.07.129.

[195] F. Kartal and U. Özveren, “A deep learning approach for prediction of syngas lower heating value from CFB gasifier in Aspen plus®,” *Energy*, vol. 209, p. 118457, Oct. 2020, doi: 10.1016/J.ENERGY.2020.118457.

[196] M. Ozonoh, B. O. Oboirien, A. Higginson, and M. O. Daramola, “Performance evaluation of gasification system efficiency using artificial neural network,” *Renew. Energy*, vol. 145, pp. 2253–2270, Jan. 2020, doi: 10.1016/J.RENENE.2019.07.136.

[197] M. Shahbaz *et al.*, “Artificial neural network approach for the steam gasification of palm oil waste using bottom ash and CaO,” *Renew. Energy*, vol. 132, pp. 243–254, Mar. 2019, doi: 10.1016/J.RENENE.2018.07.142.

[198] “ANSYS FLUENT 12.0 User’s Guide - 26.13.1 Monitoring Residuals.” https://www.afs.enea.it/project/neptunius/docs/fluent/html/ug/node812.htm (accessed Nov. 23, 2021).

[199] A. A. Arpia, T.-B. Nguyen, W.-H. Chen, C.-D. Dong, and Y. Sik Ok, “Microwave-assisted gasification of biomass for sustainable and energy-efficient

biohydrogen and biosyngas production: A state-of-the-art review," 2021, doi: 10.1016/j.chemosphere.2021.132014.

[200] J. Li, J. Tao, B. Yan, L. Jiao, G. Chen, and J. Hu, "Review of microwave-based treatments of biomass gasification tar," 2021, doi: 10.1016/j.rser.2021.111510.

REPORT DOCUMENTATION PAGE

Form Approved
OMB No. 074-0188

1. REPORT DATE *(DD-MM-YYYY)*	2. REPORT TYPE	3. DATES COVERED *(From – To)*
03-24-2022	Master's Thesis	September 2020 – March 2022

TITLE AND SUBTITLE
Application of Machine Learning Models with Numerical Simulations of an Experimental Microwave Induced Plasma Gasification Reactor

5a. CONTRACT NUMBER
5b. GRANT NUMBER
5c. PROGRAM ELEMENT NUMBER

6. AUTHOR(S)
Sedej, Owen D., 2Lt, USAF

5d. PROJECT NUMBER
5e. TASK NUMBER
5f. WORK UNIT NUMBER

7. PERFORMING ORGANIZATION NAMES(S) AND ADDRESS(S)
Air Force Institute of Technology
Graduate School of Engineering and Management (AFIT/ENY)
2950 Hobson Way, Building 640
WPAFB OH 45433-8865

8. PERFORMING ORGANIZATION REPORT NUMBER
AFIT-ENV-MS-22-M-261

9. SPONSORING/MONITORING AGENCY NAME(S) AND ADDRESS(ES)
AFCEC
Dr. Robert Diltz
2261 Hughes Ave, Ste. 155
JBSA Lackland, TX 78236
robert.diltz@us.af.mil

10. SPONSOR/MONITOR'S ACRONYM(S)
11. SPONSOR/MONITOR'S REPORT NUMBER(S)

12. DISTRIBUTION/AVAILABILITY STATEMENT
DISTRUBTION STATEMENT A. APPROVED FOR PUBLIC RELEASE; DISTRIBUTION UNLIMITED.

13. SUPPLEMENTARY NOTES

14. ABSTRACT
Climate change continues to rage as an international and multi-faceted issue that requires immediate attention. Waste-to-energy technologies are one type of emerging solution that will help to mitigate several factors that contribute to climate change. These technologies can utilize municipal solid waste streams as a form of renewable energy while simultaneously reducing greenhouse gas emissions. One type of waste-to-energy technology that is currently emerging as an efficient and viable option is microwave-induced plasma gasification. This thesis aims to contribute to the future development of this technology by providing an in-depth literature review of how this technology physically operates and can be numerically modeled. Additionally, this thesis reviews literature of machine learning models that have been applied to gasification to make accurate predictions regarding the system. Finally, this thesis provides a framework of how to numerically model an experimental plasma gasification reactor in order to inform a variety of machine learning models. The machine learning models were able to achieve a high degree of accuracy (MAE = 0.011) for predicting the proportion of the reactor that is greater than 2000K given the input variables of reactor geometry and plasma flame temperature.

15. SUBJECT TERMS
Microwave Plasma Gasification, Machine Learning, Artificial Neural Networks, Computational Fluid Dynamics Modeling, Gradient Boosted Machines

16. SECURITY CLASSIFICATION OF:			17. LIMITATION OF ABSTRACT	18. NUMBER OF PAGES	19a. NAME OF RESPONSIBLE PERSON
a. REPORT	b. ABSTRACT	c. THIS PAGE			Dr. Eric G. Mbonimpa, AFIT/ENVR
U	U	U	UU	144	19b. TELEPHONE NUMBER *(Include area code)* (937) 255-3636 (eric.mbonimpa@afit.edu)

Standard Form 298 (Rev. 8-98)
Prescribed by ANSI Std. Z39-18